12-2020

Mechanical and Frictional Behavior of Textured and non-Textured Surfaces

Raghuram R. Santhapuram
University of Arkansas, Fayetteville

Mechanical and Frictional Behavior of Textured and non-Textured Surfaces

A dissertation submitted in partial fulfillment
of the requirements for the degree of
Doctor of Philosophy in Engineering

by

Raghuram R. Santhapuram
Jawaharlal Nehru Technological University - India
Bachelor of Science in Metallurgy and Materials Engineering, 2011
Technische Universität Bergakademie Freiberg - Germany
Master of Science in Computational Materials Science, 2015

December 2020
University of Arkansas

This dissertation is approved for recommendation to the Graduate Council.

Arun K. Nair, Ph.D.
Dissertation Director

Min Zou, Ph.D.
Committee Member

Paul Millett, Ph.D.
Committee Member

David Huitnik, Ph.D.
Committee Member

Jingi Chen, Ph.D.
Committee Member

Abstract

Tribology is the study of surfaces where two objects are sliding against another. Significant energy is lost due to friction between the sliding surfaces. Therefore, developing or designing surfaces to minimize friction is critical for the durability and reliability of the mechanical components. Several researchers have identified that surface texturing at the nanoscale (nanotexture) would reduce the friction between the contacting surfaces. The nanotextured surfaces have several applications in microelectromechanical systems and nanoelectromechanical systems. This dissertation employs molecular dynamics simulations to investigate the frictional and mechanical response of nanotextured aluminum (Al) and Al/amorphous silicon (a-Si) composite surfaces.

This study determines the effective geometry (spherical or cylindrical) for texturing an Al surface that lowers the coefficient of friction of the nanotextured surface compared to a smooth surface. The results suggest that as the counter surface radius increases, the coefficient of friction decreases. For the lower counter surface radius, the coefficient of friction of the textured surface is higher than the smooth surface. But, after a specific increase in the radius of the counter surface, the coefficient of friction of the textured surface is lower than the smooth surface.

The nanotextured surface consisting of Al has lower mechanical strength, which results in permanent failure even at low contact forces. Thus, a nanotextured hemispherical Al core surface is coated by an a-Si to protect the nanotextured surface from plastic deformation, and they are named as core-shell nanostructures (CSNs). The CSNs has previously shown remarkable deformation recovery to compression loading beyond the elastic limit. This study finds an optimum coating thickness that would protect the core from plastic deformation. i.e., the ratio of core radius to shell thickness should be between 0.5 and 2.0 to have deformation resistant CSNs.

Additionally, this research investigates the core (single crystal and grain boundary) and substrate (crystalline and amorphous) material that affect the mechanical behavior of the CSNs subject to indentation. The results from this study conclude that CSNs with a single crystal core and crystalline substrate are more reliable for deformation-resistant behavior than those that contain grain boundary core and amorphous substrate.

From our previous studies, it is clear that not all textured surfaces will have a lower coefficient of friction. The coefficient of friction also depends on the indenter or counter surface radius. Therefore, we investigate the relationship between surface texture (r, L) and counter surface (R) variables. The results from this study suggest that the counter surface radius should be greater than the difference between twice the pitch length and radius of the asperity ($R > (2L - r)$) in order to have lower COF for the textured surface compared to a smooth surface. The relationship found between the textured surface and indenter surface variables is also confirmed for CSNs. Further, the relationship established in this study is also verified using experiments.

This work provides the groundwork in designing the textured surfaces as well as deformation-resistant core-shell nanostructures that has both lower COF and deformation-resistant behavior. Additionally, this research finds the mechanisms behind the deformation-resistant behavior of the CSNs.

Acknowledgments

The success of this dissertation required a lot of guidance and assistance from many people. First and foremost, I would like to express my deepest gratitude to my advisor Dr. Arun K. Nair, for providing me an opportunity to work on this research topic and for his endless support throughout my dissertation. Dr. Nair is a humble and patient person who always encouraged new ideas, and this work would not have been possible without his support. I would also like to thank Dr. Min Zou, Dr. Paul Millett, Dr. David Huitnik, and Dr. Jingi Chen for taking time out of their busy schedule to serve on my dissertation committee. I especially want to thank Dr. Min Zou for providing the platform and sharing her wisdom to perform experiments. I am also thankful to Colin Phelan, who performed the experiments to support the simulation results and co-authored one of my papers. Colin contributed to the experimental part of the text and figures. Special thanks to Dr. Douglas Spearot from the University of Florida for his invaluable suggestions for the core-shell nanostructure papers. I would like to extend my gratitude to the professors and the staff at the University of Arkansas, particularly the Mechanical Engineering Department, who provided me an advanced education.

I would not forget the support I received from my colleagues in the Multiscale Materials Modeling Laboratory: Scott Muller, Matthew Brownell, Mohan Yasodharababu, Marco Fielder, Yucong Gu. We had endless brainstorming sessions when I got stuck with research, and they helped me see the issue with a different viewpoint. Along with the group members mentioned, I also would like to thank Cameron Hopper, Casey Lindbloom, Abigail Eaton, and Garrett Story, who joined the group recently.

I am grateful to receive financial assistance provided by the Center for Advanced Surface Engineering, under the National Science Foundation (specific grant number can be found in the

acknowledgements sections of Chapters 2-5). Further, I owe profound gratitude for the Arkansas High-Performance Computing Center to perform the computational work, and without their support, my dissertation would not have been possible. I am thankful to David Chaffin and Pawel Wolinski, who were prompt in supporting with any issues related to the cluster.

Finally, I would like to thank my parents, siblings, family members, and friends for being the greatest source of inspiration throughout my career.

Table of contents

List of published papers

Chapter 2

Raghuram Reddy Santhapuram, Arun K Nair., Frictional properties of multi-asperity surfaces at the nanoscale, Comput. Mater. Sci., 136(2017)253-263.

Chapter 3

Raghuram Reddy Santhapuram, Douglas E. Spearot, Arun K Nair., Mechanical behavior of core-shell nanostructures, Journal of Materials Science., 55(2020) 4303-4310.

Chapter 4

Raghuram Reddy Santhapuram, Douglas E. Spearot, Arun K Nair., Role of grain boundaries in plastic deformation of core-shell nanostructures, Journal of Materials Science., 55(2020) 16990-16999.

Chapter 5

Raghuram Reddy Santhapuram, Colin Phelan, Min Zou, Arun K Nair., The effect of dimensional parameters of multi-asperity surfaces on friction at the nanoscale, (Under review).

Chapter 1

1. Introduction

1.1 Motivation

Concepts of friction and wear have been researched for over five hundred years. Leonardo da Vinci was the first researcher to investigate friction[1], followed by Guillaume Amontons[2, 3]. The law of friction[4] is usually identified with Guillaume Amontons, which states that friction force is proportional to the applied normal force. Amontons' law explicitly depicts the non-adhesive contact behavior at macro and microscopic levels, and it is confirmed by various studies[5, 6]. However, Amontons' law does not apply for the miniaturized micro, and nanoelectromechanical systems (MEMS/NEMS) as adhesion influence on friction cannot be neglected due to the large surface area to volume ratio[7]. Therefore, a fundamental understanding of friction at the nanoscale is of great significance for technological applications such as MEMS/NEMS.

Over the past few decades, considerable progress has been made in understanding friction at the nanoscale due to the development of advanced technologies at the nanoscale. Besides experiments, atomistic simulations have also become a powerful tool to analyze friction due to an increase in computing power. At the nanoscale, nano indenters[9, 10] and atomic force microscopes[8, 9] are used to calibrate friction. Further, the development of the miniaturized systems is possible by nanotexturing the surface. These nanotextures can be manufactured using several techniques such as lithography[11], thermal evaporation[11, 12], plasma-enhanced chemical vapor deposition[12, 13].

The nanotexture (asperity) geometry plays a significant role in tribological properties. Thus, extensive research is performed on various asperity shapes ranging from wedges[14, 15], cylinders[16, 17], pyramids[18], spheres[16, 17, 19, 20], and random uneven surfaces[21, 22]. Due to the complex tribological mechanisms of the textured surfaces, it is difficult to understand the relation between

the microstructure and tribological properties. For example, the tribological properties of the metallic asperity surfaces are determined by plastic deformation[23]. The evolution of plasticity is observed in several studies[24, 25] and were characterized using high-resolution microscopes. Thus, to understand the tribological mechanisms at the nanoscale, single asperity friction and wear studies were performed by various researchers[11, 26-28]. This led to multi-asperity contact research for various materials in both experiments and computational modeling.

Experiments[11, 21, 29] performed on multi-asperity surfaces predicts that multi-asperity surfaces have a lower coefficient of friction compared to smooth surfaces due to the reduction in the contact area between the contacting surfaces. Multi-asperity surfaces also lack structural integrity, i.e., with an increase in the normal load, the deformation of the asperities increases, which would wear the asperities easily during friction tests[11]. Therefore, to protect and increase the reliability of the asperity surfaces, researchers developed a deformation-resistant core-shell nanostructure[12, 13, 19], by coating the surface with another material. These core-shell nanostructures can be operated at higher loads without sacrificing the frictional characteristics of the textured surfaces. Moreover, these core-shell nanostructures have also significantly reduced the coefficient of friction compared to nanodot textured surfaces consisting of just the core.

Further, several studies are performed using atomistic[30-33] and multi-scale computational models[34-36] to gain more insight into the tribological behavior of asperity surfaces. These simulation techniques have high spatial resolution compared to traditional methods. While researchers tested the tribological properties of the textured surfaces, their frictional behavior and deformational characteristics are still elusive at the nanoscale. i.e., do the multi-asperity surfaces will always have a lower coefficient of friction? even though the contacting surfaces fit in between the asperities. If not, what is the geometrical relation between asperity surface and counter surface

variables that will lower the coefficient of friction of the textured surface compared to a smooth surface? What geometry is best for designing the asperity surface? What is the optimal coating thickness needed on the material surface that would make the core-shell nanostructures deformation-resistant? Should the material in core of the core-shell nanostructure be a single crystal or polycrystal that gives better deformation-resistant characteristic for the core-shell nanostructures? Exploring and addressing these questions will help us better understand the mechanical and tribological properties of the textured surfaces at the nanoscale. We perform molecular dynamics simulations on core-shell and multi-asperity surfaces to answer these questions.

1.2 Objectives

The objective of this research is to gain a fundamental understanding of the frictional behavior of textured surfaces at the nanoscale and the mechanical behavior of the deformation-resistant core-shell nanostructures. The textured surface is made of aluminum (Al), and a core-shell textured surface is made of Al (core) and amorphous silicon (a-Si, shell). The findings from this study will enable the selection and design of textured and core-shell textured surfaces that can be used in a variety of nanomechanical applications. The main objectives of this study are:

1. Determine the frictional properties of multi-asperity spherical and cylindrical surfaces at the nanoscale. (Chapter 2)
2. Determine the deformation mechanisms of the core-shell nanostructures. (Chapter 3, 4)
3. Determine an optimal relation between the core radius and shell thickness of the core-shell nanostructures that would lead to a deformation-resistant behavior. (Chapter 3)

4. Determine the difference in deformation behavior of different core (single crystal and grain boundary core) and substrate materials (crystalline and amorphous) of core-shell nanostructures. (Chapter 4)
5. Determine a relationship between spherical textured surface and indenter surface variables that would reduce the coefficient of friction of the textured surface relative to a smooth surface. (Chapter 5)
6. Find the microscopic deformation mechanisms of the multi-asperity textured surfaces (Chapter 2 and 5) and core-shell nanostructures. (Chapters 3 and 4)

1.3 Novelty of this research

There are several new contributions from this research. First, we used molecular dynamics simulations to perform frictional studies on 3D multi-asperity surfaces (Chapter 2). Second, a force-based method is developed and used for nanoindentation studies as outlined in Chapters 3 and 4. Third, we optimized the core radius and shell thickness of core-shell nanostructures to achieve deformation-resistant behavior (Chapter 3). Fourth, we investigated the effect of core and substrate materials on core-shell nanostructures and performed a detailed analysis of core-shell nanostructure deformation behavior (Chapter 4). Finally, we established a geometrical relation between dimensional parameters of multi-asperity and counter surfaces to reduce friction between multi-asperity surfaces (Chapter 5).

1.4 Layout of dissertation

The dissertation is divided into six chapters and one appendix. Chapter 2 is a journal paper investigating the frictional properties of a multi-asperity surface with spherical and cylindrical asperities, as mentioned in objective 1. This paper would help to pick the suitable surface consisting of either spherical or cylindrical textures. Chapter 3 is a journal paper that determines a

relationship between the core radius to shell thickness of the core-shell nanostructures that captures the deformation-resistant behavior of the core-shell nanostructures (objectives 2 and 3). Chapter 4 is a journal paper that describes the role of single crystal and grain boundary core deformation mechanisms of core-shell nanostructures, as mentioned in objective 4. Chapter 5 describes a relation between textured surface and counter surface variables that would reduce the friction compared to a smooth surface (objective 5). Chapter 6 is an overall conclusion of the dissertation, where key results of the dissertation are summarized. Appendix A contains the microstructural evolution of the core-shell nanostructures during nanoindentation and corresponds to the results in Chapter 3.

References

1. I.M. Hutchings: Leonardo da Vinci′ s studies of friction *Wear.* **360**, 51 (2016).

2. J. Gao, W. Luedtke, D. Gourdon, M. Ruths, J. Israelachvili and U. Landman: Frictional forces and Amontons' law: from the molecular to the macroscopic scale, (ACS Publications, City, 2004).

3. A. Berman, C. Drummond and J. Israelachvili: Amontons' law at the molecular level *Tribology letters.* **4**(2), 95 (1998).

4. K. Komvopoulos and W. Yan: Molecular dynamics simulation of single and repeated indentation *Journal of applied physics.* **82**(10), 4823 (1997).

5. E. Rabinowicz: Friction and wear of materials (Wiley New York, City, 1965).

6. B. Persson: Sliding friction of lubricated surfaces, in Physics of Sliding Friction, (Springer, City, 1996), pp. 69.

7. A. Corwin and M. De Boer: Effect of adhesion on dynamic and static friction in surface micromachining *Applied Physics Letters.* **84**(13), 2451 (2004).

8. T. Filleter, J.L. McChesney, A. Bostwick, E. Rotenberg, K.V. Emtsev, T. Seyller, K. Horn and R. Bennewitz: Friction and dissipation in epitaxial graphene films *Physical review letters.* **102**(8), 086102 (2009).

9. C. Lee, Q. Li, W. Kalb, X.-Z. Liu, H. Berger, R.W. Carpick and J. Hone: Frictional characteristics of atomically thin sheets *science.* **328**(5974), 76 (2010).

10. R.A. Fleming and M. Zou: Nanostructure-textured surfaces with low friction and high deformation resistance *Tribology Transactions.* **61**(1), 80 (2018).

11. J.G. Steck, R.A. Fleming, J.A. Goss and M. Zou: Deformation and fatigue resistance of Al/a-Si core-shell nanostructures subjected to cyclic nanoindentation *Applied Surface Science.* **433**, 617 (2018).

12. R.A. Fleming and M. Zou: The effects of confined core volume on the mechanical behavior of Al/a-Si core-shell nanostructures *Acta Materialia.* **128**, 149 (2017).

13. J. Challen, L. McLean and P. Oxley: Plastic deformation of a metal surface in sliding contact with a hard wedge: its relation to friction and wear *Proceedings of the Royal Society of London. A. Mathematical and Physical Sciences.* **394**(1806), 161 (1984).

14. Q. Li and and M.R. Lovell: Predicting critical friction in a two-roll cross wedge rolling process *J. Trib.* **125**(1), 200 (2003).

15. D.M. Mulvihill, M.E. Kartal, D. Nowell and D.A. Hills: An elastic–plastic asperity interaction model for sliding friction *Tribology international.* **44**(12), 1679 (2011).

16. R.R. Santhapuram and A.K. Nair: Frictional properties of multi-asperity surfaces at the nanoscale *Computational Materials Science.* **136**, 253 (2017).

17. Y. Gerbig, S.-U. Ahmed and D. Chetwynd: Friction and wear behaviour of pyramidal nanoscaled surface features *Wear.* **265**(3-4), 497 (2008).

18. W. Tidwell, D. Scott, H. Wang, R. Fleming and M. Zou: Nanoindentation study of deformation-resistant Al/a-Si core–shell nanostructures *Acta Materialia.* **59**(15), 6110 (2011).

19. B.D. Morton, H. Wang, R.A. Fleming and M. Zou: Nanoscale surface engineering with deformation-resistant core–shell nanostructures *Tribology Letters.* **42**(1), 51 (2011).

20. M. Zou, L. Cai, H. Wang, D. Yang and T. Wyrobek: Adhesion and friction studies of a selectively micro/nano-textured surface produced by UV assisted crystallization of amorphous silicon *Tribology Letters.* **20**(1), 43 (2005).

21. M. Zou, L. Cai and H. Wang: Adhesion and friction studies of a nano-textured surface produced by spin coating of colloidal silica nanoparticle solution *Tribology Letters.* **21**(1), 25 (2006).

22. B. Bhushan: Nanotribology and nanomechanics: an introduction (Tribol. Lubric. Technol, City, 2017).

23. C. Greiner, J. Gagel and P. Gumbsch: Solids Under Extreme Shear: Friction-Mediated Subsurface Structural Transformations *Advanced Materials.* **31**(26), 1806705 (2019).

24. X. Chen, R. Schneider, P. Gumbsch and C. Greiner: Microstructure evolution and deformation mechanisms during high rate and cryogenic sliding of copper *Acta Materialia.* **161**, 138 (2018).

25. M. Mishra, P. Egberts, R. Bennewitz and I. Szlufarska: Friction model for single-asperity elastic-plastic contacts *Physical Review B.* **86**(4), 045452 (2012).

26. B. Gotsmann and M.A. Lantz: Atomistic wear in a single asperity sliding contact *Physical review letters.* **101**(12), 125501 (2008).

27. B. Bhushan: Contact mechanics of rough surfaces in tribology: single asperity contact, (1996).

28. H. Wang, R.P. Nair, M. Zou, P.R. Larson, A.L. Pollack, K. Hobbs, M.B. Johnson and O. Awitor: Friction study of a Ni nanodot-patterned surface *Tribology Letters.* **28**(2), 183 (2007).

29. W. Cheong and L. Zhang: Monocrystalline silicon subjected to multi-asperity sliding: nano-wear mechanisms, subsurface damage and effect of asperity interaction *International Journal of Materials and Product Technology.* **18**(4-6), 398 (2003).

30. T. Liu, G. Liu, P. Wriggers and S. Zhu: Study on contact characteristic of nanoscale asperities by using molecular dynamics simulations *Journal of Tribology.* **131**(2), 022001 (2009).

31. T.D. Jacobs, K.E. Ryan, P.L. Keating, D.S. Grierson, J.A. Lefever, K.T. Turner, J.A. Harrison and R.W. Carpick: The effect of atomic-scale roughness on the adhesion of nanoscale asperities: A combined simulation and experimental investigation *Tribology Letters.* **50**(1), 81 (2013).

32. L. Si and X. Wang: Nano-adhesion influenced by atomic-scale asperities: A molecular dynamics simulation study *Applied Surface Science.* **317**, 710 (2014).

33. R.T. Tong, G. Liu and T.X. Liu: Multiscale Analysis on Two Dimensional Nanoscale Sliding Contacts of Textured Surfaces *Journal of Tribology-Transactions of the Asme.* **133**(4), 041401 (2011).

34. R. Tong, G. Liu and L. Liu: Multiscale analysis on two-dimensional nanoscale adhesive contacts *Chinese Journal of Mechanical Engineering.* **25**(3), 446 (2012).

35. G. Anciaux and J.-F. Molinari: Sliding of rough surfaces and energy dissipation with a 3D multiscale approach *International Journal for Numerical Methods in Engineering.* **83**(8-9), 1255 (2010).

Chapter 2

2. Paper 1: Frictional properties of multi-asperity surfaces at the nanoscale

Raghuram Reddy Santhapuram, Arun K Nair

Abstract

Asperities are considered as unevenness of surfaces, or surface roughness. Surfaces that are finely polished are still considered uneven at the nanoscale. This unevenness of surface reduces the actual contact area when two surfaces come into contact. Understanding surface asperities are very important because the friction and wear properties of two materials depend on the nanoscale contact between the material surfaces. Many experimental studies have concluded that surface texture can help improve contact characteristics and reduce the frictional forces between surfaces. We use molecular dynamics simulations to study the frictional and mechanical response of an aluminum surface with cylindrical and spherical asperities that resemble true surfaces. Nanoindentation and scratch tests are carried out using different indenter radii on spherical and cylindrical asperities, and the results are compared to surfaces without asperities. We observe that the coefficient of friction (COF) is lower for spherical asperity surfaces, if the indenter radius is less than or equal to 4 nm, and the COF is lower for cylindrical asperity surfaces, if the indenter radius is greater than or equal to 5 nm. Finally, the COF decreases with increasing indenter radius for the surface geometries studied here. The atomic mechanisms corresponding to the observed frictional response of the surfaces are explained by dislocation nucleation and propagation in the system. These studies could perhaps be used to guide experiments to design multi-asperity surfaces for tribological applications.

Keywords: Multi-asperity surfaces, Coefficient of friction, Nanoindentation, Molecular Dynamics.

2.1 Introduction

The mechanics behind surface deformations have been of interest for researchers over the past few decades. Surface properties such as adhesion, friction, and wear are all important aspects for understanding and addressing the surface behavior of materials. Multi-asperity surfaces have gained tremendous interest in engineering due to tribological properties associated with them. With the availability of nanolithography [1], development of surfaces with nanoscale asperities of different shapes, and size are possible for various engineering applications. For example, researchers have recently shown that multi-asperity surfaces have application in cancer research[2], where they have shown that the malenoma cells migrate on a surface with cylindrical asperities based on the distance between asperities. Similarly, neuro cell[3, 4] growth depends on the geometry (cylindrical or spherical shape) of the surface with which the cell come into contact. It should be noted that depending on the application, the asperity size varies from micro to nano meter length scales. The deformation of the asperities plays a critical role towards surface properties due to contact with either probes (such as AFM) or other surfaces. Hence, understanding the properties of surfaces with different asperities has interdisciplinary application. Many continuum-based models have been proposed to understand the phenomenon of contacts between two surfaces. Hertz (1882) [5] describes the deformation of two elastic bodies; DMT theory [6] describes adhesive contact between spheres without elastic deformation. Unlike DMT theory, Johnson, Kendall et al. (1971) [7] (JKR) theory considers elastic deformation. Maugis (1992) [8] proposed a model which gives transition between DMT-JKR. All these continuum-based models have limitations when they are applied to micro or nano length scales [9].

Recent advances in the development of micro and nanoelectromechanical systems (MEMS/NEMS) demand better understanding of the contact mechanics in micro and nanoscale

surfaces [10]. Surface measuring technologies such as atomic force microscopy, frictional force microscopy (FFM) and lateral force microscopy (LFM) [11] are used to study the frictional and wear properties at the nanoscale. Developments in computational materials modeling have paved the path to use methods such as molecular dynamics (MD) which allow us to predict atomic level properties. This method has been widely used in exploring the surface properties of various materials [12-20]. Moreover, the results obtained by MD can guide the experimental research by providing the details of asperity shape, asperity size, and distance between asperities for specific application[20].

Cheong and Zhang (2003) [21] were the first to study the effect of relative position and orientation of asperities on the nanoscale wear mechanisms of silicon (Si) surfaces using MD simulations. They found that forces experienced by the asperities are independent of their relative positions and that there were no dislocations when the indentation depth is small. Cha et al. (2004) [22] investigated single asperity surface and its deformation when two surfaces come in contact. According to their study, JKR theory is not applicable to the loading condition of the asperity, but is applicable to unloading, and the deformation of the asperity is considered to be nearly elastic. Liu et al. (2009) [23] performed MD simulations to study contact between a rigid cylindrical probe and an elastic Cu substrate with and without adhesion by varying the radius, size, shape and number of asperities on the cylindrical probe. This study showed that the adhesive effect is stronger when surfaces have smaller and more numerous asperities in contact with the substrate. Similarly, Jacobs et al. (2013) [20] studied atomic scale roughness on adhesion between carbon based materials and nanoscale asperities of either diamond like carbon (DLC) or ultra-nanocrystalline diamond using MD and experiments; they found that adhesion decreased more than an order of magnitude as roughness increased. Si and Wang (2014) [18] conducted MD studies on surface roughness and

on adhesion between a spherical tip with single asperity and on smooth surfaces. The study was carried out by varying height, radii, and nanoindentation velocity, with both the spherical tips and surfaces made of Si. Their results led to the conclusion that the adhesion force decreases when the asperity size is at the nanoscale. However, the adhesion forces obtained are larger than the Rumpf [24] and Rabinovich [25] models, which they explain is due to not considering the chemical bonds.

Multiscale approaches have been performed by various researchers to address the nanoscale contact information using molecular dynamics and the finite element method [26-29]. Using the multiscale approach Tong et al. (2011) [26] studied 2D nano scale sliding contact between a rigid cylindrical tip and an elastic copper substrate with a textured surface. In their research, the adhesive effects are considered using different asperity shapes, height, and spacing between asperities; this allowed them to find the optimal asperity height and spacing between asperities on the copper substrate; however, the effect of the indenter radius or dislocation mechanisms were not investigated. They concluded that with the proper asperity height and spacing, surface texture can reduce frictional forces effectively. Tong et al. (2012) [27] using multiscale approach, studied the contact between a rigid cylindrical tip and a smooth surface. They conclude that the compressive force of textured surfaces increases with either increasing asperity height, or decreasing the asperity distance. This indicates that an appropriate spacing between the asperities could help in getting the required contact force. Similarly, Zhu et al (2011)[28] and Anciaux et al (2010)[29] has performed multiscale simulations, where Zhu et al. (2011)[28] revealed that indenter velocity and radius significantly affects the nanoindentation process; and Anciaux et al (2010)[29] implemented a bridging domain method coupled with FEM and MD which developed promising strategy for analysis of sliding contacts.

The current study focuses on multi-asperity surfaces of spherical or cylindrical shape which will reduce the surface friction and provide a better understanding of microscopic plastic deformation and its relationship to frictional properties. We perform nanoindentation and scratch tests on an aluminum (Al) surface with and without asperities using molecular dynamics simulations. We investigate how the coefficient of friction (COF) changes with the asperity geometry (sphere and cylinder), and the indenter radius. In this study, we propose model surfaces that can be used to identify the suitable asperity shape (cylinder or spherical asperities) that reduces the COF. This study also reveals microscopic deformation mechanisms, such as dislocation nucleation and propagation, for both spherical and cylindrical asperities during nanoindentation and scratch tests.

2.2 Methodology

We use molecular dynamics simulations to predict the COF on surfaces without asperities (Fig 1.a), as well as those with equally spaced spherical (Fig 1.b) and cylindrical asperities (Fig 1.c). All samples used in this study are single crystal Al with dimensions of 40, 20 and 25 nm along x [1 1 $\bar{2}$], y [1 1 1] and z [1 $\bar{1}$ 0] directions respectively. The spherical and cylindrical multi-asperities are created on top of the x-z plane, as shown in Fig. 1(b, c) where spacing between the asperities is 2 nm. The spherical asperity has a radius of 2 nm, and the cylindrical asperity has a radius and height of 2 nm and 4 nm respectively. An initial spacing of 2 nm between the asperities is chosen to avoid interaction between the asperities during nanoindentation and scratch process. For example, as observed by Tong et al (2011)[26] the deformed neighboring asperities could come in contact to form another asperity of higher radius. We also study different asperity distances for both cylindrical and spherical cases. We use spherical indenters with radii of 3, 4, 5 and 6 nm for nanoindentation and scratch tests. The indenter radii are considered such that it is greater than the

asperity size, and the indenter is in contact with more than one asperity at a given time during nanoindentation. We chose a thickness of 20 nm for the substrate to avoid the boundary effects. We also study two more asperity spacing at 1 and 3 nm with the indenter of radius 6nm, to see the effect of COF on different spacing between the asperities. During the nanoindentation and scratch process, the bottom 8 atom layers are fixed, and all other atoms are mobile. The periodic boundary conditions are employed along *x* and *z* directions and shrink-wrapped boundary conditions are employed in the *y* direction. Atomic interactions between Al atoms are governed by the embedded atom method [30].

The samples are first minimized and then equilibrated at 300 K by maintaining zero pressure along the *x* and *z* directions using NPT (isothermal and isobaric) ensemble for a duration of 350 ps. The indenter is lowered to the surface along the *y* direction and the samples are indented to a depth of 1.8 nm, and then scratched along the *x* direction over 10 nm. The velocity of the indenter is maintained at 5 m/s during nanoindentation and scratch tests. We use the LAMMPS [31] software package to perform MD simulations. For all simulations, we use a hard-spherical indenter (with force constant, K=10 ev/$A^{\circ 3}$) as implemented in LAMMPS [26]. The indenter implemented in LAMMPS describes the interaction between the indenter and surface atoms using a repulsive L-J potential. Common neighbor analysis and dislocation analysis (DXA) is performed using OVITO [32], which allow us to visualize defects, dislocations or stacking faults during the simulations.

We start the indentation such that the indenter is in contact with at least two asperities, which reflect experimental conditions where two surfaces of different asperities are in contact with each other. For indenter radii of 3, 4, 5 and 6 nm the center of indenter is in between the two neighboring asperities. To study the effect of location of indenter on COF, we study an additional

case, where the center of indenter of 6 nm radius is in between four neighboring asperities (see section 3, Fig 3). The location of the indenter center is specifically selected, because if the center of the indenter radius for 3, 4, and 5 nm is in between four neighboring asperities, the indenter will be in between the asperities instead of touching the top surface of the asperities, so the center for the indenter radius is selected in between two neighboring asperities. This is not the same case for the indenter with a radius of 6 nm, so the center for this indenter is chosen in two locations, one is in between two neighboring asperities and other is in between four neighboring asperities.

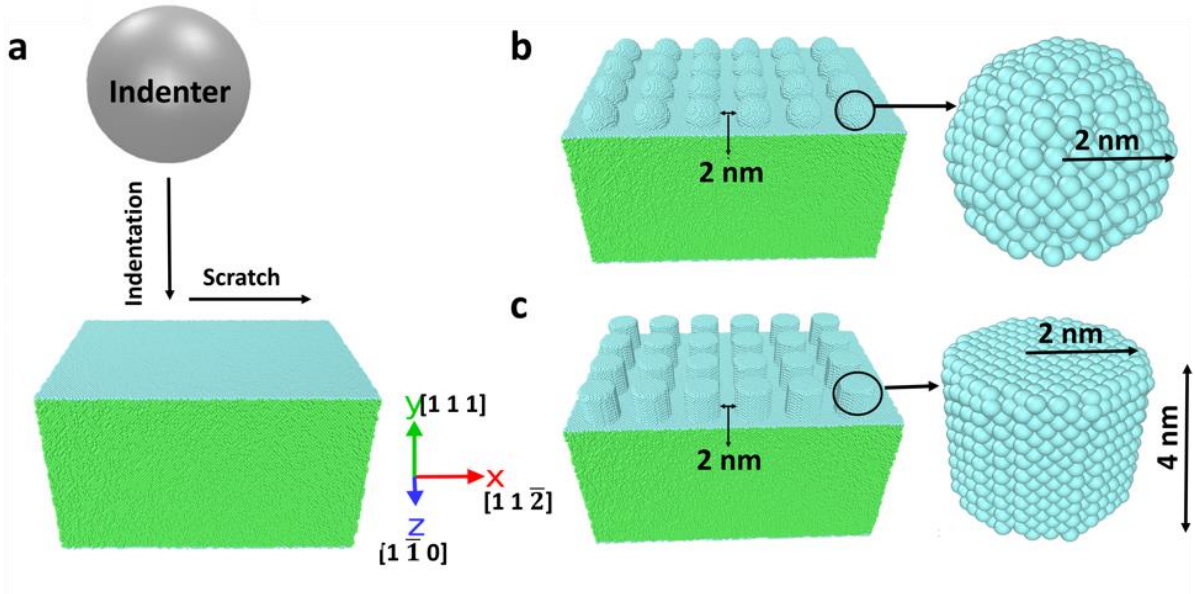

Fig 1. Nanoindentation and scratch process for (a) surface without asperity. (b) surface with spherical asperity (radius 2nm). (c) surface with cylindrical asperity (radius 2nm, height 4nm), The green color atoms in the model represents bulk FCC atoms of Al and the light blue color atoms represents surface atoms. Each sample has dimensions of 40×20×25 nm in the *x, y* and *z* directions respectively.

2.3 Results and discussion

The process to find the coefficient of friction is divided in two stages: (i) nanoindentation of the substrate until the indenter has reached the desired depth into the substrate, and (ii) scratching the surface by moving the indenter on the surface. Nanoindentation is performed in this study using indenters of radii 3, 4, 5 and 6 nm, while maintaining an indenter velocity of 5m/s.

Based on previous studies [12, 19, 33] and computational cost associated with MD simulations, we chose 5m/s as the indenter velocity for nanoindentation and scratch.

We indent the samples to a depth of 1.8 nm, to study the elastic and initial plastic deformation of the surfaces. Fig. 2 shows the nanoindentation force versus indentation depth for three samples and for four different indenter radii. The nanoindentation force is calculated as the total normal force on the indenter from the substrate atoms. Three regions are present in Fig. 2. In region 1 the indenter is above the substrate surface, which causes the forces to be zero. In region 2 the indenter starts to touch the surface and is in the elastic regime. In the elastic region, the nanoindentation force increases linearly until the critical indentation depth is reached, at which point the samples are no longer elastically deformed. The force and indentation depth corresponding to the first dislocation nucleation is defined as the critical nanoindentation force and critical indentation depth respectively. The critical indentation depths and critical nanoindentation forces found in this study are listed in Table 1. Region 3 starts after the critical indentation depth is reached. Within region 3 the nanoindentation force drops, which indicates the beginning of plastic deformation accompanied by dislocation nucleation. This deformation behavior in region 3 determines the work hardening stage of the material[34].

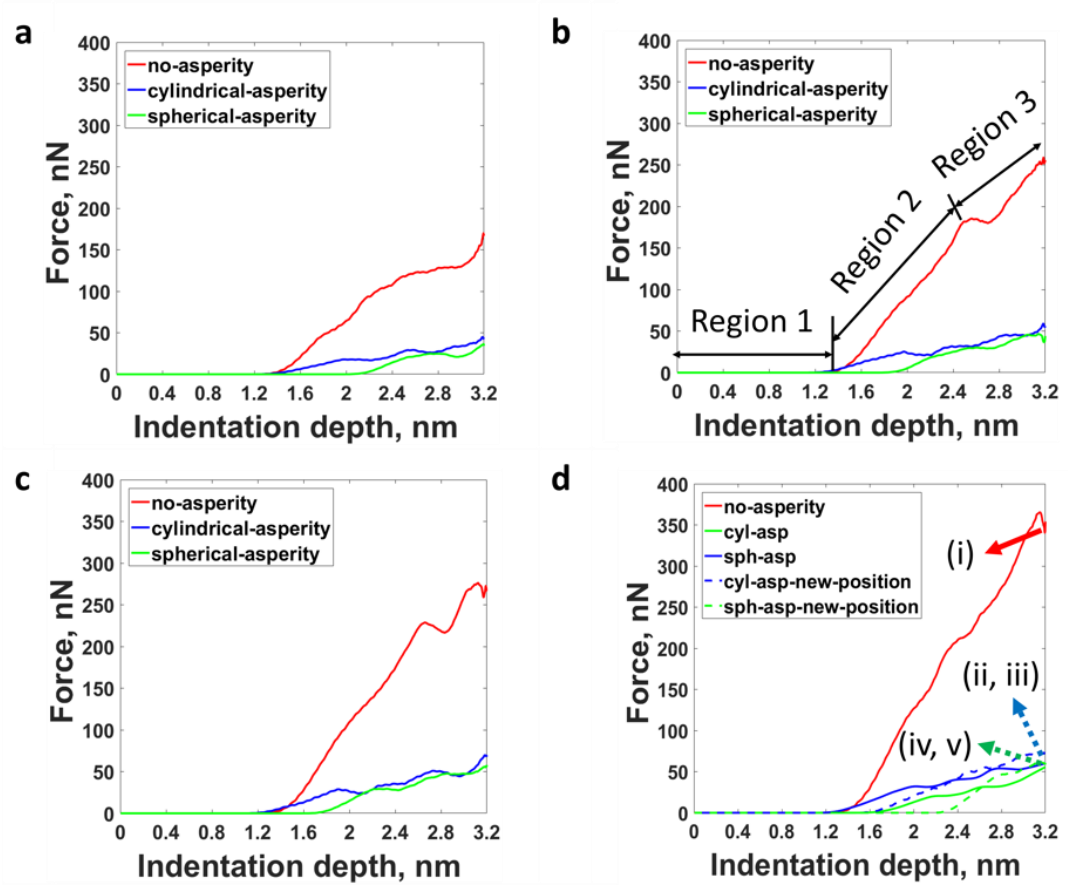

Fig 2. Force vs indentation depth during nanoindentation process for (a) indenter with a radius of 3 nm, (b) indenter with a radius of 4 nm, (c) indenter with a radius of 5 nm and (d) indenter with a radius of 6 nm. With the increase in the indenter radius the critical nanoindentation force increases for samples with and without asperity surfaces. The points i, (ii, iii) and (iv, v) from panel (d) refers to defect microstructures that are shown in more detail in Fig. 4. The dotted lines in the panel (d) corresponds to new indenter location on spherical and cylindrical asperities.

Table 1 Mechanical response of aluminum single crystal substrate with (spherical and cylindrical) and without asperity surface, during nanoindentation with different indenter radii. Critical nanoindentation force increases for with and without asperity surfaces with increase in indenter radius. For indenter radius, less than or equal to 4 nm, the spherical asperity has higher critical nanoindentation force compared to cylindrical asperity and it reverses for indenter radius greater than are equal to 5 nm. Critical nanoindentation force is measured in nN and critical indentation depth is measured in nm.

	Indenter radius	3 nm	4 nm	5 nm	6 nm
No-asperity	Critical Nanoindentation force	143.45	233.67	269.25	389.9
	Critical Indentation depth	2.51	2.58	2.71	3.14
Cylindrical asperity	Critical Nanoindentation force	23.87	35.97	42.44	71.7
	Critical Indentation depth	2.00	2.01	1.93	2.61
Spherical asperity	Critical Nanoindentation force	33.25	37.24	37.22	57.93
	Critical Indentation depth	2.82	2.62	2.32	2.79

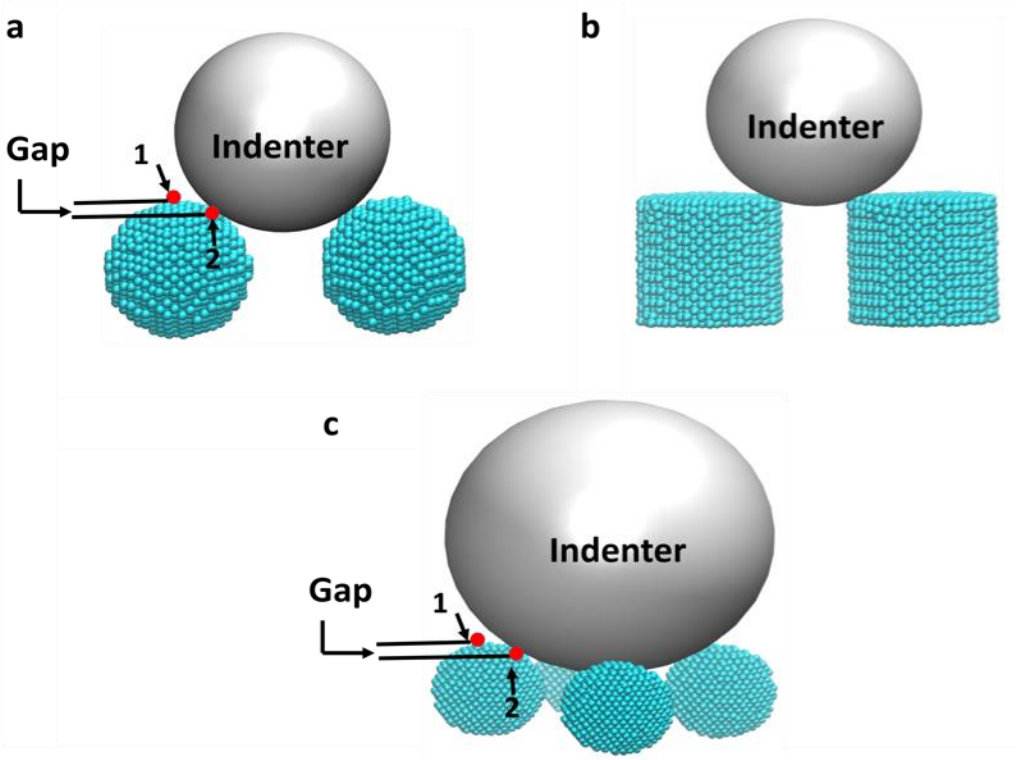

Fig 3. Schematic representation of initial interaction of indenter and the asperity. (a) for indenter of radius 3 nm, touching two spherical asperities, marked by red points 1 and 2. (b) indenter of radius 3 nm, touching two cylindrical asperities. (c) indenter of radius 6 nm, touching four spherical asperities. The gap between points 1 and 2 shows the reason that region 1 is present for greater indentation depth for the spherical asperity compared to cylindrical and no-asperity (shown in Fig. 2). This is because the initial contact point is not exactly at the top surface of spherical asperity. Detailed explanation is given in the results section.

From Fig. 2 we can observe that, with the increase in the indenter radius, the critical nanoindentation force increases, which is consistent with previous studies [35]. The critical nanoindentation force for the no-asperity case is greater than the spherical and cylindrical asperity cases. The critical nanoindentation force for the spherical asperity is greater than that of the cylindrical asperity for indenter radius less than or equal to 4 nm. This trend is reversed for an indenter radius greater than or equal to 5 nm (see Table 1). This is due to the lower the contact area between the indenter and the asperity that leads to higher contact pressure[36]. This also leads to increase in the critical nanoindentation force (see table 1). The spherical asperity has lower

contact area with the indenter compared to cylindrical asperity, when the indenter radius is less than or equal to 4 nm. Therefore, the critical indentation force is higher for the spherical asperity compared to the cylindrical asperity. This trend is reversed because contact area for cylindrical asperity with the indenter is lower than for the spherical asperity when the indenter radius greater than or equal to 5 nm. The increase in the contact area for the spherical asperity can be explained from Fig. 3. i.e., with the increase in indenter radius the gap region is reduced (see Fig.3) hence, contact area increases.

All simulations in this study are displacement controlled. The indenter is displaced 3.2 nm during nanoindentation for all cases (see Fig. 2(a-d)). But we observe region 1 is larger for the spherical asperity compared to the cylindrical and the no-asperity cases. This is because; the initial contact point of indenter on spherical asperity is not exactly at the top of the asperity surface, which is indicated by the gap in Fig. 3 (a, c). The beginning of region 2 is similar for the no-asperity and cylindrical asperity cases, i.e., because the surfaces of the cylindrical asperity and no-asperity are both flat (see Fig. 3 (b)). The gap for the spherical asperity will reduce with the increase in the indenter radius, which implies that region 1 reduces for spherical asperity case as the contact area increases. The reduction in region 1 for the spherical asperity is shown in Fig. 2 (a-d), but in Fig. 2 (d) we can observe that newly positioned 6 nm (indenter center is in between four neighboring asperities) indenter for the spherical and cylindrical asperity has region 1 larger compared to other position of the indenters Fig. 2 (a-d). This is because in Fig. 2 (a-d) when the indenter is touching only two asperities (see Fig. 3 (a, b)) but in Fig. 2 (d) the newly positioned indenter is touching four asperities (see Fig. 3 (c)). The initial gap is more when the indenter is touching four asperities, therefore region 1 is larger compared to other cases (see Fig. 3(c)), but for all cases the indentation depth is ~1.8 nm for both asperity and no asperity surfaces.

The defect microstructure of Al single crystal with and without asperities indented with a newly positioned 6 nm indenter radius is shown in Fig. 4. This microstructure corresponds to the end of the nanoindentation process and the beginning of the scratch process. Fig. 4 shows the evolution of dislocation loops and their Burgers vector which are analyzed using dislocation analysis. Fig. 4 (i), (ii,iii) and (iv,v) correspond to dislocation network for no-asperity, cylindrical asperity and spherical asperity cases respectively. The dislocation network with thin rods are shown in Fig. 4, in which green color rods corresponds to Shockley partial dislocation with 1/6 <1 1 2> Burger vector, blue color rods corresponds to perfect dislocations with ½ < 1 1 0> Burger vector, yellow color corresponds to Hirth dislocation with 1/3< 0 0 1> Burger vector, pink color corresponds to stair-rod dislocation with 1/6 < 1 1 0> Burger vector. Generally, the stair rod dislocation is formed by the glide of dislocations on adjacent slip planes. Due to the dislocation-dislocation interaction and cross slips, prismatic loops are formed during nanoindentation and move into the bulk material. The loops formed would stay in the bulk, because of the non-periodic boundary conditions employed along the *y*-direction. The prismatic loop contains an additional plane of atoms, which transport the material displaced by the indenter. The prismatic loops are only found in the no-asperity case. There are no prismatic loops visible in the cylindrical asperity and spherical asperity cases, the reason could be because of the smaller diameter of the asperities resisting the dislocation-dislocation reaction; or that the loops which are formed in the asperities are moving toward the surface leaving behind the steps on the surface. As shown in Fig. 4 the number of dislocations formed is less for cylindrical and spherical asperity surfaces compared to no-asperity surfaces. We observe similar results for other indenter radii such as 3, 4, and 5 nm. However, for the spherical asperity for indenter radii of 3 and 5 nm and cylindrical asperity with indenter radius of 4nm, we found no dislocation at the end of the nanoindentation process. This is

because the dislocations, which are nucleated as the critical indentation depth is reached, move toward the surface and are annihilated by forming the step on the surface.

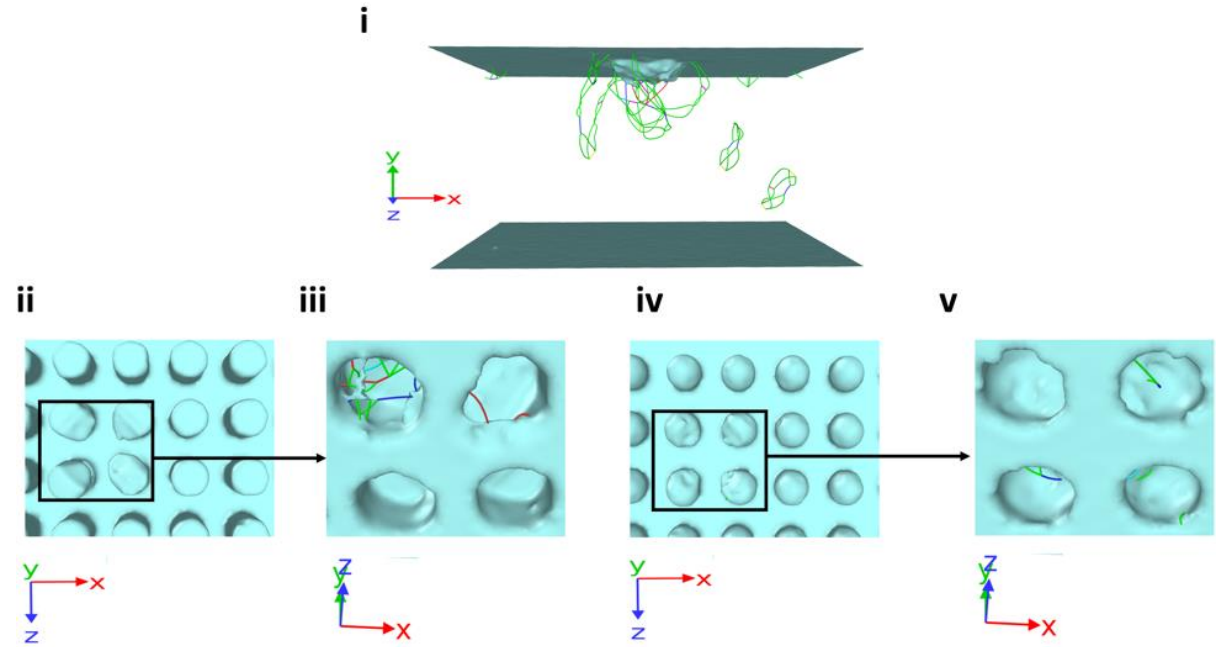

Fig 4. The formation of defect microstructure for 6 nm indenter radius, at the end of nanoindentation (indentation depth is 1.8 nm) and the beginning of scratch process. (i) no asperity case. (ii, iii) cylindrical asperity. (iv, v) spherical asperity. Panels (i, iii, and v) show dislocation formation in aluminum for with and without asperity. The green color rods represent shockley partial dislocation, blue color rod represents perfect dislocation, yellow color represents Hirth dislocation, pink color rod represents stair rod dislocation. Atoms at perfect lattice locations are not shown for better visualization of defects.

After completion of the nanoindentation process with an indentation depth of 1.8 nm, we perform the scratch test on all samples. The scratch tests are performed by moving the indenter along the positive *x* direction with a constant velocity of 5 m/s for about 10 nm. Fig. 5 shows the fluctuations in scratch force for different indenter radii and for surfaces with and without asperities. The scratch force here is the total lateral force exerted on the indenter from the substrate atoms. From Fig. 5 a-d we observe that the scratch force is higher for surfaces without asperities than surfaces with asperities. The scratch force increases significantly with the increase in indenter radius for all the surfaces studied here (Fig. 5 a-d). After reaching the critical scratch length (length

at which dislocation nucleates during scratch), the scratch force starts to fluctuate. It is obvious from Fig. 5a-d that the scratch force for spherical and cylindrical asperity surface fluctuates; this is due to the gap that persists between the asperities at equal intervals. However, with the increase in the indenter radius the fluctuations in scratch force decreases (see Fig. 5 a-d) and for the 6nm indenter radius the fluctuations start at the origin (see Fig. 5d). The corresponding normal force from the indenter during the scratch process is shown in Fig. 6, and it can be noticed that there is a reduction of normal force until the scratch length of the indenter reaches 2 nm; later the force fluctuates at a constant average force value. For the no-asperity case, we also observe that with the increase in the indenter radius from 3 nm to 6 nm, the average constant normal force value increases from 70 nN to 200 nN. Similarly, for the spherical and cylindrical asperity cases the average constant normal force value increases from 20 nN to 70 nN for 3 to 6 nm change in radius. The fluctuations of normal force values for spherical and cylindrical asperity surface decreases as the indenter radius increases. This is because the indenter will encounter the asperity at lower displacements as shown in Fig. 7 (f). Hence, we can conclude that with the increase in the indenter radius or decrease in the distance between the asperities, the fluctuations of the scratch force reduce and have similar scratch force profile as surface without asperities. We also observe negligible difference in scratch force, normal force and COF for 6 nm indenter radius whose center is placed between two and four neighboring asperities respectively.

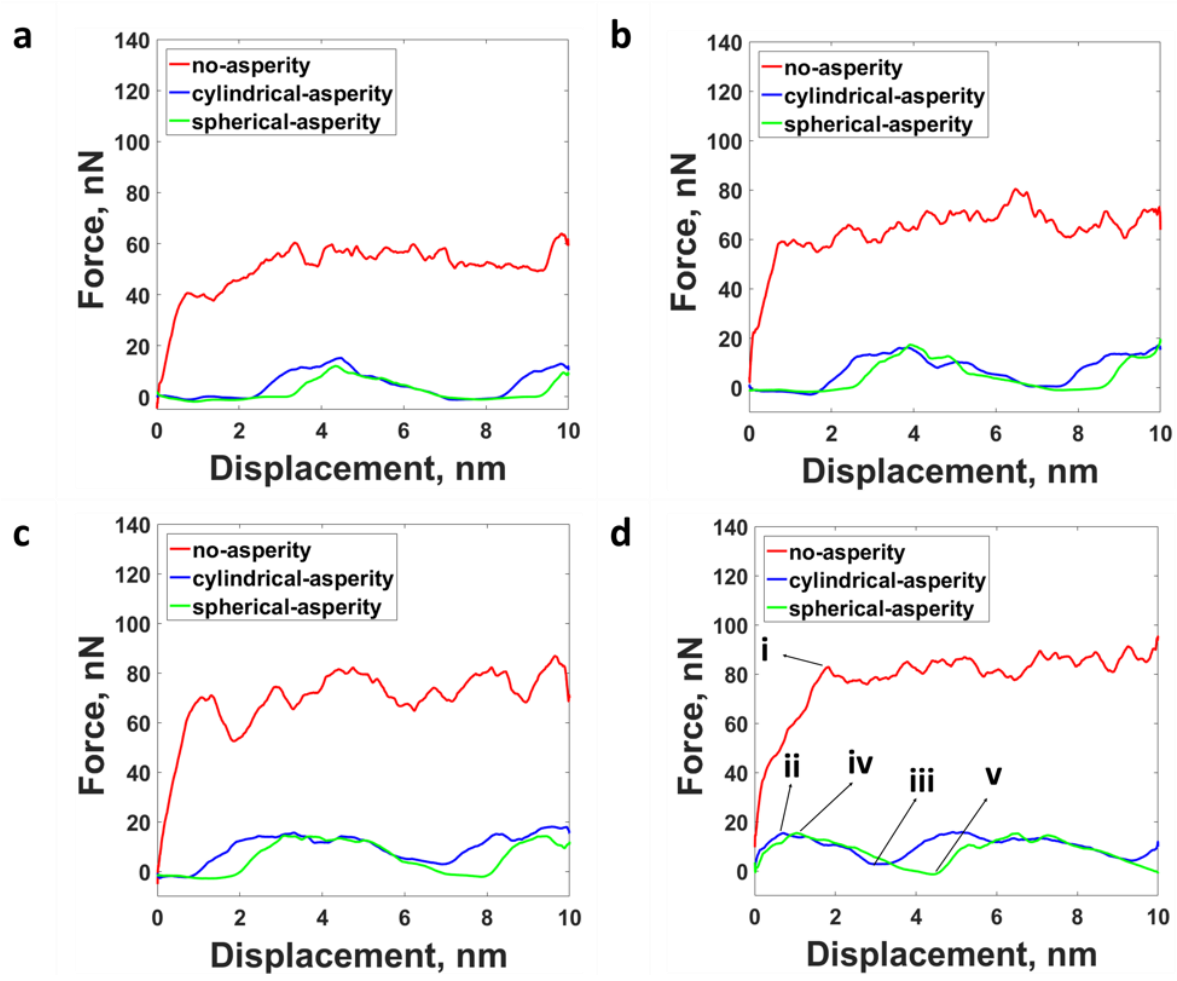

Fig 5. Scratch force vs displacement during the scratch process for indenter with a radius of (a) 3 nm, (b) 4 nm, (c) 5 nm, and (d) 6 nm. The points (i), (ii), (iii) (iv) and (v) in (d) are shown in Fig. 9 which are defect microstructure during the scratch process. With the increase in the indenter radius, average scratch force values increase for samples with and without asperities.

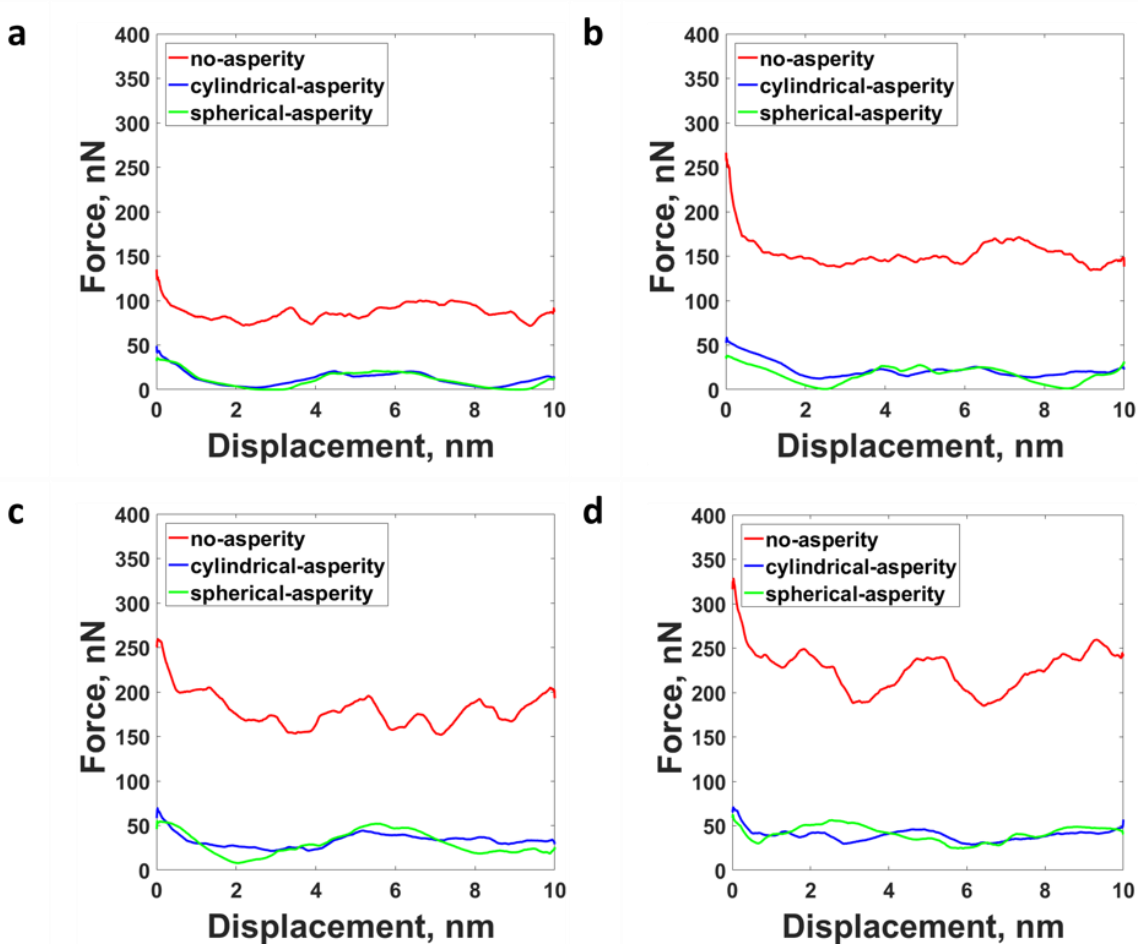

Fig 6. Normal force vs displacement during the scratch process for indenter with a radius of, (a) 3 nm, (b) 4 nm, (c) 5 nm, and (d) 6 nm. With the increase in the indenter radius, average normal force values increase for all samples studied here.

To understand how the COF value varies with the displacement of the indenter during the scratch process. We compute the COF values using the Amontons-Coulomb law under the high load approximation[37] which is the ratio of scratch force to the normal force (see Fig. 7). We observe that the COF values decrease as the indenter radius increases. The average COF value for the no-asperity case is calculated once the COF starts fluctuating around a constant value, seen in Fig. 7. For the spherical and cylindrical cases, the average COF value is calculated using the two highest peaks from Fig. 7. The average COF value decreases from 0.61 to 0.38, 1.71 to 0.41 and 1.16 to 0.5 for no-asperity, cylindrical asperity and spherical asperity respectively, for indenter radius of

3 nm to 6 nm. Komanduri et al (2000) [38] has performed MD simulations of indentation and scratch on single crystal Al surface in various crystal orientations and directions, out of which they found COF for Al is 0.698 for (111) plane and [$\bar{2}$ 1 1] direction (which is similar to the plane and direction we used in our calculations). However, their results prove COF value changes for different crystal orientations and directions. The COF value of 0.61 reported in this paper, for no-asperity case for 3 nm indenter radius is in agreement with Komanduri et al (2000) [38]. We believe the difference is due to the sliding speed, indentation depth, indenter shape and size used by Komanduri et al (2000) [38] are completely different from the current simulations. Similarly, Junge et al (2014)[33] also performed MD simulations on Al surfaces, but predicted the COF is two to three times higher than the current results for the same scratch speed. This could be because Junge et al (2014) has performed the calculations on polycrystalline Al at 0 K where indentation plane is ($\bar{1}$ 1 0) and scratch direction is [$\bar{2}$ 1 1], whereas the current simulations are performed on single crystal Al at 300K where indentation plane is (1 1 1) and scratch direction is [$\bar{2}$ 1 1]. Furthermore, the depth at which indentation and scratch test performed are less than the indentation and scratch depth used in our calculations. This suggests that the COF depends on the temperature, indentation depth as well as the crystallographic plane and the direction of scratch[38]. Furthermore, experimental study conducted by Flom et al (2002) [39] on single crystal Al, have indented Al crystal along the (1 1 1) plane and scratched in different directions. The [2 1 1] scratch direction resulted in a COF of 1.03, which is significantly higher compared than the value predicted in this study. Similarly, Lafaye et al (2006)[40] have found the COF for Al to be approximately 0.6. However, the indenter speed is three order magnitude less than the indenter speed used in the current simulation, and the shape of the indenter is cube cone diamond indenter, whereas we use a spherical indenter. Furthermore, the

size of the sample and indenter used is at the millimeter [39]/micro meter[40] scale, where as our studies are at the nanometer scale.

From Figs. 5 and 6 we observe that increase in normal force is higher than the scratch force as the indenter radius increases, therefore the COF values decreases with increasing indenter radius (Fig 7(a-d)). This reduction in COF values for asperity surfaces with the increase in indenter radius agrees with Zou et al (2005)[41]. However, Zou et al (2005)[41], who used an amorphous silicon substrate, compared to the Al substrate in this study. COF for cylindrical asperity is 47% and 7% higher than spherical asperity for indenter radii 3 and 4 nm respectively; and this reverses for the indenter radii of 5 and 6 nm i.e., COF for spherical asperity is 18% and 22% higher than cylindrical asperity for 5 and 6 nm indenter radius respectively. The shift in COF values between spherical and cylindrical asperities are due to the shift in the contact area between indenter and asperities surfaces.

The negative coefficient of friction for the spherical and cylindrical asperities shown in Fig. 7 is due to the indenter experiencing an opposing force during the start of the scratch process, and also when the indenter encounters a new asperity. Negative COFs have also been observed in experiments [42] as well as in MD simulations [43] and multiscale simulations [44]. Experiments by Ternes, Lutz et al (2008) [42] using AFM to scratch a copper surface with cobalt, did not mention the negative COF, but from their results for lateral and vertical forces, it can be concluded that they have also observed the negative COF, which is similar to conclusions in Mo et al. (2009) [43]. Furthermore, multiscale simulations by Deng et al (2012) [44] have found negative COF at the nanoscale and is adhesion dependent.

It should be noted that in the first three cases in Fig. 7 a-c, the indenter is in contact with two asperities and for the last case in Fig. 7 d, the indenter is in contact with four asperities. These

asperities are deformed initially during nanoindentation and when the scratch starts on the completely deformed asperities the scratch force decreases initially, and then increases when the indenter encounters the neighboring asperities. Therefore, with the increase in the indenter radius the scratch force increases because the contact area increases between the indenter and asperities. For the 6 nm indenter radius, the scratch force is positive for the cylindrical asperity and is a small and negative scratch force for the spherical asperity (see Fig. 5 d), this is because the spherical asperities are deformed more compared to cylindrical asperities. This results in a positive coefficient of friction for the cylindrical asperity, but has a smaller negative COF for the spherical asperity case, because the indenter needs to be displaced more for the spherical asperity compared to the cylindrical asperity to meet the neighboring asperities, see Fig 7 e and f.

With these observations, we can estimate that with further increase in the indenter radius or reducing the gap between the asperities, we can overcome the negative COF. From the results, we see that (Fig 7(a-d)) the difference in COF for asperity and no-asperity cases is decreasing with the increase in the indenter radius. But for the 6 nm indenter radius, the COF for the cylindrical asperity case is almost equal to the no-asperity case. In order to test the trend in COF values with respect to the indenter radaii, we conduct a scratch test using 10 nm indenter radius. We find that the COF values for the asperity surfaces is slightely lower than the no-asperity case (see Fig 8). We believe that with further increase in the indenter radius the COF will further reduces compared to no-asperity case. Experimental studies also show that with the increase in roughness the COF [41] will decrease. But this study shows that the nanoscale roughness has a limit, which means below certain nanoscale roughness the COF will increase compared to smooth surface. From the current studies, we conclude that if the asperity radius is 2 nm then the indenter size should be more than 6 nm to lower the COF compared to the no-asperity case. Furthermore, we can conclude that for

the indenter with radius lower than 4 nm, we observe that the COF for the spherical asperity is lower than the cylindrical asperity. For indenter with radius greater than or equal to 5nm the cylindrical asperity has lower COF than the spherical asperity. We have also performed nanoindentation and scratch simulations for two additional asperity spacing (1 nm and 3 nm) with an indenter radius of 6 nm, keeping same indentation depth (1.8 nm) and doubled the scratch length (here, 20 nm). The results of this study show that with the increase in the distance between the asperities, the COF increases (see Fig 9), which is in agreement with the results obtained for the decrease in the indenter size. As the distance between the asperities increases for constant indenter radius (here, 6nm) the contact area between the indenter and the asperities decreases, which is comparable to the decrease in the indenter radius with constant asperity distance (here, 2 nm). Similar trend of the results were observed in Tong et al (2011)[26] by changing the distance between the asperities for copper. From Fig 9 we see that the highest values of COF for respective scratch tests would not vary much and the difference is less than 5%. Similar trend is observed by Tong et al (2011)[26], hence it is clear that the COF variation cycle is almost the same when the indenter encounters a new asperity, which leads to minimal difference in COF even if we run scratch test for shorter distance covering fewer asperities. Therefore, considering the computational time, we could use a scratch distance of 10 nm for all other samples. This study could perhaps be useful for designing surfaces with nanoscale multi-asperities that are interacting with each other. For example, a surface can be developed with a targeted COF value based on the asperity radius on each surface.

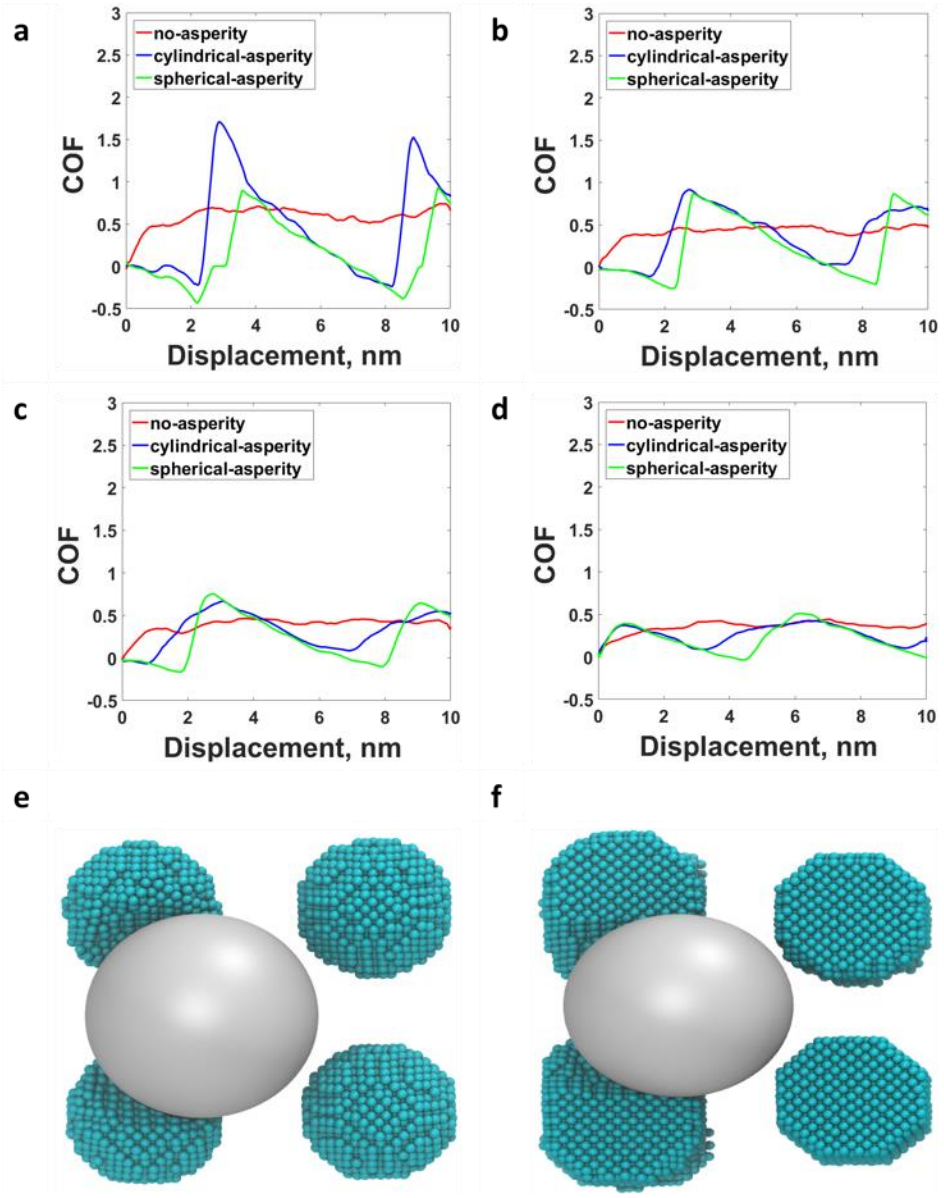

Fig 7. Variation of the coefficient of friction (COF) vs displacement during the scratch process for indenter with a radius of (a) 3 nm, (b) 4 nm, (c) 5 nm and (d) 6 nm. The coefficient of friction decreases with the increase in indenter radius. (e, f) Schematic representation of interaction between indenter (radius 4 nm) and the asperity during the scratch process for, (e) spherical asperity, (f) cylindrical asperity. This explains the reason for the fluctuations in COF values.

Finally, we investigate the dislocation loops and surface pileup evolutions during the scratch process (see Fig. 10). We can observe that as the scratch process evolves, new dislocations (prismatic loops) are emitted in front of the indenter for no-asperity case (shown in Fig. 10 (b &

d)). These loops are propagating parallel to the indenter direction. The half loops with their screw segments gliding on the surface produce a surface step as shown in Fig. 10 (c). Similar to the nanoindentation process, the prismatic loops are not found in cylindrical and spherical asperity surfaces. The reason for this is that the asperity diameter is smaller which is resisting the formation of the loops. Even if the loops are formed, they move to the surface of the asperity forming the surface steps on the asperity surface as shown in Fig. 10 (k & s). From Fig 11 (a-d), we observe that the spherical and cylindrical asperity surfaces for different indenter radii, after certain scratch distance dislocation segments are not found, even though there were dislocation segments present before. This explains that the dislocations moved to the surface during the scratch process forming surface steps (seen in Fig 10 (g,k,o,s)). Similarly, we observe the surface step formation for no-asperity surface with different radii (see Fig 11 (a-d), and Fig 10c). We also observe that there is increase in total number of dislocation segments compared to previous time step during scratch process, this is due to the formation of new dislocation segments during the scratch test. For the spherical (Fig 11 a,c) and cylindrical asperity (Fig 11 b,c) surfaces, we observe no dislocations before the the scratch process begins, this is due to the fact that the dislocations formed during the indentation process have moved toward the surface at the end of the indentation process. The microstructure of the first trough part of the fluctuation shown in Fig. 5d are represented in Fig. 10(i-l & q-t) where the scratch force is minimum and the indenter is about to deform the next neighboring asperity. At this point as the scratch force goes to a minimum, the dislocation density decreases compared to the crest of the curve, which is the initiation of dislocation nucleation during the scratch process. This reduction in dislocations are found in both spherical and cylindrical asperity surfaces, which are shown in Fig. 11. It is expected that total number of dislocation segments should increase as the scratch process proceeds, but from Fig. 11, we observe the

dislocation segments evolution is random. This is because, some of the dislocation formed in the scratch process moves to the surface forming surface step, shown in Fig. 10 (c,g,k,o,s).

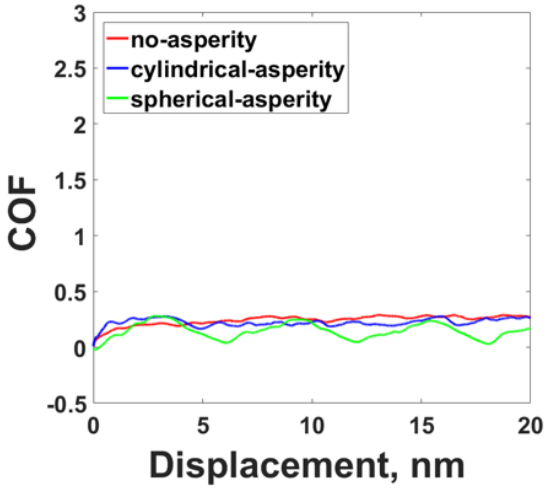

Fig 8. Variation of the coefficient of friction (COF) vs displacement during the scratch process for 10 nm indenter radius.

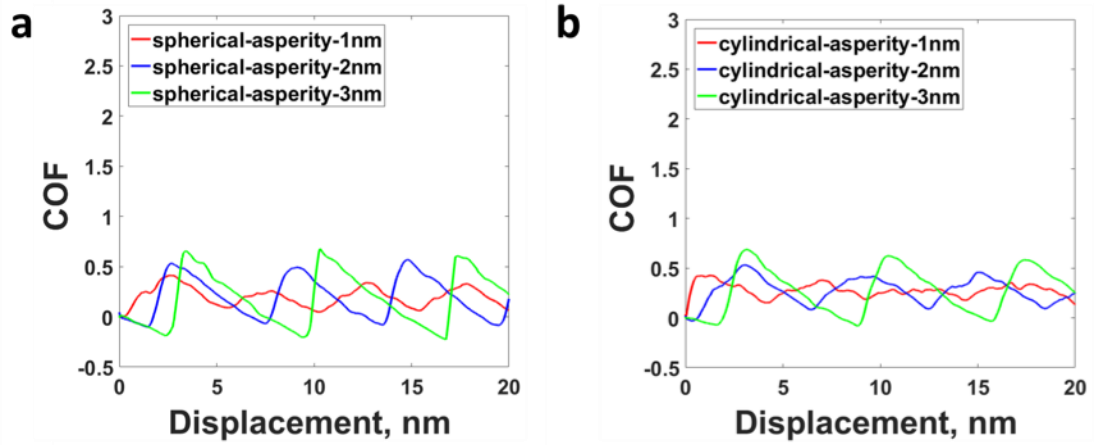

Fig 9. Variation of the coefficient of friction (COF) vs displacement during the scratch process for an indenter of radius 6nm with different spacing between the asperities. The 1 nm, 2 nm and 3 nm represents the distance between the asperities for (a) Spherical asperities (b) Cylindrical asperities respectively.

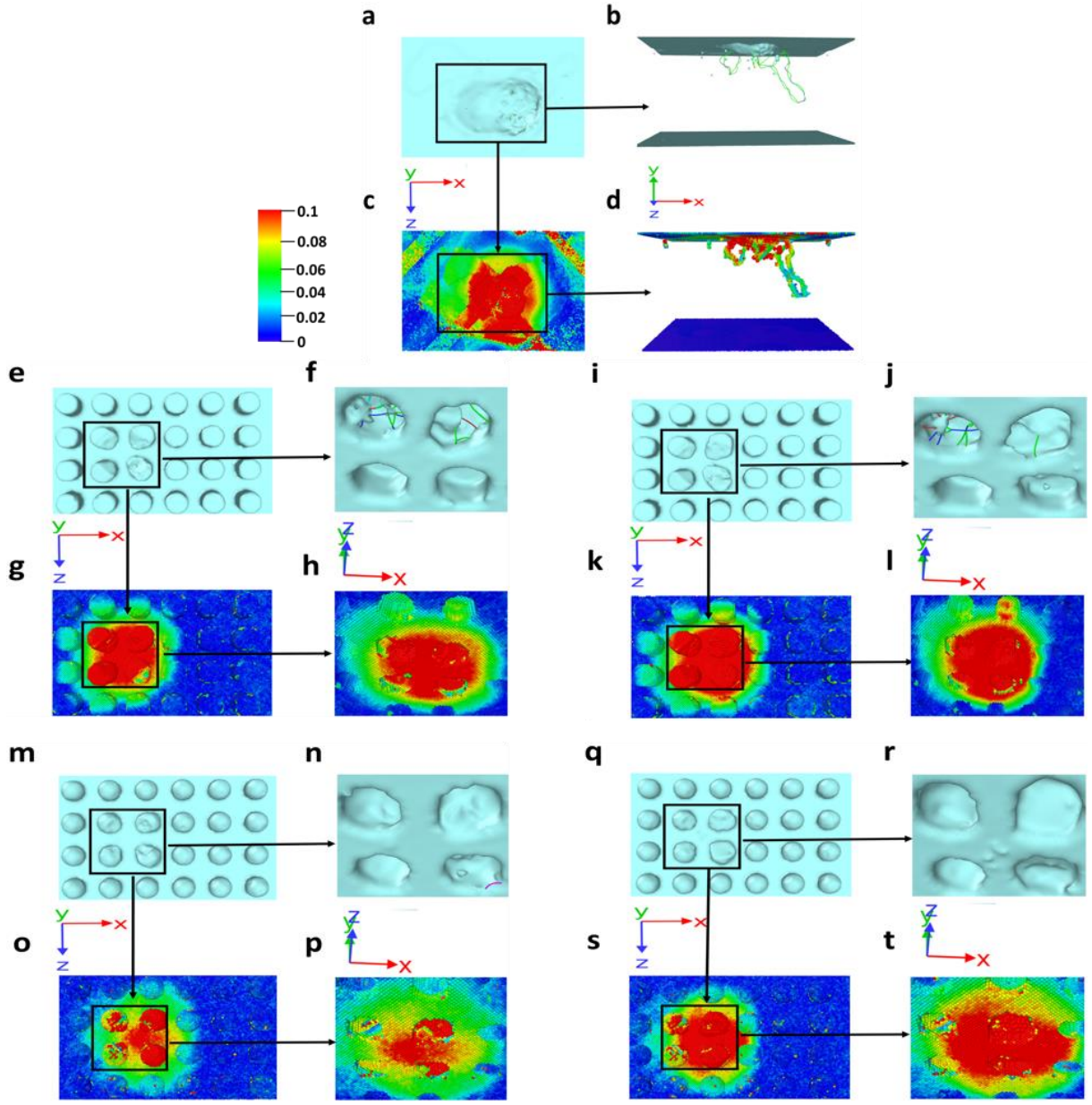

Fig 10. The snapshot of defect microstructure taken using OVITO for 6 nm indenter radius, during the scratch process. (a – d) for no asperity case. (e – l) cylindrical asperity case. (m – t) spherical asperity case respectively. (a-d) corresponds to (i) in Fig. 5, (e-h) corresponds to (ii) in Fig. 5, (i-l) corresponds to (iii) in Fig. 5, (m-p) corresponds to (iv) in Fig. 5, (q-t) corresponds to (v) in Fig. 5. The color bar represents the atomic strain, where 0 correspond to no strain (blue) and 0.1 (red) correspond to the maximum strain, as shown in (c-d, g-h, k-l, o-p, s-t). Dislocations seen in (b, f, j, n) represents the no-asperity and asperity surfaces and are plastically deformed. No dislocation is observed in (r) even though the asperity is plastically deformed because the dislocations moved on to the surface. Atoms at perfect lattice locations are not shown for better visualization of defects.

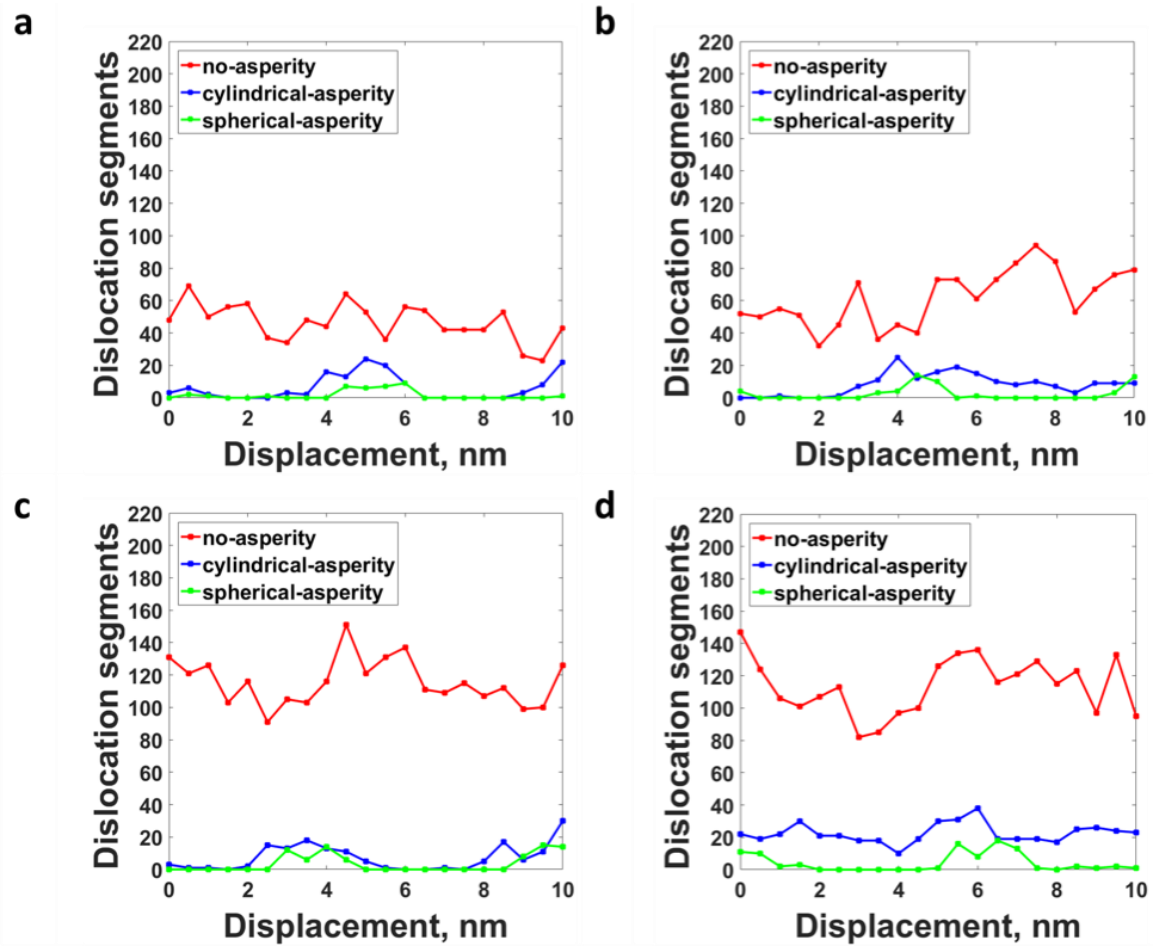

Fig 11. Total number of dislocation segments evolved during scratch process for indenter radius of (a) 3nm. (b) 4nm, (c) 5nm, and (d) 6nm. Dislocation formation represents the plastic deformation, from the graph we can say that the surface with and without asperities have plastically deformed.

2.4 Conclusions

In this study, we perform molecular dynamics simulations to understand the variation of COF with different indenter radii, for single crystal aluminium with asperities (spherical and cylindrical) and without asperity surfaces. We also examine the evolution of microstructure during the nanoindentation and scratch process. Our results show that the nanoindentation force, scratch force and constant average normal force increases as the indenter radius increases, but the increase in scratch force is much lower compared to the normal force. This suggests that the COF decreases

with the increase in the indenter radius. We found that the COF is lower for spherical asperity surfaces, if the indenter radius is less than or equal to 4 nm; and COF is lower for cylindrical asperity surfaces, if the indenter radius is greater than or equal to 5 nm. This is because for indenter radius less than or equal to 4 nm the spherical asperity has lower contact area between the indenter and the asperities compared to cylindrical asperities; this trend reverses when the indenter radius is greater than or equal to 5 nm. Moreover, our results show that a smooth surface has higher frictional force and lower COF for indenter radius less than 6 nm, when we compare with asperity surfaces (frictional force is lower). The average COF for the asperity surfaces are approximately equal or lower than the smooth surface, if the indenter radius is greater than 6 nm. This leads to the conclusion that with an appropriate indenter and asperity sizes (or two interacting surfaces), we can make surfaces with lower COF compared to smooth surfaces. Higher frictional force on smooth surface could lead to surface fracture [26]. Therefore, surface texture (asperities) would help in reducing the frictional force at the nanoscale. The prismatic loops are observed in no-asperity case but not in cylindrical and spherical asperity surface cases. Surfaces with and without asperities are found with the formation of surface steps because the dislocation loops move toward the surface during the scratch process. The computational models developed in this study and the results from this study could guide the experiments in designing surfaces at the nanoscale. For example, to design two interacting surfaces with a targeted COF value, the nanoscale asperity size and shape can be preselected. This is especially useful for bio-inspired surfaces that have multiple applications. Future work include studying different asperity and indenter radii to find the general trend between asperity size and indenter size to reduce frictional properties. Furthermore future studies also include asperities with core-shell structures and how the thickness of core and shell affect the frictional properties.

Acknowledgements

We sincerely thank the Center for Advanced Surface Engineering, under the National Science Foundation Grant No. IIA-1457888 and the Arkansas EPSCoR Program, ASSET III, Funding for this research. Authors would like to acknowledge the support in part by the National Science Foundation under the grants ARI#0963249, MRI#0959124 and EPS#0918970, and a grant from Arkansas Science and Technology Authority, managed by Arkansas High Performance Computing Center.

References

1. A. Pimpin and W. Srituravanich: Review on micro-and nanolithography techniques and their applications *Engineering Journal.* **16**(1), 37 (2011).

2. J. Park, D.-H. Kim, H.-N. Kim, C.J. Wang, M.K. Kwak, E. Hur, K.-Y. Suh, S.S. An and A. Levchenko: Directed migration of cancer cells guided by the graded texture of the underlying matrix *Nature materials.* (2016).

3. E. Spedden, M.R. Wiens, M.C. Demirel and C. Staii: Effects of surface asymmetry on neuronal growth *PloS one.* **9**(9), e106709 (2014).

4. L. Garion, U. Dubin, Y. Rubin, M. Khateb, Y. Schiller, R. Azouz and J. Schiller: Texture coarseness responsive neurons and their mapping in layer 2–3 of the rat barrel cortex in vivo *Elife.* **3**, e03405 (2014).

5. H. Hertz: Über die Berührung fester elastischer Körper *Journal für die reine und angewandte Mathematik.* **92**, 156 (1882).

6. B.V. Derjaguin, V.M. Muller and Y.P. Toporov: Effect of contact deformations on the adhesion of particles *Journal of Colloid and interface science.* **53**(2), 314 (1975).

7. K. Johnson, K. Kendall and A. Roberts: Surface energy and the contact of elastic solids, in Proceedings of the Royal Society of London A: Mathematical, Physical and Engineering Sciences, (**324**, The Royal Society, City, 1971), pp. 301.

8. D. Maugis: Adhesion of spheres: the JKR-DMT transition using a Dugdale model *Journal of colloid and interface science.* **150**(1), 243 (1992).

9. B. Luan and M.O. Robbins: The breakdown of continuum models for mechanical contacts *Nature.* **435**(7044), 929 (2005).

10. R. Maboudian and R.T. Howe: Critical review: Adhesion in surface micromechanical structures *J Vac Sci Technol B.* **15**(1), 1 (1997).

11. B. Bhushan, J.N. Israelachvili and U. Landman: Nanotribology: friction, wear and lubrication at the atomic scale *Nature.* **374**(6523), 607 (1995).

12. A.K. Nair, M. Cordill, D. Farkas and W. Gerberich: Nanoindentation of thin films: Simulations and experiments *Journal of Materials Research.* **24**(03), 1135 (2009).

13. A.K. Nair, E. Parker, P. Gaudreau, D. Farkas and R.D. Kriz: Size effects in indentation response of thin films at the nanoscale: A molecular dynamics study *International Journal of Plasticity.* **24**(11), 2016 (2008).

14. Y. Zhao, X. Peng, T. Fu, C. Huang, C. Feng, D. Yin and Z. Wang: Molecular dynamics simulation of nano-indentation of (111) cubic boron nitride with optimized Tersoff potential *Applied Surface Science.* **382**, 309 (2016).

15. Y. Gao and H.M. Urbassek: Scratching of nanocrystalline metals: A molecular dynamics study of Fe *Applied Surface Science.* **389**, 688 (2016).

16. J. Li, J. Guo, H. Luo, Q. Fang, H. Wu, L. Zhang and Y. Liu: Study of nanoindentation mechanical response of nanocrystalline structures using molecular dynamics simulations *Applied Surface Science.* **364**, 190 (2016).

17. C. Hu, M. Bai, J. Lv, H. Liu and X. Li: Molecular dynamics investigation of the effect of copper nanoparticle on the solid contact between friction surfaces *Applied Surface Science.* **321**, 302 (2014).

18. L. Si and X. Wang: Nano-adhesion influenced by atomic-scale asperities: A molecular dynamics simulation study *Applied Surface Science.* **317**, 710 (2014).

19. C. Qiu, P. Zhu, F. Fang, D. Yuan and X. Shen: Study of nanoindentation behavior of amorphous alloy using molecular dynamics *Applied Surface Science.* **305**, 101 (2014).

20. T.D. Jacobs, K.E. Ryan, P.L. Keating, D.S. Grierson, J.A. Lefever, K.T. Turner, J.A. Harrison and R.W. Carpick: The effect of atomic-scale roughness on the adhesion of nanoscale asperities: A combined simulation and experimental investigation *Tribology Letters.* **50**(1), 81 (2013).

21. W. Cheong and L. Zhang: Monocrystalline silicon subjected to multi-asperity sliding: nano-wear mechanisms, subsurface damage and effect of asperity interaction *International Journal of Materials and Product Technology.* **18**(4-6), 398 (2003).

22. P.-R. Cha, D.J. Srolovitz and T.K. Vanderlick: Molecular dynamics simulation of single asperity contact *Acta Materialia.* **52**(13), 3983 (2004).

23. T. Liu, G. Liu, P. Wriggers and S. Zhu: Study on contact characteristic of nanoscale asperities by using molecular dynamics simulations *Journal of Tribology.* **131**(2), 022001 (2009).

24. R. H: Particle Technology *Chapman & Hall, London.* (1990).

25. Y.I. Rabinovich, J.J. Adler, A. Ata, R.K. Singh and B.M. Moudgil: Adhesion between nanoscale rough surfaces: I. Role of asperity geometry *Journal of Colloid and Interface Science.* **232**(1), 10 (2000).

26. R.T. Tong, G. Liu and T.X. Liu: Multiscale Analysis on Two Dimensional Nanoscale Sliding Contacts of Textured Surfaces *Journal of Tribology-Transactions of the Asme.* **133**(4), 041401 (2011).

27. R. Tong, G. Liu and L. Liu: Multiscale analysis on two-dimensional nanoscale adhesive contacts *Chinese Journal of Mechanical Engineering.* **25**(3), 446 (2012).

28. P. Zhu, Y. Hu and H. Wang: A hybrid model for multiscale simulations of nanoindentation *Proceedings of the Institution of Mechanical Engineers, Part J: Journal of Engineering Tribology.* **225**(8), 845 (2011).

29. G. Anciaux and J.-F. Molinari: Sliding of rough surfaces and energy dissipation with a 3D multiscale approach *International Journal for Numerical Methods in Engineering.* **83**(8-9), 1255 (2010).

30. J. Winey, A. Kubota and Y. Gupta: Thermodynamic approach to determine accurate potentials for molecular dynamics simulations: thermoelastic response of aluminum *Modelling and Simulation in Materials Science and Engineering.* **18**(2), 029801 (2010).

31. S. Plimpton: Fast parallel algorithms for short-range molecular dynamics *Journal of computational physics.* **117**(1), 1 (1995).

32. A. Stukowski: Visualization and analysis of atomistic simulation data with OVITO–the Open Visualization Tool *Modelling and Simulation in Materials Science and Engineering.* **18**(1), 015012 (2009).

33. T. Junge and J.-F. Molinari: Plastic activity in nanoscratch molecular dynamics simulations of pure aluminium *International Journal of Plasticity.* **53**, 90 (2014).

34. C. Begau, A. Hartmaier, E.P. George and G.M. Pharr: Atomistic processes of dislocation generation and plastic deformation during nanoindentation *Acta Materialia.* **59**(3), 934 (2011).

35. Z. Li, Y. Huang, J. Zhang, Y. Yan and T. Sun: Atomistic insight into the minimum wear depth of Cu (111) surface *Nanoscale research letters.* **8**(1), 1 (2013).

36. G. Ziegenhain, H.M. Urbassek and A. Hartmaier: Influence of crystal anisotropy on elastic deformation and onset of plasticity in nanoindentation: a simulational study *Journal of Applied Physics.* **107**(6), 061807 (2010).

37. J.P. Ewen, C. Gattinoni, F.M. Thakkar, N. Morgan, H.A. Spikes and D. Dini: Nonequilibrium molecular dynamics investigation of the reduction in friction and wear by carbon nanoparticles between iron surfaces *Tribology Letters.* **63**(3), 38 (2016).

38. R. Komanduri, N. Chandrasekaran and L. Raff: MD simulation of indentation and scratching of single crystal aluminum *Wear.* **240**(1), 113 (2000).

39. D.G. Flom and R. Komanduri: Some indentation and sliding experiments on single crystal and polycrystalline materials *Wear.* **252**(5), 401 (2002).

40. S. Lafaye and M. Troyon: On the friction behaviour in nanoscratch testing *wear.* **261**(7), 905 (2006).

41. M. Zou, L. Cai, H. Wang, D. Yang and T. Wyrobek: Adhesion and friction studies of a selectively micro/nano-textured surface produced by UV assisted crystallization of amorphous silicon *Tribology Letters.* **20**(1), 43 (2005).

42. M. Ternes, C.P. Lutz, C.F. Hirjibehedin, F.J. Giessibl and A.J. Heinrich: The force needed to move an atom on a surface *Science.* **319**(5866), 1066 (2008).

43. Y. Mo, K.T. Turner and I. Szlufarska: Friction laws at the nanoscale *Nature.* **457**(7233), 1116 (2009).

44. Z. Deng, A. Smolyanitsky, Q. Li, X.-Q. Feng and R.J. Cannara: Adhesion-dependent negative friction coefficient on chemically modified graphite at the nanoscale *Nature materials.* **11**(12), 1032 (2012).

Chapter 3

3. Paper 2: Mechanical behavior of core-shell nanostructures

Raghuram Reddy Santhapuram, Douglas E. Spearot, Arun K Nair

Abstract

Nanotexturing reduces the effective contact between surfaces in relative motion, which can result in a lower coefficient of friction. However, nanotextured surfaces lack structural integrity, resulting in permanent deformation even at moderate contact forces. Therefore, core-shell nanostructures (CSNs) have been developed to protect the structural integrity of nanotextured surfaces. These CSNs can withstand higher contact forces, might include some plastic deformation (dislocations), but during unloading there is no evidence of residual plastic deformation. Therefore, the CSN is deformation resistant. In the current study, molecular dynamics simulations are used to study the effect of core (aluminum) radius, shell (amorphous-silicon) thickness, and the random atomic distribution in the amorphous shell, on mechanical properties of core-shell nanostructures. The results suggest that core radius does not have a significant influence on the initial plastic deformation of the CSN. The shell thickness should be chosen so that the core to shell ratio is less than two to have deformation resistant CSNs. Further we observe that with an increase in core radii or shell thickness, the ability of a CSN to fully recover decreases. These results will help in the design of deformation resistant surfaces for MEMS/NEMS applications.

Keywords: Core shell nanostructures, Dislocation starvation, Strain hardening

3.1 Introduction

Due to their large surface to volume ratios, micro-electro-mechanical systems (MEMS) and nano-electro-mechanical systems (NEMS) devices experience high capillary forces, electrostatic forces and van der Waals forces. Therefore, MEMS/NEMS are vulnerable to failure mechanisms such as friction, stiction, adhesion and wear [1-5]. To combat these failure mechanisms, volume confined materials such as nanoparticles, nanopillars, composite nanoparticles and core-shell nanoparticles have been incorporated into the design of MEMS/NEMS. For example, recent study [3] has shown that nanotextured surfaces with core-shell nanostructures significantly enhanced the fatigue resistance of the nanostructure without any evidence of plastic deformation. However, the dependency between core radius and shell thickness was not explored, i.e., what would be the optimal shell thickness for a given core radius that would evidently protect the core-shell nanostructure from plastic deformation? Therefore, our objective is to understand the effect of the ratio of the core radii to shell thickness undergoing plastic deformation.

Several studies based on experiments [6], analytical and numerical simulations [7, 8] have been performed to understand the physical mechanisms associated with plasticity in nanoscale domains, which is necessary to understand the deformation of core-shell nanostructures (CSN). Dislocation starvation is prominent among several other mechanisms. This concept is used to describe strengthening of a nanosized crystal that contains fewer dislocations compared to the bulk material. Plasticity at the nanoscale could be delayed until a few dislocations get nucleated. The initial starvation is more significant as the crystal size reduces.

Another important perspective related to nanoscale plasticity is the evidence of reverse plasticity. Reverse plasticity is a nanoscale phenomenon in which dislocations migrate to a surface or an interface and are removed during unloading. This phenomenon is observed in nanoparticles during

a micro compression test [9]. During the compression test of nanoparticles, inelastic deformation requires higher stresses whereas recovery (reverse plasticity) is observed at lower loads. This is observed in both single phase nanoparticles and composite nanoparticles [10, 11].

The current study focuses on the deformation of core-shell nanostructures and provides a dislocation-based understanding of the effect of core radius to shell thickness ratio under plastic deformation. Specifically, we use molecular dynamics (MD) method to predict the mechanical properties of an Al core coated with amorphous Si shell under nanoindentation. Further, in this study, we explore and quantify microscopic deformation mechanisms such as dislocation nucleation, propagation, and recovery along with stress distribution in the core and shell of the core-shell nanostructures. Dislocation evolution in CSNs help us to understand the structure property relations at the nanoscale. This is analogous to dislocation starvation state and hence the high strength of CSNs. The novelty of this research is to predict the presence of dislocation starvation mechanism present in CSNs, and the optimization of core radius to shell thickness of the CSNs that would most effectively behave as deformation resistant.

3.2 Materials and method

We perform nanoindentation and retraction tests using the Large Scale Atomic/Molecular Massively Parallel Simulator (LAMMPS) [12] to understand how the core radius to shell thickness ratio affects the plasticity within core-shell nanostructures (Fig.1). We study samples with a core radius of R = 10 or 30 nm, where for each core radius, the shell thickness variation is t = 5, 10 or 20 nm. The core consists of aluminum (Al), where the crystal structure is oriented along the x $[11\bar{2}]$, y [111] and z $[1\bar{1}0]$ directions, respectively, and the shell consists of amorphous silicon (a-Si). An amorphous silicon layer is generated by randomly and uniformly distributing silicon atoms in the defined shell region [13], and then energy minimization is performed using the conjugate

gradient method so that Si atoms can find local minimum energy positions. The number of Si atoms that are randomly distributed is calculated from the total number of crystalline Si that would fit in the given region. We use a rigid spherical indenter of 100 nm radius composed of Al atoms. The indenter is displaced using a force-based method to perform the nanoindentation and retraction process. A 10 nN (negative) force is added to the indenter every 500 ps, which displaces the indenter and deforms the core-shell nanostructure. Similarly, during retraction of the indenter, we add a 10 nN (positive) force every 500 ps. The MD simulations are performed at a temperature of 300 K and employ a modified embedded atom method (MEAM) interatomic potential [14]. This potential [14] shows excellent agreement of generalized stacking fault energy curves for Al and Si when compared with ab initio calculations. MEAM parameters for the element pair were formulated using a reference NaCl structure to generate stable binary compounds and are validated with ab initio calculations and experiments. Further, this potential has been used for calculating mechanical properties of core-shell nanostructures (deformation resistance) for binary compounds [15, 16], hybrid welded joints [17], and metastable phases during age hardening of tertiary compounds [18, 19].

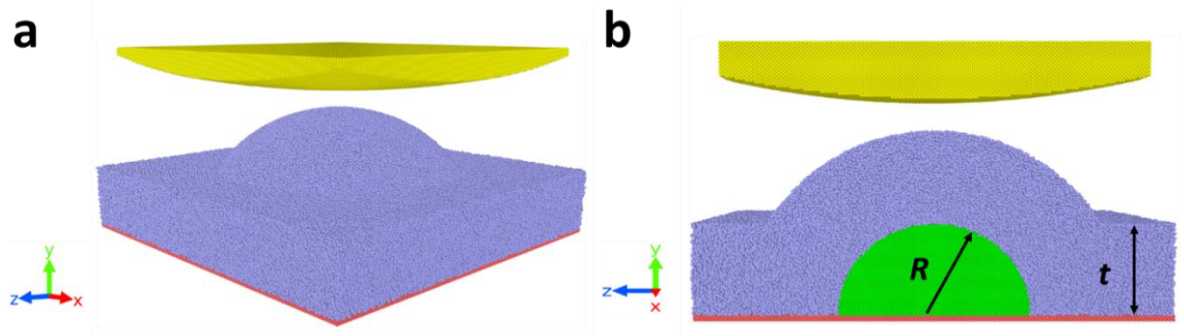

Fig 1. (a) Core-shell nanostructure with rigid Al indenter (b) Cross-sectional view of the core-shell nanostructure. Red, green and blue color atoms represent Al substrate, Al core, and a-Si shell respectively. The yellow color atoms represent a rigid indenter. Different core radius (*R*) and shell thickness (*t*) used in this study varies as *R*= 10 and 30 nm, and *t*= 5, 10, 20 nm.

Periodic boundary conditions are implemented along the *x*, *z* directions and a nonperiodic boundary condition is employed along the *y* direction. Several atomic planes (red color atoms) are held fixed at the bottom of the samples, as shown in Fig. 1. All samples are subjected to energy minimization using the conjugate gradient method. Following this, samples are equilibrated at 300 K using the isothermal and isobaric ensemble (NPT) for 300 ps while maintaining zero pressure along periodic directions. OVITO [20] is used to perform common neighbor analysis and dislocation analysis (DXA), which helps to visualize defects including dislocations, stacking faults and the distribution of stress in the core and shell generated during nanoindentation. The stresses in the samples are calculated using virial stress, as defined by Thompson et al. [21].

3.3 Results and discussion

Force based nanoindentation tests are performed on six CSN samples that consist of two different core radii and three different shell thicknesses. For the 10 nm core radius, we use three different seed parameters for the random atom distribution in the shell and find that the simulation method demonstrates good reproducibility under nanoindentation, with less than 5% difference in the force versus displacement behavior, indentation depth at first dislocation and stress at first dislocation for respective shell thickness of core-shell nanostructures. The force-displacement plot for the 10 nm core and 5 nm shell thickness is shown in Fig. 2(a). It is divided into three regions: a linear elastic response (region 1), plastic response with low hardening rate (region 2) and plastic response with high hardening rate (region 3). As indicated, region 2 is where the plastic deformation response of the CSN initiates. Points 1, 2 and 3 indicate the dislocation nucleation point and propagation into the core, respectively. The corresponding displacement magnitude and dislocation analysis images are also shown in Fig. 2(a). The core-shell interface clearly serves as the source for dislocation nucleation.

Further, points 4 and 5 in region 3 correspond to high hardening rate and this can be clearly seen in DXA images of the corresponding points with an increase in the number of dislocation segments in the core of the CSN. Note, the drop in the force in region 1 (see Fig. 2(a)) is due to the accumulation of back-stress in CSN. The increase in back-stress in the CSN forced the indenter to bounce back (unload) during force controlled nanoindentation. Similar behavior is observed in other samples as well (see Fig. 2(b)). However, this behavior is not observed as the nanoindentation depth increases because the load applied to the indenter is more than the back-stress developed within the CSN.

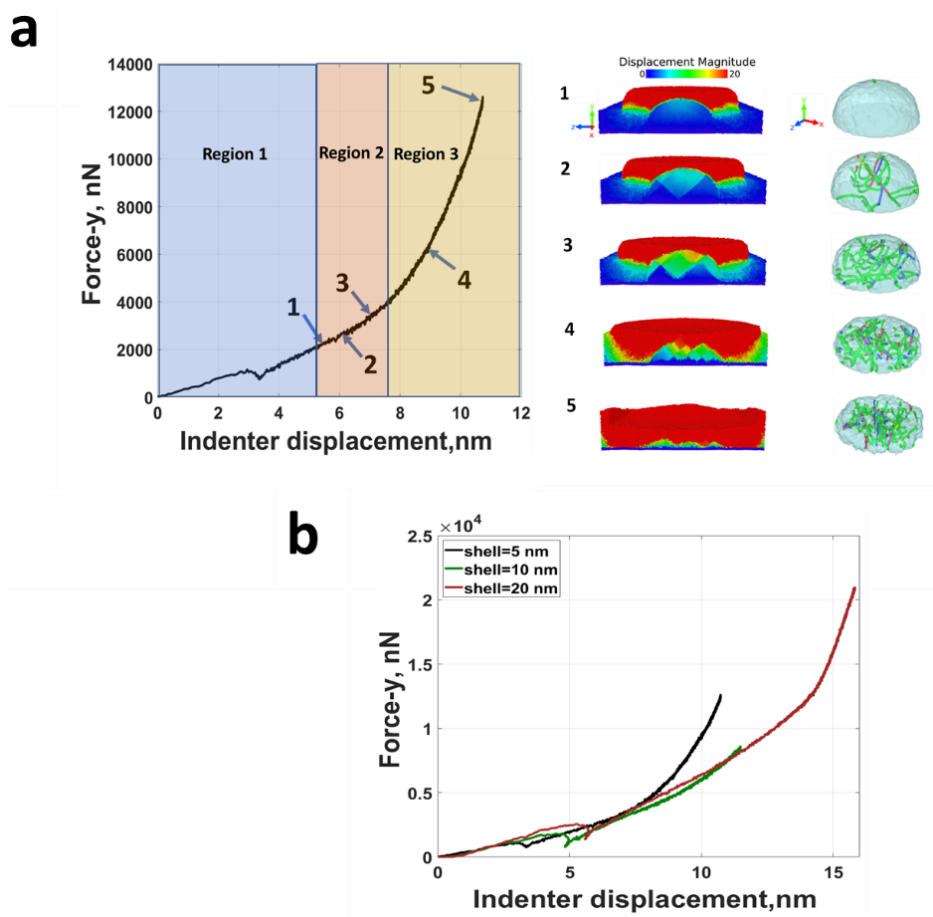

Fig 2. (a) Force versus indenter displacement (*ID*) for indentation on a CSN with core radius 10 nm and shell thickness 5 nm. Points 1-5 in the plot are marked to show the corresponding deformation of the core-shell model. The increase in the force after dislocation nucleation is due to strain hardening. (b) Force versus indenter displacement for indentation on a CSN with core radius 10 nm and shell thickness of 5, 10, and 20 nm.

The force-displacement plots for a CSN with 10 nm core radius and shell thickness of 5,10, and 20 nm are shown in Fig. 2(b). We observe no difference in the elastic stiffness for the CSN with varying shell thickness, but we observe a rightward shift in the regions 1,2, and 3. The shift occurs because with increasing shell thickness in the CSN, we need to indent to greater depths to nucleate dislocations. From the displacement magnitude images shown in Fig. 2, we observe that the shell deforms initially as it first encounters the indenter, and then later core deformation is observed. Therefore, with the increase in the shell thickness, we need to deform the shell more to generate enough stresses within the core to nucleate dislocations. We observe similar force-displacement behavior for R=30 nm core.

The stress corresponding to first dislocation nucleation event in the core is recorded for both core and shell separately (see Fig. 3) for all six samples. From Fig. 3(a) we observe that with an increase in the shell thickness, the stress associated with dislocation nucleation in the core decreases. A more significant decrease in stress in the core is observed in the smaller core radius (10 nm) compared to the larger core radius (30 nm). Similar observations were found by Fleming et al. [15]. For the higher core radius (R=30 nm) CSN, as the shell thickness increases, the stress in the shell increases coressponding to stress needed to nucleate first dislocation in the core. This is also observed in core-shell nanorods [16] composed of Al and a-Si. For the CSN samples with 10 nm core radii, there is no trend observed in stress in the shell corresponding to dislocation nucleation in the core. That is, stress in shell increased for t=10 nm compared to t=5 nm, and then decreased for t=20 nm compared to t=10 nm (see Fig. 3(a)). When stress in the shell corresponding to dislocation nucleation is represented by the ratio of core radius to shell thickness (see Fig. 3 (b)) we see that an increase in the core/shell ratio increases stress in the shell at the point of dislocation nucleation in the core and stablizes. Except one data point, R=10 nm and t=20 nm CSN, the

opposite trend is observed in the core for all other samples, i.e., as the core/shell ratio increases the stress in the core initially decreases and later stabilizes. This implies that larger core radii do not influence the initial plastic deformation of the CSN. Similar comparative results are observed experimentally by Fleming et al. [15], although experimental [15] core radii are an order of magnitude larger than the samples considered here, the R/t ratios in experiments range between 0.3-3. From Fig. 3(a and b) we can conclude that shell thickness should be chosen so that the ratio of the core radius to shell thickness should be greater than 0.5 and less than 2 ($0.5 < R/t < 2$) in order to have a strong CSN.

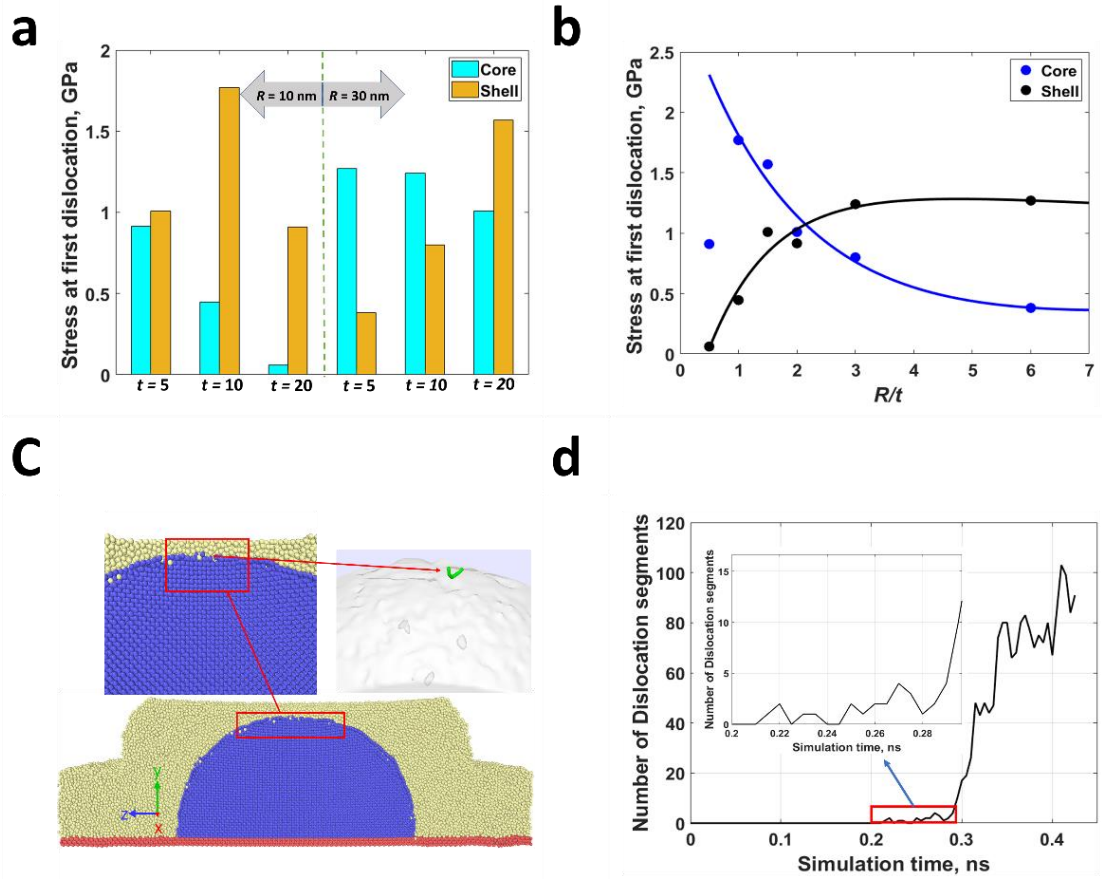

Fig 3. (a) Stress at the point of dislocation nucleation in the core and shell for different core-shell nanostructure models (C represents core radius; S represents Shell thickness). (b) Stress at the point of dislocation nucleation versus ratio of core radius (R) to shell thickness (t). (c) Cross sectional view of CSN showing the dislocation nucleation event. Point defects present at the interface of core and shell is also displayed. (d) Dislocation density evolution during the indentation process for CSN (R=10, t=10 nm).

To understand the deformation behavior of CSNs, we analyze different dislocation nucleation sources in the core. The point defects are substitutional atoms and point vacancies are formed by diffusion between the crystalline core and amorphous shell. We observe that the first dislocation nucleation event in the core for the CSN occurs at or near point defects present at the crystalline-amorphous interface (see Fig. 3(c)). However, all such events at the interface do not lead to dislocation propagation. A few dislocations move back to the interface (see Fig. 3(d), insert, less than 0.28 ns). Other dislocations, after the dislocation nucleation event, propagate into the crystal and absorb into the interface before further increase in dislocation content (see Fig. 3(d) after 0.29 ns and supplementary section S3). This phenomenon is called dislocation starvation, which was also observed in several other studies [9, 15, 22, 23]. The driving force to escape the dislocation to the free surface is the image force from the surface, which increases with decreasing sample size [24]. After the initial dislocation nucleation, further deformation of the CSN leads to an increase in dislocation density. A decrease in core size also increases the critical stress needed for dislocation multiplication. Dislocations escape from the crystal before multiplying or interacting with each other dislocations resulting in dislocation starved state which further require a very high stress to nucleate new dislocations (see Fig. 3(d)). Therefore, smaller crystals are stronger than larger crystals and much stronger than bulk materials.

Fig 4 shows the force-displacement relation during retraction. Specifically, the black curve corresponds to the indentation process, while the other colored curves correspond to the same relation while unloading or retracting the indenter at different nanoindentation depths. We observe that as the depth of the retraction increases, the adhesion force between indenter and the CSN also increases. This is because more atoms in the indenter are in contact with the CSN with increasing indentation depth.

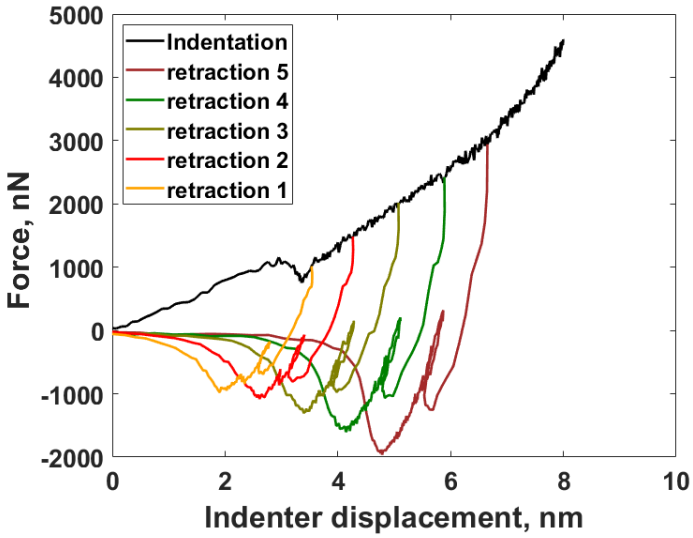

Fig 4. Force versus indenter displacement of CSN (*R*=10 nm and *t*=5 nm) during indentation and retraction processes.

To study the plastically deformed microstructures of CSNs, we use DXA in OVITO (see Fig. 5). The dislocations are represented by thin lines. The lines with green color correspond to Shockley partial with 1/6 <112> Burgers vector, blue color characterize the perfect dislocation with Burgers vector ½ <110>, yellow color represents Hirth dislocation with 1/3< 001> Burgers vector, and pink color represents stair-rod dislocation with 1/6 <110> Burgers vector. We do observe shear loops (in the core of CSN) that are formed during the deformation of the CSN (see supplementary section, S1 (a)). Further, upon indenting the CSN some of the dislocations move to the interface of CSN.

Dislocation nucleation and propagation in the core for all the CSNs are recorded throughout the nanoindentation and retraction process. We observe that CSNs deform twice compared to a flat surface with same amorphous and metallic thickness to observe stable dislocations that would propagate into the core (see supplementary section, S2). This is because CSNs exhibit a dislocation starvation mechanism (see Fig. 3(d) and supplement section, S2 and S3) whereas the flat surface sample does not exhibit a dislocation starvation mechanism (see the continuous increase in

dislocation density for the flat model in supplement, S2(d)). The dislocation density (DD) for all CSNs are calculated approximately 10% after the nanoindentation depth associated with the first dislocation nucleation event, as shown in Fig. 5(a). We see that with an increase in the shell thickness, the dislocation density in the core decreases (see Fig. 5(a)). This decrease in DD is significant in a 10 nm core radius compared to 30 nm core radius. This is because samples with smaller core radii experience larger back stress in the core during nanoindentation. Similar results are observed by Fleming et al. [13, 15].

We record the dislocation density for all retraction processes, as shown in Fig. 5(b). The recovery of DD is calculated based on indentation depth. An indentation depth (*ID*) that is more than the shell thickness does not indicate that shell has completely deformed because the core also experiences deformation with nanoindentation. The *ID* values (cyan bar plot) in Fig. 5(b) correspond to 100% recovery of the dislocation content in CSNs. This is observed for samples with core radii of R=10 nm and 30 nm. For the CSNs that are deformed more than the corresponding *ID* values (Fig. 5b, cyan bar plots), we do not observe 100% recovery (orange bar plot). The percentage recovery can be varied based on how much farther we indent the CSNs beyond the corresponding *ID* values (cyan bar plots). Therefore, we chose random points from force-displacement plots that are beyond the 100% recovery point for retraction studies and measured the average recovery percentages of the CSNs (see orange bar plot in Fig 5(b)). Several other authors have also observed a 100% recovery of the plastic deformation [3, 13, 16, 25, 26]. Since the substrate is fixed for CSNs, we observe that substrate effect is predominant for 10 nm core radius compared to 30 nm core radius samples. We also notice that the cores of the CSN have retained its size and shape after the retraction of the indenter. Further analysis of CSNs (see Fig. 5(b)) suggests that CSNs does not undergo plastic deformation if the *ID* is less than or equal to the shell

thickness except for R=10 nm and t = 20 nm CSN. This indicates that for CSN, R=10 nm and t = 20 nm sample the dislocation nucleation stress has reached earlier compared to other samples. The optimal shell thickness for a given core radius that would protect the core-shell structures from plastic deformation ($0.5 < R/t < 2$, see Fig. 4 (b)) reported in this study matches the ratio (R/t) studied by Fleming et al. [15]. The un-recovered dislocations present in the core after retraction are mostly sessile dislocations, which are formed by dislocation interactions from different planes. The sessile dislocations are immobile, and they are difficult to eliminate without changes in the stress state within the CSN. Further analysis suggests that, larger the core radius (here, R=30 nm, see Fig. 5 (b)) it is less likely to have 100% recovery of dislocations at the end of the retraction process.

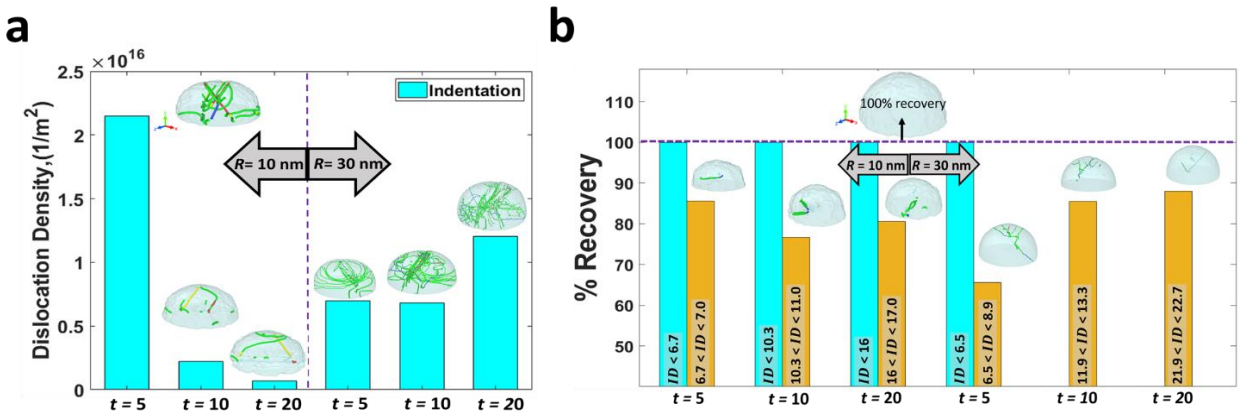

Fig 5. (a) Dislocation density in core-shell samples at a depth that is approximately 10% more than the first dislocation nucleation depth. (b) The percentage recovery of the dislocations during the retraction process for different core-shell samples. All values related to *ID*, *R* and *t* are in nm.

3.4 Conclusions

In this study, we investigate the mechanical response and changes in dislocation density during nanoindentation and retraction on CSNs by performing large scale molecular dynamics simulations. We observe no difference in stiffness for the CSN with varying shell thickness, but we observe a shift of regions 1, 2 and 3 towards larger intentation depths, associated with different

regions of plastic deformation. We also show that nanoindentation performed in CSNs involves concepts of dislocation nucleation and dislocation starvation. Larger core radii do not have a significant influence on the initial plastic deformation of the CSN. The shell thickness should be chosen so that the ratio of core radius to shell thickness is less than two in order to have deformation resistant CSN. Further, we observe that with increases in core radius or shell thickness, the CSN's ability to recover 100% of plastic deformation decreases. Our results provide valuable information about the optimal core radius to shell thickness ratio as well as the recovery of CSN that will help researchers fabricate CSNs for NEMS and MEMS applications.

Acknowledgments

We acknowledge the support from National Science Foundation under the Grant CMMI #1463306. Authors would like to acknowledge the support in part by the National Science Foundation under the grants ARI #0963249, MRI #0959124, and EPS #0918970, and a grant from Arkansas Science and Technology Authority, managed by Arkansas High-Performance Computing Center.

Conflicts of interest: The authors declare no conflict of interest.

References

1. K. Komvopoulos: Adhesion and friction forces in microelectromechanical systems: mechanisms, measurement, surface modification techniques, and adhesion theory *Journal of adhesion science and technology.* **17**(4), 477 (2003).

2. S.H. Kim, D.B. Asay and M.T. Dugger: Nanotribology and MEMS *Nano today.* **2**(5), 22 (2007).

3. J.G. Steck, R.A. Fleming, J.A. Goss and M. Zou: Deformation and fatigue resistance of Al/a-Si core-shell nanostructures subjected to cyclic nanoindentation *Applied Surface Science.* **433**, 617 (2018).

4. W.M. Van Spengen: MEMS reliability from a failure mechanisms perspective *Microelectronics Reliability.* **43**(7), 1049 (2003).

5. R.R. Santhapuram and A.K. Nair: Frictional properties of multi-asperity surfaces at the nanoscale *Computational Materials Science.* **136**, 253 (2017).

6. M.D. Uchic, D.M. Dimiduk, J.N. Florando and W.D. Nix: Sample dimensions influence strength and crystal plasticity *Science.* **305**(5686), 986 (2004).

7. M.D. Uchic, P.A. Shade and D.M. Dimiduk: Plasticity of micrometer-scale single crystals in compression *Annual Review of Materials Research.* **39**, 361 (2009).

8. K. Sieradzki, A. Rinaldi, C. Friesen and P. Peralta: Length scales in crystal plasticity *Acta materialia.* **54**(17), 4533 (2006).

9. A. Rinaldi, S. Licoccia and E. Traversa: Nanomechanics for MEMS: A structural design perspective *Nanoscale.* **3**(3), 811 (2011).

10. A. Rinaldi, M. Correa-Duarte, V. Salgueirino-Maceira, S. Licoccia, E. Traversa, A. Dávila-Ibáñez, P. Peralta and K. Sieradzki: Elastic properties of hard cobalt boride composite nanoparticles *Acta Materialia.* **58**(19), 6474 (2010).

11. A. Rinaldi, S. Licoccia, E. Traversa, K. Sieradzki, P. Peralta, A.B. Dávila-Ibáñez, M.A. Correa-Duarte and V. Salgueirino: Radial inner morphology effects on the mechanical properties of amorphous composite cobalt boride nanoparticles *The Journal of Physical Chemistry C.* **114**(32), 13451 (2010).

12. S. Plimpton: Fast parallel algorithms for short-range molecular dynamics *Journal of computational physics.* **117**(1), 1 (1995).

13. R.A. Fleming, J.A. Goss and M. Zou: Material dimensionality effects on the nanoindentation behavior of Al/a-Si core-shell nanostructures *Applied Surface Science.* **412**, 96 (2017).

14. B. Jelinek, S. Groh, M.F. Horstemeyer, J. Houze, S.G. Kim, G.J. Wagner, A. Moitra and M.I. Baskes: Modified embedded atom method potential for Al, Si, Mg, Cu, and Fe alloys *Physical Review B.* **85**(24), 245102 (2012).

15. R.A. Fleming and M. Zou: The effects of confined core volume on the mechanical behavior of Al/a-Si core-shell nanostructures *Acta Materialia.* **128**, 149 (2017).

16. S.E. Muller and A.K. Nair: Deformation mechanisms of Al/amorphous-Si core–shell nanorods *Modelling and Simulation in Materials Science and Engineering.* **27**(4), 045006 (2019).

17. S. Yan: Multiscale study of the properties of hybrid laser-welded Al-Mg-Si alloy joints, (2019).

18. Y. Qiu, Y. Kong, S. Xiao and Y. Du: Mechanical properties of β ″precipitates containing Al and/or Cu in age hardening Al alloys *Journal of Materials Research.* **31**(5), 580 (2016).

19. S. Xiao, Y. Kong, Y. Qiu and Y. Du: The microstructure evolution of U1 and U2 nanowires constrained in Al matrix *Computational Materials Science.* **117**, 180 (2016).

20. A. Stukowski: Visualization and analysis of atomistic simulation data with OVITO–the Open Visualization Tool *Modelling and Simulation in Materials Science and Engineering.* **18**(1), 015012 (2009).

21. A.P. Thompson, S.J. Plimpton and W. Mattson: General formulation of pressure and stress tensor for arbitrary many-body interaction potentials under periodic boundary conditions *The Journal of chemical physics.* **131**(15), 154107 (2009).

22. J.R. Greer and W.D. Nix: Nanoscale gold pillars strengthened through dislocation starvation *Physical Review B.* **73**(24), 245410 (2006).

23. C. Chisholm, H. Bei, M. Lowry, J. Oh, S.S. Asif, O. Warren, Z. Shan, E.P. George and A.M. Minor: Dislocation starvation and exhaustion hardening in Mo alloy nanofibers *Acta Materialia.* **60**(5), 2258 (2012).

24. P. Huang and Q. Yu: Dislocation Multiplications in Extremely Small Hexagonal-structured Titanium Nanopillars Without Dislocation Starvation *Scientific reports.* **7**(1), 15890 (2017).

25. B.D. Morton, H. Wang, R.A. Fleming and M. Zou: Nanoscale surface engineering with deformation-resistant core–shell nanostructures *Tribology Letters.* **42**(1), 51 (2011).

26. W. Tidwell, D. Scott, H. Wang, R. Fleming and M. Zou: Nanoindentation study of deformation-resistant Al/a-Si core–shell nanostructures *Acta Materialia.* **59**(15), 6110 (2011).

Chapter 4

4. Role of grain boundaries in plastic deformation of core-shell nanostructures

Raghuram Reddy Santhapuram, Douglas E. Spearot, Arun K Nair

Abstract

The mechanical properties of metallic systems at the nanoscale can be modified by varying their structure and composition. One example of a deformation-resistant structure is a core-shell nanostructure (CSN). In the present work, we use molecular dynamics simulations to perform nanoindentation and retractions to understand plastic deformation of core-shell nanostructures. The core consists of aluminum (Al), the shell is amorphous-silicon (a-Si), and the substrate is either crystalline Al or a-Si. The unique aspect of this work is that we study the deformation behavior of CSNs that contain symmetric and asymmetric grain boundaries in the core with two different orientations; comparisons are made to deformation in a CSN with a single crystal core. Nanoindentation on CSNs with 5 nm and 10 nm core radius shows that the elastic stiffness with and without a grain boundary are similar when the substrate material is the same. 5 nm core radius CSNs with a-Si and Al-substrates and an asymmetric tilt grain boundary in the core show 100% recovery from dislocation plasticity, but damage within the core leads to reduction of ~50% of the atoms that no longer being identified as FCC crystal structure, which makes these CSNs non-deformation resistant. CSNs with Al substrate (5 nm and 10 nm core radius) obtained 100% recovery from plasticity and retained its crystal structure after unloading when the core is single crystal or contains a symmetric tilt grain boundary. Moreover, a single crystal core can withstand nanoindentation to 100% of the shell thickness whereas, a symmetric tilt grain boundary core can only withstand nanoindentation about 80% of the shell thickness and still have 100% recovery from plasticity. Therefore, CSNs with single crystal core are more reliable for deformation-resistant behavior than those that contain grain boundaries.

keywords: Core-shell nanostructures, Symmetric tilt grain boundary, Asymmetric tilt grain boundary, Single crystal, Deformation resistant

4.1 Introduction

The development of material architecture through nanoengineering is a renovative approach to manipulate the defect landscape of metallic systems to improve their mechanical properties [1, 2]. Nanotexturing is one of the novel materials architectures that has been used to improve surface properties. These nanotextures can be produced using different approaches such as plasma-enhanced chemical vapor deposition, thermal evaporation, and lithography [3-5]. Each of these methods has its own advantages and disadvantages and are best suited for specific applications.

Nanotextured surfaces have shown improved tribological properties at the micro- and nanoscale in polymers [6, 7], metals [8, 9], and other materials [10, 11]. These nanotextured surfaces have potential applications in electronics [12-14], magnetic storage [15], micro-electromechanical systems [3, 16], and nano-electromechanical systems [3]. Unfortunately, nanotextured surfaces lack structural integrity when subjected to loading, resulting in permanent deformation of the texture, which leads to device reliability issue. Researchers have identified core-shell nanostructures as a potential solution to this issue. The core-shell nanostructures are deformation-resistant to compression loading and have been identified in several different core and shell materials [4, 17, 18]. Further, these nanostructures have shown enhanced fracture resistance [1], fatigue resistance [5], and can also have complete shape restoration after the load is removed.

The mechanical properties of materials are associated closely with internal structural defects. Among those defects, dislocations are the primary carriers of plastic deformation in metallic materials. During indentation, dislocations nucleate from the core-shell interface and

escape to the opposite side of the core, because of the small core volume, before they have the opportunity to multiply and interact. This leads to a dislocation starvation state [2, 18, 19]. Therefore, the plasticity of the core-shell nanostructure is accommodated by the nucleation and motion of new dislocations rather than by motion and interaction of existing dislocations, as in the case for bulk crystals [2, 19]. The nucleation of new dislocations requires higher stress; hence it is referred to as dislocation starvation hardening. Furthermore, core-shell nanostructures exhibit reverse plasticity because of the back stress generated in the core [18]. This causes dislocations that are within the core when the load is removed to retrace their paths or annihilate during unloading. The phenomenon of dislocation starvation and reverse plasticity in CSNs makes them deformation resistant. Researchers have performed studies on core-shell nanostructures for different geometries [17], sizes [4], and to study the effect of core radius and shell thickness [19]. Nevertheless, the size-dependent response of single crystal and polycrystalline cores and the effect of different substrates are currently unknown.

Therefore, in this work, we study differences in the deformation behavior of single crystal and polycrystalline cores in core-shell nanostructures. We also study the effect of substrate material on the deformation behavior of core-shell nanostructures. The core material is aluminum (Al), the shell is amorphous silicon (a-Si), and the substrate is either Al or a-Si. We use molecular dynamics simulations to predict the mechanical properties of CSNs under nanoindentation and retraction. Additionally, we explore and quantify dislocation nucleation, propagation, and recovery of the core-shell nanostructures.

4.2 Methods

4.2.1 Core-shell model description

Schematics of the core-shell nanostructures are shown in Figs. 1 (a, b). The core consists of Al (see Figs. 1 (c, d, e, f, g)), the shell is a-Si, and the substrate is made of either Al or a-Si (see Figs. 1(a, b)). The lattice of the crystalline Al core and substrate are oriented along *x* [1 0 0], *y* [0 1 0], and *z* [0 0 1] directions, respectively. We use a 100 nm radius rigid spherical indenter composed of Al atoms. Core-shell models are generated using the Large Scale Atomic/Molecular Massively Parallel Simulator (LAMMPS) [20] except the core with a grain boundary. The core with the grain boundary is modeled using Atomsk [21] and later stitched with shell and substrate materials using LAMMPS [20].

Table 1: Types of core and substrate used in core-shell models. Two different types of cores are used in this study: grain boundary and single crystal (SC). The grain boundary core is further categorized into two types: symmetric tilt grain boundary (STGB) and asymmetric tilt grain boundary (ATGB). *R* is the core radius, and *t* is shell thickness.

Models			**Grain Boundaries**								**SC**	
			STGB				ATGB					
R, nm	***t, nm***	***Substrate height, nm***	Parallel to [0 1 0] axis (Pa)		Inclined to [0 1 0] axis (Ia)		Parallel to [0 1 0] axis (Pa)		Inclined to [0 1 0] axis (Ia)		Substrate	
			Substrate (S)		***Substrate (S)***		***Substrate (S)***		***Substrate (S)***		***Substrate (S)***	
5	5	5	a-Si	Al	a-Si	Al	a-Si	Al	a-Si	Al	a-Si	Al
10	10	5	Al								Al	

Table 1 lists details of the core-shell models studied in this research. We consider two types of grain boundaries in this study: a symmetric tilt grain boundary (STGB, see Figs. 1(c, d)), and an asymmetric tilt grain boundary (ATGB, see Figs. 1(e, f)). The STGB has a misorientation angle $\theta = 26.6^{o}$ about the [0 1 0] tilt axis. Whereas the ATGB has a random misorientation angle chosen by Atomsk [21] about the [0 1 0] tilt axis. The random misorientation angle of the ATGB later calculated is $\theta = 45.3^{o}$, which is expected to represent a high angle grain boundary. Specifically, the grain on the right in Fig. 1(e) is rotated by $\theta = 30.8^{o}$ about [0 1 0] while the grain on the left in

Fig. 1(e) is rotated in the opposite direction by θ = 14.5^{o} about [0 1 0] tilt axis. The core with a grain boundary has two different alignments: one where the grain boundary is aligned parallel to the [0 1 0] axis, and the other where the grain boundary is inclined 38° to [0 1 0] axis. The volume of the two grains is the same when the grain boundary alignment is parallel to [0 1 0] axis, but the volume of the two grains is not the same when the grain boundary is inclined, i.e., one grain occupies about 35 – 40% of the core volume and the rest is occupied by other grain. The core radius to shell thickness ratio is chosen from the optimal range described in Santhapuram et al. [19]. After creating the core-shell models, Al atoms are deleted at the grain boundary (in the core) and at the core-substrate interface when the distance between atoms is less than 2 Å to avoid non-physical high energy configurations. Similarly, interface atoms between the Al core and a-Si shell/substrate are deleted when the separation distance is less than 2.57 Å [22]. The a-Si shell is generated by randomly distributing Si atoms in the shell and substrate regions, similar to the procedure described in Santhapuram et al. [19].

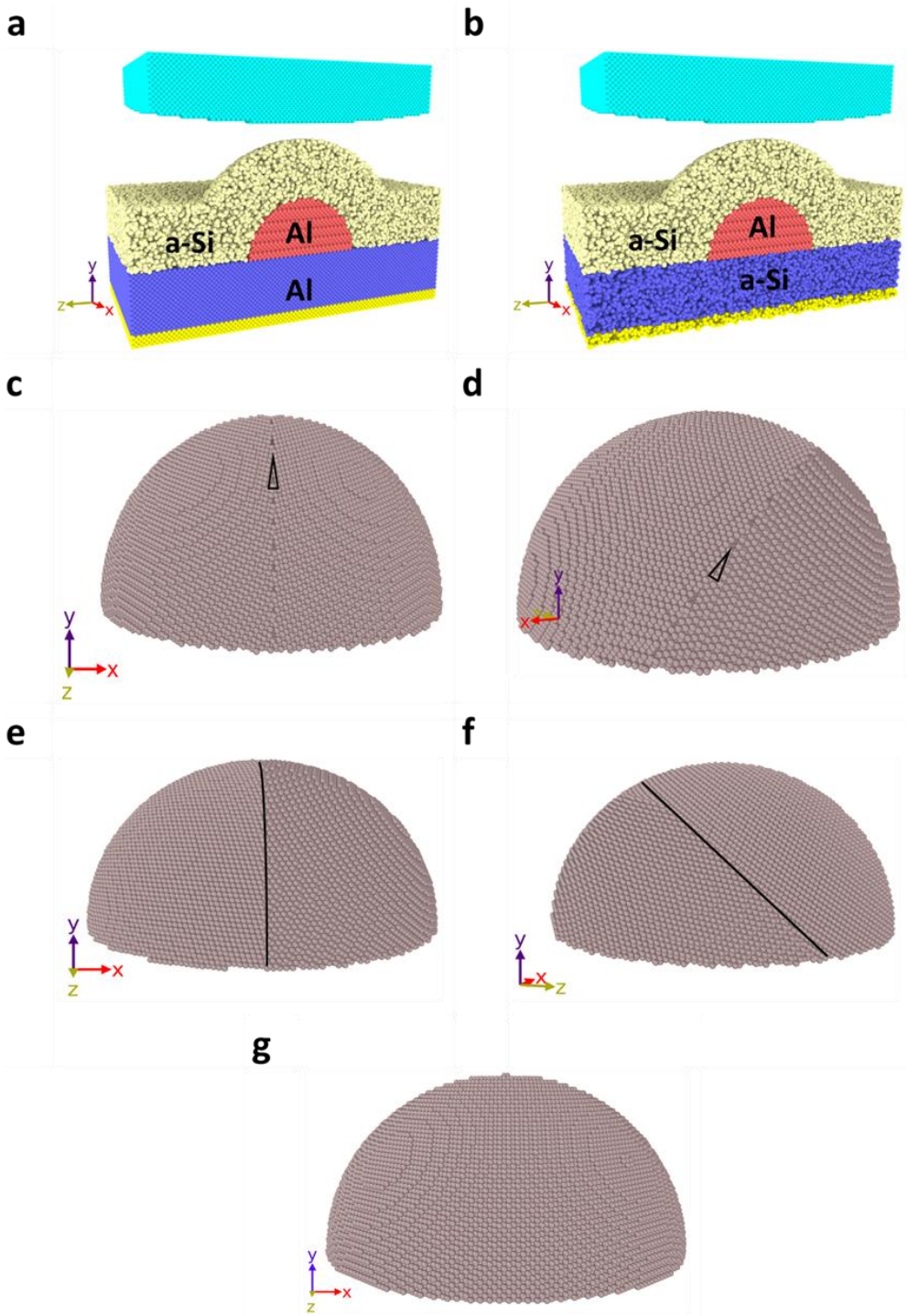

Fig 1. A cross-sectional view of the core-shell nanostructure, where the core is made of Al, the shell is made of a-Si, and the substrate is either made of (a) Al or (b) a-Si. Two different types of cores are used in the core-shell nanostructure (c-f) core with the grain boundary, and (g) core with a single crystal. Additionally, two different types of grain boundaries are used in this study (c, d) symmetric tilt grain boundary (STGB), and (e, f) asymmetric tilt grain boundary (ATGB). Further, two different grain boundary alignments are used (c, e) parallel to [0 1 0] axis and (d, f) inclined to [0 1 0] axis.

4.2.2 Simulation specifics

The MD simulations are performed using the Large-Scale Atomic/Molecular Massively Parallel Simulator (LAMMPS) [20]. We use a modified embedded atom method (MEAM) potential [23] to define the interactions between Al-Al, Si-Si, and Al-Si atoms. Periodic boundary conditions are imposed along the *x* and *z*-directions, and a non-periodic boundary condition is used along the *y*-direction. The core-shell nanostructures are relaxed using energy minimization with a conjugate gradient method followed by temperature and pressure equilibration for 300 ps using equations of motion for the isothermal-isobaric ensemble (NPT). The temperature is maintained at 300 K while enforcing zero pressure in the periodic directions. Several atomic layers (1 nm thickness) of the substrate are fixed during simulations, as shown with the pink color atoms in Figs. 1 (a, b). The simulations consist of two steps. First, we indent the CSNs, and second the indenter is retracted. During indentation, the indenter is applied 10 nN (negative) force for every 0.5 ps, which displaces indenter atoms and deforms the core-shell nanostructure. This method is called the force-based method [19]. Once the required indentation depth is reached, the indenter is retracted by adding 10 nN positive force every 0.5 ps. Throughout the indentation and retraction process, the position of the indenter and the force experienced by the indenter is recorded. We use OVITO [24] to visualize and track dislocation emission, propagation, and annihilation in the core-shell models through the entire simulation.

4.3 Results and discussion

4.3.1 Nanoindentation and retraction response of the core-shell nanostructures

Fig. 2 displays force-indentation curves for the CSNs with 5 nm core radius, 5 nm shell thickness, and 5 nm substrate thickness. Figs. 2 (a, b) correspond to core-shell nanostructures with Al substrate and a-Si substrate, respectively. The drop in the force around 3.7 nm to 5 nm is due

to buildup in back-stress in the core during indentation, this is observed for all models. Similar observations are noted in simulations [19] and experiments [4]. Force- indentation curve (see Fig. 2(a)) shows a linear elastic region (< 4 nm indentation depth), a plastic region with a low hardening rate (4-6 nm indentation depth), and a plastic region with high hardening rate (> 6 nm indentation depth). This is consistent with our previous simulations on CSNs [19].

The different types of cores used in CSNs provide no significant difference in force-displacement behavior (see Figs. 2 (a, b)) when the substrate material is the same. This indicates that the inclusion of a single grain boundary in the core has no significant impact on nanoindentation behavior of the CSNs that have similar substrate material. Similarly, the stiffness (slope of force-indenter displacement plot) is the same for CSNs with Al and a-Si substrate in the linear elastic region (see Figs. 2(c, d)). However, the force-displacement curves deviate from each other during plastic hardening when the substrate materials are different (see Figs. 2 (c, d)). The average hardening rate of CSNs with a-Si substrate is higher than CSNs with Al-substrate over the plastic region. The increase in stiffness in the plastic region is because dislocations are confined in the core (higher dislocation-dislocation interactions) of CSNs with a-Si substrate, whereas for CSNs with Al substrate, dislocations can propagate out of the core into the substrate (lower dislocation-dislocation interaction). In addition to stiffness difference, the drop in the force appears slightly later for the a-Si substrate than the Al substrate for all the CSNs. This is because of free volume that is present in a random distribution of a-Si atoms in the substrate (see Fig 2 (e, f), the shell, indenter atoms are removed, and the substrate is sliced to 1 nm for clear visibility of voids). The Al atoms in the core are forced into the substrate free volume during initial deformation, which causes the delay in force drop in the CSN with a-Si substrate (see Fig 2(f)).

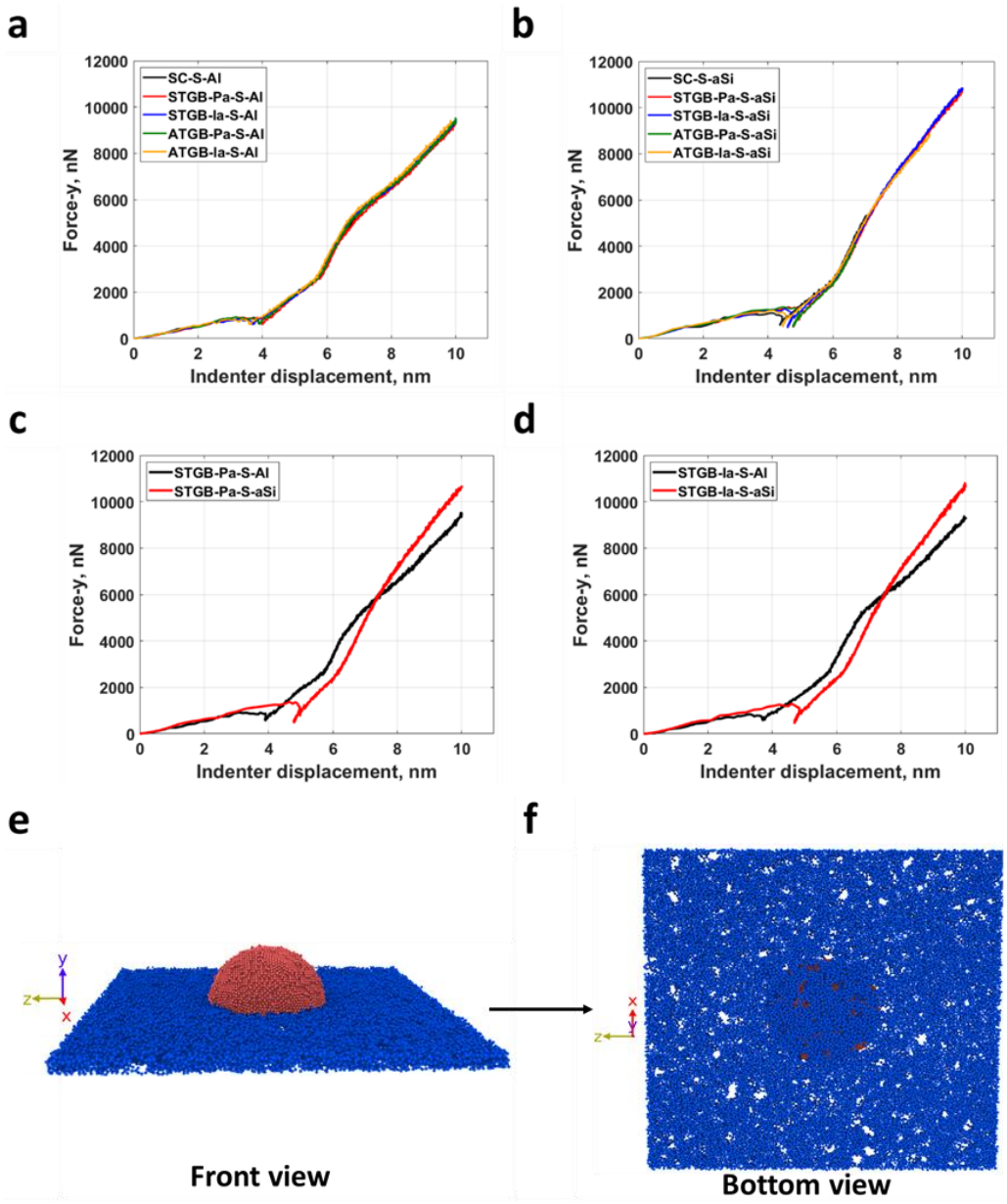

Fig 2. Force versus indenter displacement in CSNs with (a) Al substrate, (b) a-Si substrate. (c, d) Force versus indenter displacement comparison for CSNs with symmetric tilt grain boundary for Al and a-Si substrate, (c) grain boundary parallel to [0 1 0] axis, (d) grain boundary inclined to [0 1 0] axis. (e, f) CSN with shell and indenter atoms removed, and the substrate is sliced to 1 nm thick for clear visibility of voids. (e) Front view of the CSN, (f) Bottom view of the CSN.

The force-displacement behavior during retraction of the nano indenter from the CSN with a STGB and Al substrate is shown in Fig. 3. The black curve represents the force-displacement behavior of the CSN during the indentation phase, whereas other colors represent the force

behavior during the retraction phase at different indentation depths. The retraction points were specifically chosen when plastic deformation (dislocations) is observed in the CSN.

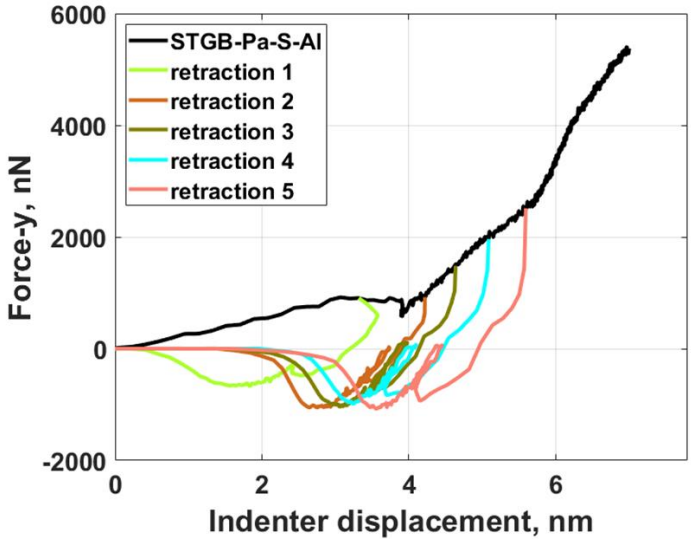

Fig 3. Force vs indenter displacement (*ID*) behavior of CSN's (R = t = h= 5 nm) during nanoindentation and retraction processes.

4.3.2 Shape recovery of the CSNs

Table 2: Shape recovery of CSN's where core is made of single crystal for both Al and a-Si substrates.

Models	Before Indentation, nm	After Retraction, nm				
		Retraction 1	Retraction 2	Retraction 3	Retraction 4	Retraction 5
SC-S-Al	4.87	4.82	4.79	4.73	4.86	4.83
SC-S-aSi	4.82	4.73	4.68	4.25	3.91	4.13

The radius of the core is measured before nanoindentation and after the retraction for all models. Results of CSNs with a single crystal core of 5 nm radius for both Al and a-Si substrates are shown in Table 2, but all models show a similar trend. We measure that the core of the CSNs with Al substrate has recovered its shape for all the retraction points chosen, even for those whose indentation depth is greater than the shell thickness (for example, see Fig. 3 retraction points 4 and 5). However, when an a-Si substrate is used, the core of the CSNs does not recover its shape, and

the recovery percentage generally decreases with an increase in the indentation depth. Therefore, from these observations, CSNs with Al substrate can be used for reindentation, whereas CSNs with a-Si substrate cannot be used for reindentation.

4.3.3 Dislocation dynamics during nanoindentation and retraction of CSNs

We use OVTIO [24] to visualize plasticity in the Al core and substrate using the dislocation extraction algorithm (DXA). The initial equilibrated CSN with a grain boundary has dislocations in the grain boundary region due to lattice mismatch (see initial points in Fig. 4(a) and insert). Further, we use the volume of the crystalline regions (Al) to calculate dislocation density, because dislocations are defects that are exclusively present in the crystalline material, but not in amorphous materials. For CSNs with Al substrate, core and unfixed substrate volumes are combined to calculate dislocation density. For CSNs with a-Si substrate, just core volume is used to calculate dislocation density. Several dislocation types are identified by DXA during deformation, such as Shockley partials, Hirth, perfect, stair-rod, and other dislocations. Dislocation activity, nucleation, and propagation are recorded during nanoindentation for all CSNs with a 5 nm core radius and are shown in Figs. 4 (a, b).

We analyze the dislocation nucleation sources in the core. For CSNs with single crystal core (Al), the source for dislocations is the interface between the crystalline core and amorphous shell. This is similar to our previous study on CSNs [19]. For CSN with a grain boundary within the core, the source is identified as either the grain boundary in the core or at the core-shell and core-substrate interfaces. However, not all the dislocation events recorded lead to propagation. A few dislocations are forced back to the interface or the grain boundary, and some are absorbed on the other side of the interface or at the grain boundary. This elimination of dislocations during the deformation process is known as a dislocation starved state. To completely nucleate a new

dislocation, a higher force is required. This phenomenon is known as dislocation starvation hardening and is observed in both experiments [18, 25] and simulations [19, 26]. However, we do not find much difference in the dislocation density for CSNs with an Al substrate with and without grain boundaries (see Fig. 4(a)). Fig 4(b) shows the dislocation density in CSNs with an a-Si substrate, where the core is made of single crystal or has a grain boundary. The dislocations are confined within the core as the shell and substrate have an amorphous structure, and hence the dislocation density is also lower for CSN with a-Si substrate compared to CSN with Al-substrate (see Fig. 4 (a, b)). The single crystal core has no dislocations at the beginning of the nanoindentation, but dislocations are observed at an indentation depth of 4.2 nm (see Fig. 4 (b)). Later there is a fluctuation of dislocation density due to dislocation starvation. For the grain boundary core in the CSN with the a-Si substrate, we observe that the dislocation starved state is higher than the single crystal core of CSNs (see Fig. 4 (b)).

Although Table 2 shows strong evidence of deformation resistance, to further identify CSNs as deformation-resistant nanostructures, we evaluate the dislocation density after the retraction process. We choose five points from the force-displacement plots of CSNs, beyond the point of initiation of plastic deformation during nanoindentation. The load is removed, as described in Section 2.2, and the average recovery percentage of the CSNs is measured. The recorded dislocation density after the retraction process for CSNs with and without a grain boundary is shown in Fig. 4(c). From Fig. 4(c) we observe 100% recovery for all the CSNs with a-Si substrate. Whereas only one CSNs with an Al substrate (ATGB, with inclined aligned grain boundary) has 100% recovery. The next best recovery percentage for CSNs with Al substrate is the STGB aligned parallel to [0 1 0], followed by single-crystal Al core at 96 and 88 % recovery, respectively.

We further evaluated residual damage within the core of the CSNs after retraction to verify if the core has retained its crystal structure to be used for reindentation. The damage in the core is inspected using common neighbor analysis (CNA) and coordination analysis (radial distribution function) in OVITO [24]. From the CNA analysis, we observe that no core in the CSNs has 100% retained its crystal structure (FCC) after unloading (see Fig. 4(d)). The Al-substrate CSNs with STGB parallel aligned core and single-crystal core has retained more than 95% of its crystal structure (FCC) in the core (see Fig. 4(d)). The decline of 5% in the number of FCC atoms might be due to small changes in the core surface geometry during the indentation/retraction process due to dislocation motion. The CSNs with a-Si substrate have retained less than 50% of their crystal structure after unloading (see Fig. 4(d)). Further, coordination analysis performed on the core of CSNs with Al and a-Si substrate agrees with the retained crystallinity obtained from CNA (see Figs. 4(e, f)). The coordination analysis performed on the core (STGB parallel aligned) of CSN (with Al-substrate) before indentation and after retraction (for lowest and highest retraction points) follows a similar trend, which confirms no residual damage (see Fig. 4(e)). Whereas coordination analysis performed on the same CSN with a-Si substrate shows residual damage after retraction, implied by the reduction in peak intensities and broadening of the peak profiles (see Fig. 4(f)). Therefore, comparing the percentage recovery (see Fig. 4(c)), percentage retained of FCC atoms (see Figs. 4(d-f)), and coordination analysis (see Figs. 4(e, f)) of the CSN, we can conclude that not all CSN are reliable to undergo a reindentation process, particularly the CSNs with a-Si substrate. This is because CSNs with a-Si substrate has the lowest crystallinity left after unloading, which makes the CSNs non-deformation resistant and unreliable for further loading conditions. Therefore, from Figs. 4(c, d), we can conclude that CSNs with STGB (parallel aligned grain boundary) and single crystal core are reliable to attain deformation-resistant behavior.

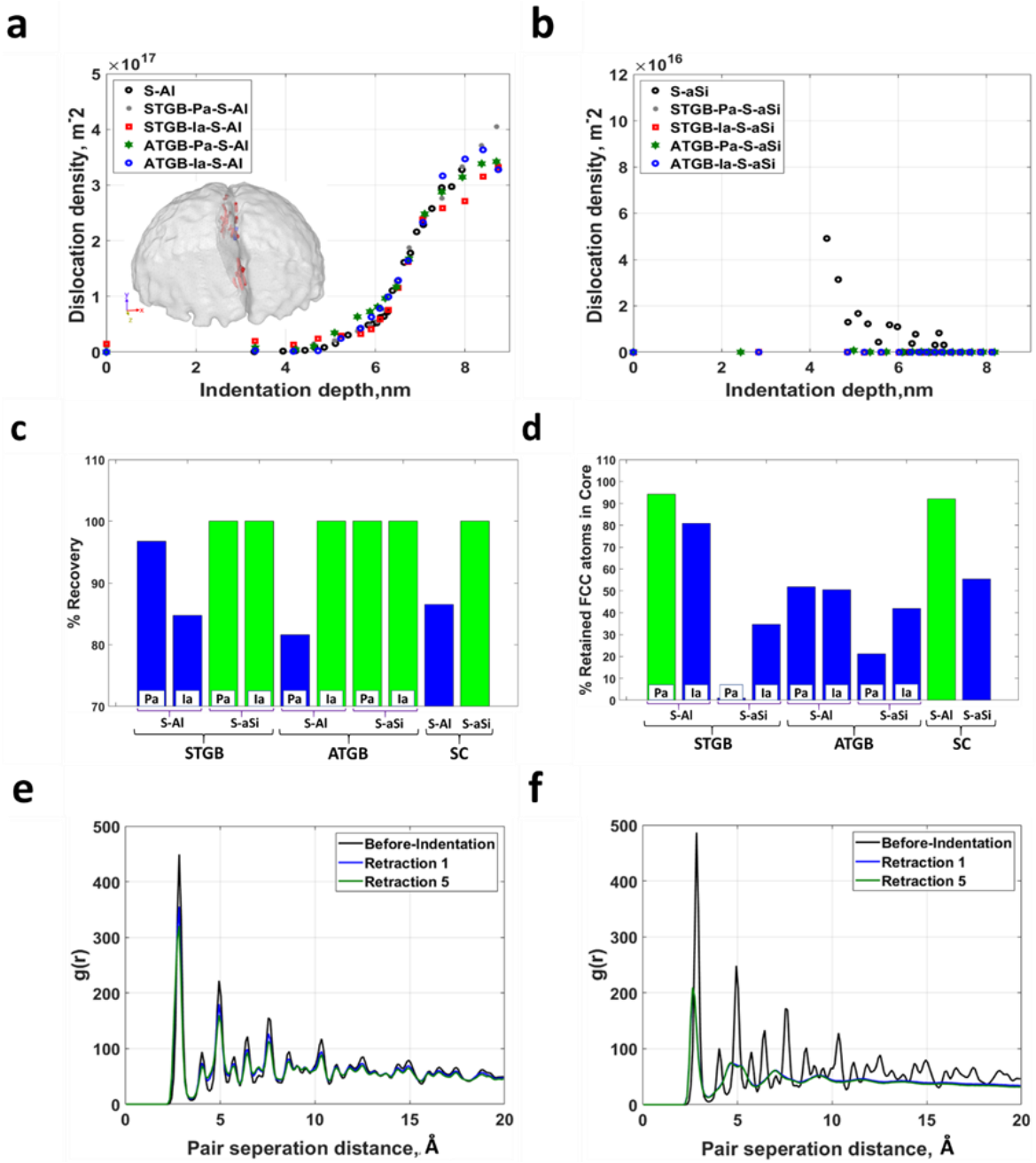

Fig 4. Dislocation evolution during nanoindentation of the CSNs (R = t = 5 nm) with (a) Al substrate, (b) a-Si substrate. (c) The average percentage recovery of dislocations after retraction for all the CSNs. (d) Percentage retained FCC atoms (Al) after retraction for all the CSN's. Coordination analysis performed on CSN before indentation and after retractions for STGB core with (e) Al-substrate, (f) a-Si substrate. The radial distribution function (e, f) is computed using only the atoms in the core. Therefore, the radial distribution function does not converging to 1.0 as pair separation increases because the normalizing factor for the radial distribution function is the entire volume of the simulation cell.

We further investigate the influence of a STGB on CSN behavior for a larger core radius (10 nm) using an Al-substrate (see Fig. 5). The quantitative dislocation analysis using DXA (see initial points in Fig. 5(a)) suggests that the core with a STGB has dislocations at the grain boundaries and core-substrate interface even before applying the load. Similar observations are noticed for CSNs with smaller core radii. Whereas for the single crystal core, the CSN is dislocation free at the beginning of the indentation, and later an increase in dislocation density is observed after 9 nm indentation depth. The dislocation density of these two cases has no noticeable variation after the indentation depth of 10 nm, which is equal to shell thickness. After the 10 nm indentation depth, the dislocations propagate into the substrate and therefore can increase in their line length. Further, we performed retractions at several points and calculated recovery percentages for all samples. From Fig. 5 (b), we can see that CSNs with STGB and single crystal cores all have 100% recovery. In fact, STGB has more than 100% recovery, because some of the initial dislocations in the grain boundaries were also annihilated after retraction. For retraction points greater than 8 nm indentation depth, dislocations remain in the substrate (see Fig. 5(b), inserts 2 and 3), which makes the CSN unreliable for reindentation. However, for single crystal CSN, we see less than 60% recovery for the retraction points after 10 nm indentation depth (see Fig. 5(b), inserts 5 and 6), but we observe 100% recovery for the retraction points before 10 nm indentation depth (see Fig. 5(b), insert 4).

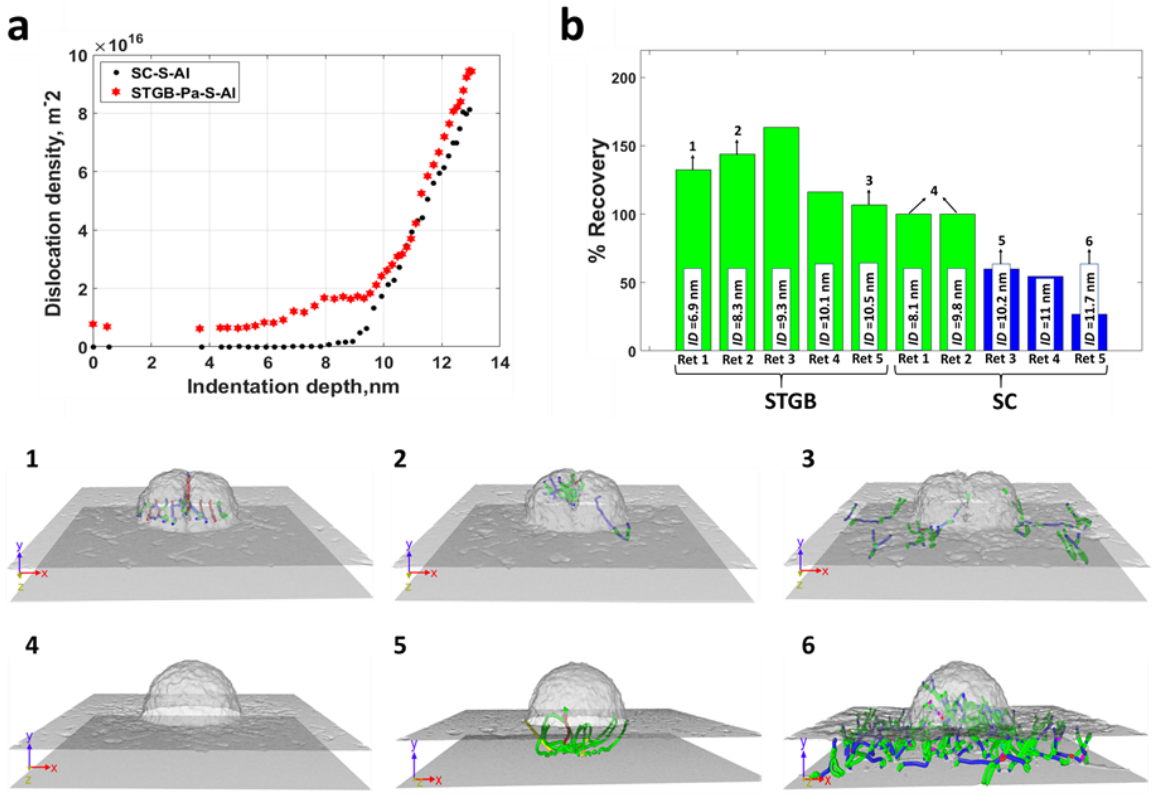

Fig 5. (a) Dislocation density evolution during nanoindentation on CSNs for $R = t = 10$ nm (b) Percentage recovery of dislocations after retraction at various *ID* for symmetric tilt grain boundary parallelly aligned to [0 1 0] axis and single crystal cores of the CSN's whose $R = t = 10$ nm. The inserts 1-6 in (b) shows the final DXA analysis of CSN after retraction. 1 and 4 inserts in (b) show no dislocations in the substrate and 100% recovery from plastic deformation, which makes the CSNs deformation resistant. If the deformation for CSN for STGB core is more than 8 nm (inserts 2, 3) and for single crystal (SC) core is more than 10 nm (inserts 5, 6), dislocations are present in the substrate after retraction which makes this CSN non-deformation resistant.

4.4 Conclusions

The mechanical response and evolution of the dislocation density within CSNs are characterized by nanoindentation and retraction processes using molecular dynamics simulations. For crystalline and a-Si substrates, we observe no difference in stiffness for the CSN in the elastic region, irrespective of whether the core has a grain boundary or not. However, CSNs with a-Si substrate have higher stiffness in the plastic (low and high hardening rate) regions than the CSN with Al substrate. CSNs with a-Si substrate show residual damage in the core after retraction;

therefore, these CSNs are not considered to be deformation-resistant. The STGB (parallel alignment) and single crystal CSNs with Al–substrate performs better than ATGB in terms of dislocation recovery and retains a more significant fraction of FCC atoms, which makes single crystal and STGB CSNs deformation-resistant. However, CSNs with a single crystal core can withstand nanoindentation equal to 100% of the shell thickness whereas, CSNs with a STGB core can only withstand nanoindentation about 80% of the shell thickness and still have 100% recovery. Thus, for less than 10 nm core radius, single crystal core is the most suitable for nanotextures used in tribological applications.

Acknowledgments

We acknowledge the support from the National Science Foundation under the Grant CMMI #1463306. Authors would like to acknowledge the support in part by the National Science Foundation under the grants ARI #0963249, MRI #0959124, and EPS #0918970, and a grant from Arkansas Science and Technology Authority, managed by Arkansas High-Performance Computing Center.

Conflicts of interest: The authors declare no conflict of interest.

References

1. J.-B. Seol, S.-H. Na, B. Gault, J.-E. Kim, J.-C. Han, C.-G. Park and D. Raabe: Core-shell nanoparticle arrays double the strength of steel *Scientific reports.* **7**, 42547 (2017).

2. J.R. Greer and W.D. Nix: Nanoscale gold pillars strengthened through dislocation starvation *Physical Review B.* **73**(24), 245410 (2006).

3. R.A. Fleming and M. Zou: The effects of confined core volume on the mechanical behavior of Al/a-Si core-shell nanostructures *Acta Materialia.* **128**, 149 (2017).

4. R.A. Fleming: Deformation Behavior of Al/a-Si Core-shell Nanostructures, (2017).

5. J.G. Steck, R.A. Fleming, J.A. Goss and M. Zou: Deformation and fatigue resistance of Al/a-Si core-shell nanostructures subjected to cyclic nanoindentation *Applied Surface Science.* **433**, 617 (2018).

6. E.-S. Yoon, R.A. Singh, H. Kong, B. Kim, D.-H. Kim, H.E. Jeong and K.Y. Suh: Tribological properties of bio-mimetic nano-patterned polymeric surfaces on silicon wafer *Tribology Letters.* **21**(1), 31 (2006).

7. N.S. Tambe and B. Bhushan: Micro/nanotribological characterization of PDMS and PMMA used for BioMEMS/NEMS applications *Ultramicroscopy.* **105**(1-4), 238 (2005).

8. H. Wang, R.P. Nair, M. Zou, P.R. Larson, A.L. Pollack, K. Hobbs, M.B. Johnson and O. Awitor: Friction study of a Ni nanodot-patterned surface *Tribology Letters.* **28**(2), 183 (2007).

9. H. Wang, M. Zou, P. Larson, E. Sanchez, K. Hobbs, M. Curtis, M. Johnson and O. Awitor: Nanomechanical properties of a Ni nanodot-patterned surface *Nanotechnology.* **19**(29), 295708 (2008).

10. M. Zou, L. Cai and H. Wang: Adhesion and friction studies of a nano-textured surface produced by spin coating of colloidal silica nanoparticle solution *Tribology Letters.* **21**(1), 25 (2006).

11. B.D. Morton, H. Wang, R.A. Fleming and M. Zou: Nanoscale surface engineering with deformation-resistant core–shell nanostructures *Tribology Letters.* **42**(1), 51 (2011).

12. L.J. Lauhon, M.S. Gudiksen, D. Wang and C.M. Lieber: Epitaxial core–shell and core–multishell nanowire heterostructures *Nature.* **420**(6911), 57 (2002).

13. L. Tsakalakos, J. Balch, J. Fronheiser, B. Korevaar, O. Sulima and J. Rand: Silicon nanowire solar cells *Applied Physics Letters.* **91**(23), 233117 (2007).

14. M.D. Kelzenberg, D.B. Turner-Evans, B.M. Kayes, M.A. Filler, M.C. Putnam, N.S. Lewis and H.A. Atwater: Photovoltaic measurements in single-nanowire silicon solar cells *Nano letters.* **8**(2), 710 (2008).

15. E. Eleftheriou, T. Antonakopoulos, G. Binnig, G. Cherubini, M. Despont, A. Dholakia, U. Durig, M. Lantz, H. Pozidis and H. Rothuizen: Millipede-a MEMS-based scanning-probe data-storage system *IEEE transactions on magnetics.* **39**(2), 938 (2003).

16. R. Xu, S. Zhou and W.J. Li: MEMS accelerometer based nonspecific-user hand gesture recognition *IEEE sensors journal.* **12**(5), 1166 (2011).

17. R.A. Fleming, J.A. Goss and M. Zou: Material dimensionality effects on the nanoindentation behavior of Al/a-Si core-shell nanostructures *Applied Surface Science.* **412**, 96 (2017).

18. A. Rinaldi, S. Licoccia, E. Traversa, K. Sieradzki, P. Peralta, A.B. Dávila-Ibáñez, M.A. Correa-Duarte and V. Salgueirino: Radial inner morphology effects on the mechanical properties of amorphous composite cobalt boride nanoparticles *The Journal of Physical Chemistry C.* **114**(32), 13451 (2010).

19. R.R. Santhapuram, D.E. Spearot and A.K. Nair: Mechanical behavior of core–shell nanostructures *Journal of Materials Science.* 1 (2020).

20. S. Plimpton: Fast parallel algorithms for short-range molecular dynamics *Journal of computational physics.* **117**(1), 1 (1995).

21. P. Hirel: Atomsk: a tool for manipulating and converting atomic data files *Computer Physics Communications.* **197**, 212 (2015).

22. K. Gall, M. Horstemeyer, M. Van Schilfgaarde and M. Baskes: Atomistic simulations on the tensile debonding of an aluminum–silicon interface *Journal of the Mechanics and Physics of Solids.* **48**(10), 2183 (2000).

23. B. Jelinek, S. Groh, M.F. Horstemeyer, J. Houze, S.-G. Kim, G.J. Wagner, A. Moitra and M.I. Baskes: Modified embedded atom method potential for Al, Si, Mg, Cu, and Fe alloys *Physical Review B.* **85**(24), 245102 (2012).

24. A. Stukowski: Visualization and analysis of atomistic simulation data with OVITO–the Open Visualization Tool *Modelling and Simulation in Materials Science and Engineering.* **18**(1), 015012 (2009).

25. Y. Gao, Z. Liu and Z. Zhuang: The investigation of size effect for dislocation starvation mechanism UNDER Cu single-crystal micro-pillar compression, in AIP Conference Proceedings, (**1233**, American Institute of Physics, City, 2010), pp. 436.

26. A. Jérusalem, A. Fernández, A. Kunz and J.R. Greer: Continuum modeling of dislocation starvation and subsequent nucleation in nano-pillar compressions *Scripta Materialia.* **66**(2), 93 (2012).

Chapter 5

5. The effect of dimensional parameters of multi-asperity surfaces on friction at the nanoscale

Raghuram Reddy Santhapuram, Colin Phelan, Min Zou, Arun K Nair

Abstract

Experiments have shown that nanoscale surface texture can effectively reduce the coefficient of friction (COF) between contact surfaces compared to a smooth surface. However, recent simulation work by Santhapuram et al. [1] demonstrated that not all textured surfaces would have lower COF than smooth surfaces, as COF also depends on the counter surface radius. In the current study, we use molecular dynamics on an aluminum surface to investigate a relationship between the spherical counter surface radius (R) and the surface texture variables such as radius of the asperity (r), and pitch length (L) that would effectively reduce the COF when compared to a smooth surface. A relationship is obtained, and it predicts that textured surfaces have lower COF than a smooth surface when $R/(2L - r)$ is greater than 1, otherwise textured surfaces have higher COF than the smooth surface. The relationship obtained is verified by using different surface texture variables and other material surfaces such as silver-nanodot spherical textured surface, and the core-shell spherical textured surface. Further, the trend predicted by the computational model agrees with experiments performed on core-shell spherical textured and smooth surfaces.

Keywords: Nanodot spherical texture surface, Core-shell spherical texture surface, Smooth surface, Molecular Dynamics, Coefficient of Friction

5.1 Introduction

Understanding nanoscale wear and friction is considered critical and necessary for developing applications such as nano-electromechanical systems. The friction and wear of nanoscale materials can be measured using experiments such as nano scratch test [1], and the surface deformation can be analyzed using transmission electron, scanning electron, scanning tunneling, and atomic force microscopes . Besides experimental techniques, atomistic modeling has become a powerful tool to understand friction, wear, and failure modes of materials at the nanoscale.

At the nanoscale, contact theories are developed based on the foundation of single asperity contact that led to contact models for a rough surface [2-4]. This contributed to multi-asperity contact research for various materials in both experimental and computational studies. Tong et al. [5] performed computational studies to find the adhesive effect of textured surfaces by considering different texture shapes, heights, and spacings between them, showing that surface texture can effectively reduce the friction and they also investigated [6] nanoscale sliding contact of two-dimensional textured surfaces. Their results suggest that the average frictional force can be reduced by approximately 90 percent when the counter surface with radius R is in contact with isosceles trapezoid textured surface. Several other researchers have also performed simulations and experiments on nano and micro-textured surfaces by varying asperity radius [7-10], counter surface radius [8, 9, 11, 12], the positioning of the asperities [7-11, 13, 14], and the counter surface velocity [8, 9, 14]. All these studies conclude that the textured surface would effectively reduce friction; however, a relation between the counter surface and the textured surface was not reported for multi-asperity surfaces.

The radius of the counter surface tip during friction tests has a significant impact on the measured COF values [6, 11, 12, 15-18]. The greater contact area of larger tips causes an increase in average friction forces recorded on smooth surfaces. However, when measuring the COF of a Ni nanodot-pattern surface, Wang et al. [12] recorded a COF four times greater with a 1 μm-tip than with a 100 μm-tip. The larger tips resulted in a more significant reduction in COF than the smaller tips because of a more considerable difference in the contact areas between the tip and the textured and the smooth surfaces. Also, less plastic deformation was experienced with the larger tips due to lower contact pressure at the interface. Zou et al. [15] studied the difference in COF measured by a 5 μm-tip and 100 μm-tip and found that the smaller tip follows the surface topography slope, while the larger tip follows the topography of the surface. Due to this, more significant reductions of COF are measured by larger tips than the smaller tips when comparing textured and smooth surfaces. Similarly, Santhapuram and Nair. (2017) [11] studied textured surfaces with different shapes and found that not all textured surfaces could reduce friction, but COF is dependent on the counter surface radius, which is in contact with the textured surface. They found that for a lower counter surface radius, the friction is higher for the textured surface compared to a smooth surface, but for a larger counter surface radius, the friction is lower than the smooth surface.

Aluminum (Al) surface with texture lacks structural integrity [19, 20]. One way to overcome this is by coating the textured surfaces with a material that has a higher hardness to form core-shell nanotextures. The core is made of Al, and the shell is made of a-Si. Several experimental studies [20, 21] have shown that core-shell nanotextured surface shield the core from permanent deformation and still have a lower COF compared to smooth and textured surfaces without the shell. In their recent work, Santhapuram et al. [22] found an optimal shell thickness for an Al core textured surface coated with amorphous silicon. However, there have been no studies at the nanoscale that have

shown a relation between spherical texture surface variables (r, L) and the counter surface radius (R) that will lower the friction compared to a smooth surface. Finding a relation between these variables could help in designing a textured substrate, and a counter surface for different engineering applications to lower friction.

The focus of this research is to determine a relationship between nanodot spherical texture surface (NDSTS) and counter surface variables that would effectively reduce the COF of the textured surface relative to a smooth surface. Therefore, to determine COF, we use molecular dynamics simulations to perform nanoindentation and scratch tests on aluminum nanodot spherical texture and smooth surfaces. The relationship obtained is tested for two different material surfaces, namely silver (Ag) nanodot spherical texture and aluminum-amorphous silicon core-shell nanostructures. Based on computational model predictions, we perform nanoindentation and scratch experiments on aluminum-amorphous silicon core-shell structures to determine the COF. Further, this study will also address the microscopic deformation mechanisms of the textured surfaces during the indentation and scratch process.

5.2 Methodology

5.2.1 Computational method

We perform molecular dynamics simulations using LAMMPS [23] to determine the COF of the textured and smooth surfaces (SS). All samples have periodic boundary conditions along x and z directions and non-periodic boundary conditions along the y-direction. All simulations are performed at 300 K using isothermal and isobaric ensemble (NPT) while maintaining zero pressure along the periodic directions. In this study, we use two types of textured and smooth surfaces. The smooth surface consists of crystalline Al (Al-SS), crystalline Ag (Ag-SS), see Fig 1 (a), green color atoms), and amorphous Si (a-Si-SS, see Fig 1 (a)). The a-Si-SS is obtained by coating a-Si

on the crystalline Al surface along the *x*-*z* plane. Two types of textured surfaces are labeled as nanodot spherical textured surface (NDSTS) and core-shell spherical textured surface (CSSTS). The CSSTSs consists of spherical asperities made of crystalline Al core with radius r = 2 nm and a-Si shell with thickness, t = 2 nm (see Fig 1(b, c)). The shell thickness, t = 2 nm, is chosen based on an optimal core-shell study by Santhapuram et al. [22]. The NDSTSs also consists of spherical asperities but built with crystalline Al core or with crystalline Ag core with radius, r = 3 nm and shell thickness, t = 0 nm (see Fig 1(b, c), green color atoms). The distance between the center of the two asperities along *x* and *z*-directions is called the pitch length (L) (see Fig 2). The pitch lengths used for NDSTSs and CSSTSs in this study are L= 7, 8, 9, and 10 nm and L = 10 nm, respectively. All samples with and without texture have a substrate with dimensions of 35/40/45/50 nm, 10 nm, and 14/16/18/20 nm along *x* [1 1 $\bar{2}$], *y* [1 1 1], and *z* [1 $\bar{1}$ 0] directions, respectively. The different lengths of crystal in *x* and *z* directions are due to the different pitch lengths and number of asperities arranged in each direction. The number of asperities arranged along *x* is 5, and 2 in the *z*-direction. A sample thickness of 10 nm in the *y*-direction is chosen to avoid the substrate effects. For NDSTSs, the Embedded atom method is used for atomic interaction between Al atoms defined by Winey et al. [24] and Ag atoms defined by Williams et al. [25]. Further, Atomic interactions of Al-Si core-shell nanostructure (Al-Al, Si-Si, and Al-Si atoms) are governed by the modified embedded atom method [26] as this potential captures the interface behavior of Al-Si composite. All simulations are visualized in OVITO [27] to perform microstructural analysis.

In this study, we use a repulsive counter surface with force constant, K=10 eV/Å^3. The repulsive counter surface uses a displacement-controlled approach and does not have adhesive forces and will help in extracting geometrical relations. For the chosen texture models: asperity radius, thickness, and pitch lengths are kept constant with varying counter surface radius (R). The

counter surface radius and its center are chosen such that the radius is greater than the asperity size and is at least in contact with two asperities at any given time during the indentation and scratch process. This represents the experimental condition where two surfaces with different asperity radii are in contact with each other. The counter surface location is chosen between the two asperities along the *z*-direction, and the different *R* values used in the study are 4.5, 6, 9, 15, 30, and 45 nm.

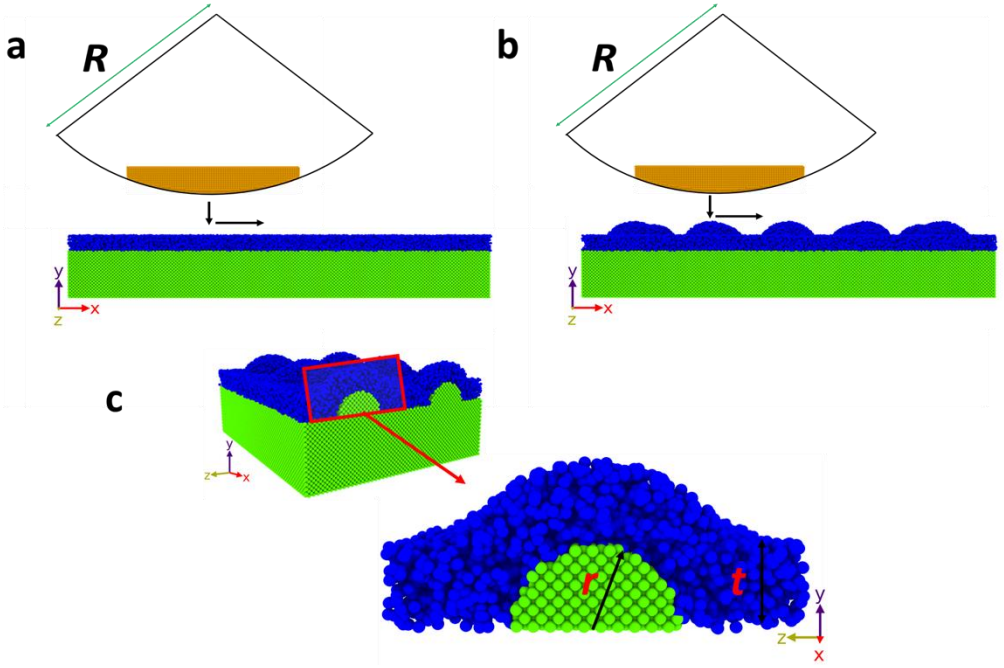

Fig 1. Nanoindentation and scratch process for a smooth and textured surface (a) smooth surface, made of a-Si. (b) CSSTS, substrate, and core are made of Al, and the shell is made of a-Si. (c) cross-section view of the CSSTS, the insert describes the CSSTS attributes, where core radius is defined with "*r*" (*r* = 2 nm), and shell thickness is defined as "*t*" (*t* = 2 nm). The green color atoms in the model represent crystalline Al atoms, and dark blue color atoms represent a-Si. Orange color atoms represent counter surface atoms, and the counter surface radius is defined as *R*. Nanoindentation, and the scratch process is also performed on texture (NDSTS) and smooth surface models (made of crystalline Al) with no shell (where *t* = 0 nm).

The simulation methodology for the repulsive counter surface is implemented using the same method as described in Santhapuram et al. [11]. This approach is named as the displacement-controlled method because the position of the counter surface on top of the substrate can be

accurately guided using an applied velocity. The indentation depth of the counter surface in displacement-controlled method simulations are 1 and 1.5 nm. Once the indentation depth is reached along the *y*-direction, the counter surface is moved along the *x*-direction to scratch the surface. The counter surface velocity is 5 m/s for both the indention and scratch process.

The counter surface center is chosen to coincide with the center of two asperities along the *z*-direction [11], such that it always has contact with at least two asperities, as shown in Fig 2. As the counter surface radius increases, the initial point of contact *p* (see Fig 2) would shift from sides of the asperity to a contact point on the top of the asperity, where *p* value decreases from a maximum of *r* to 0 (see Fig 2). The indentation depth is kept constant for all counter surface radii used. i.e., if the counter surface is in contact with the sides of the asperities where $p = 5$ Å, we indent 5 Å more to have an indentation depth of 1 nm from the top of the asperity. If the counter surface is in contact with the top of the asperity, the asperity is deformed about 1 nm, so that the indentation depth is constant for varying counter surface radii. From our previous work [11], we found that as the counter surface radius increases and has crossed a certain value, the COF of the textured surface decreases compared to the smooth surface. In that study, the only variation other than the counter surface radius is the initial contact point of the counter surface on the textured surface. Therefore, it is assumed that the initial contact point of the counter surface on the asperity should be less than *q* (an unknown number) percentage of *r* to have lower COF for textured surfaces compared to smooth surfaces. Hence, we derive an analytical equation with parameters *r*, *L* and *R* that would affect the COF of the surfaces that would come in contact and are described below. The *q* % is obtained from the MD simulations, as discussed in section 3.1

$$p < (q\ \%)\, r \tag{1}$$

$$r - a < (q\ \%)\, r \tag{2}$$

$$r - r\cos(\emptyset) < (q\ \%)\, r \tag{3}$$

$$1 - \cos(\emptyset) < q\ \% \tag{4}$$

$$1 - \cos(90 - \theta) < q\ \% \tag{5}$$

$$1 - \sin(\theta) < q\ \% \tag{6}$$

$$1 - \left(\frac{h}{R + r}\right) < q\% \tag{7}$$

$$\left(\frac{h}{R + r}\right) > 1 - q\% \tag{8}$$

$$\frac{\sqrt{(R + r)^2 - L^2/4}}{R + r} > 1 - q\% \tag{9}$$

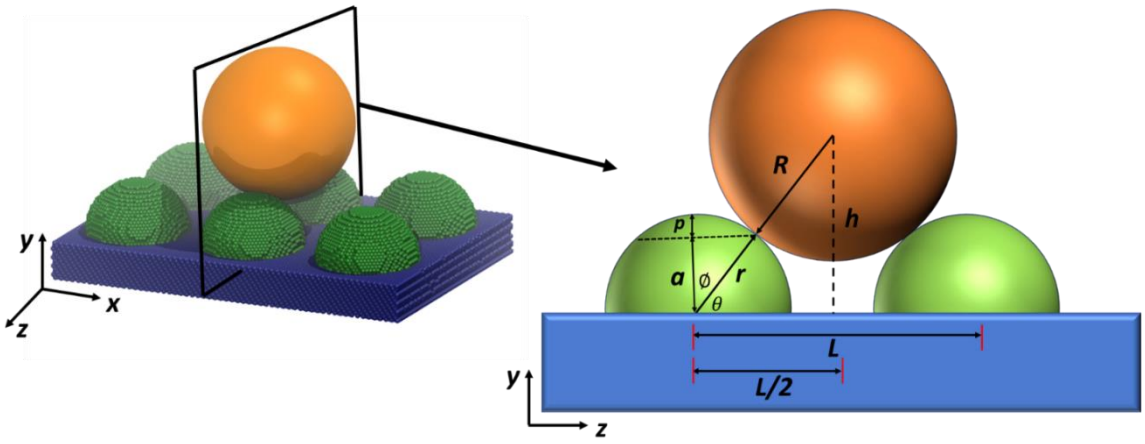

Fig 2. Schematic derived from the model, which represents the initial interaction between the counter surface and the asperities. *R* is the counter surface radius, *r* is the asperity radius, *L* is the pitch length between the asperities, *h* is the distance between the center of the counter surface and the substrate when counter surface meets the asperities. *p* represents the distance at which the counter surface contacts the asperities from the top of the textured surface.

5.2.2 Experimental method

An instrumented nano indenter (TriboIndenter, Hysitron) was used to perform force-controlled nano-scratch experiments. The TriboIndenter has a two-axis transducer with both lateral and vertical force and displacement control and sensing capabilities. The use of both electrostatic force actuation and a three-plate capacitive sensor measuring displacements produces a 3 nN vertical/normal force resolution, 0.04 nm vertical displacement resolution, and 500 nN lateral force resolution. The nano scratch experiments were performed at a constant normal load of 100 μN with a scratch length of 8 μm and a lateral speed of 0.2 μm/s. Before each scratch, the indenter tip contacts the sample at the center of the scratch under 1 μN normal load, travels 4 μm left from the center of the scratch in 10 s, then over the next 10 s, the desired normal load is applied, and the scratch was performed from left to right at 8 μm distance. After each scratch is complete, the indenter tip reduces the normal load over 10 s to 1 μN, and then travels 4 μm back to the center location during the last 10 s of the process. Conical diamond tips with a 60-degree cone angle and 1 μm and 5 μm radii of curvature were used. A CSSTS, consisting of an Al core of 100 nm in diameter and an a-Si shell of 300 nm in thickness, tested in a previous study was used for the experiments [28].

Several techniques were utilized for sample fabrication. Electron beam lithography (EBL) and a metal lift-off procedure were used to create the Al nanodot cores. A positive tone electron resist (4% dilution of 495k MW poly (methyl methacrylate) (PMMA)) was spin-coated onto a 100 crystalline Si wafer at 3000 rpm. Next, with an electron beam writer (JBX-9300FS, JEOL Ltd.), the electron resist was exposed at a 1 nA of current, 50-kV of accelerating voltage, and beam dose of 775–1,000 μC/cm^2. These newly formed arrays were developed in a mixture of methyl isobutyl ketone and isopropyl alcohol (IPA) with a ratio of 1:3 for 45 s. Afterward, pure IPA was used to

rinse the arrays for 15 s. Low-pressure oxygen plasma etch was then used to smoothen the edges of the holes opened in the PMMA film. Then, a 100 nm of Al was deposited on the patterned PMMA film at a rate of 0.4 nm/s using thermal evaporation (Auto 306D, Edwards Vacuum). The sample was then placed within a bath of Remover PG (MicroChem Corp.) heated to 75 °C for 48 h to remove any surplus PMMA. Finally, 300 nm of a-Si was coated on the resulting regular arrays of Al nanodots by plasma-enhanced chemical vapor deposition (Plasma-Therm SLR730). This shell material coats both the Al nanodots and the flat area between nanodots. While depositing the a-Si, the substrate temperature, radio-frequency power, and silane flow rate were 250 °C, 20 W, and 85 sccm, respectively.

The surface consists of arrays of CSSTSs with 1 μm pitch spacing. The *in-situ* scanning-probe microscopy (SPM) of the TriboIndenter was used to image the topography of the CSSTS before and after each scratch at a scanning speed of 1 μm/s using the scratch tips. Nanoscratch tests were then performed with the tips centered between the CSSTSs on the textured surface, similar to Fig 2, and results were compared to scratches performed on a smooth Al/a-Si film surface. Normal and lateral forces and displacements were measured in each test, and the measured COF of the smooth surfaces, with both tip radii, was calculated as the average ratio of the lateral force to the normal force over the scratch length. Similar to the simulations' COF calculations described later in Section 3.1, the COF measured with the 5 μm tip on the textured surface was calculated as the average ratio of the lateral force to the normal force over the scratch length, while the COF measured with the 1 μm tip on the textured surface was calculated as the average of the maximum COF values over the scratch length. The smaller tip radius results in large COF fluctuations over the scratch length, while the COF of the larger tip radius has much lower fluctuations.

5.3 Results and discussion

5.3.1 Computational model predictions

We perform nanoindentation and scratch tests to measure indentation and frictional forces that assist in predicting the coefficient of friction between a counter surface and the textured and smooth surfaces. The initial set of simulations are performed on crystalline Al smooth surface, and Al textured surface (Al-NDSTS) using the displacement-controlled method, to find a relation between geometrical parameters R, r, and L. Later, we check if the relationship works for different material surfaces such as crystalline silver smooth surface (Ag-SS) and corresponding textured surface (Ag-NDSTS), and a-Si smooth surface (a-Si-SS) and the core-shell spherical textured surface (CSSTS) with crystalline Al core and a-Si shell. Further, the relation is tested with experiments using the force-controlled method on a-Si-SS and CSSTSs surfaces.

Displacement controlled indentation is performed on an Al-SS and the Al-NDSTSs. The NDSTS with the core radius, r = 2 nm, and pitch length L = 7 nm is kept constant, and the counter surface radius (R) is varied from 4.5 nm to 45 nm. From the indentation results, we observed that the stiffness of the textured surface increases with an increase in the counter surface radius (see Fig 3 (a)). Similar effects are observed for the smooth surface (see Fig 3 (b)), but an increase in stiffness for the smooth surface is higher than the textured surface. This is because the smooth surface has a higher contact area compared to the textured surface when both surfaces have the same indentation depth. Nanoindentation studies performed for different pitch lengths L = 8 nm and 9 nm and by varying the counter surface radius as before also led to similar results.

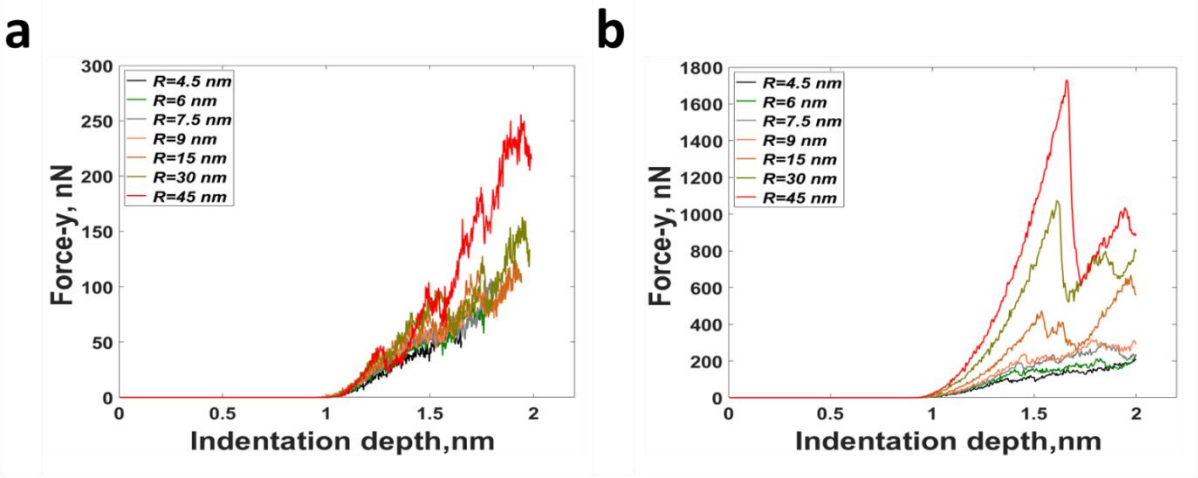

Fig 3. Force vs. indentation depth for varying counter surface radius (R) (a) NDTS with core radius r = 2 nm, L = 7 nm. (b) smooth surface, crystalline Al.

After an indentation depth of 1 nm is reached, the counter surface is moved along x-direction with a constant velocity of 5 m/s to scratch the surfaces (both smooth and NDSTS). The scratch test is performed on Al-SS and three different Al-NDSTS with varying pitch lengths of L = 7 nm, 8 nm, and 9 nm and different counter surface radii. The COF results for three different NDSTS, and corresponding smooth surfaces follow a similar trend. Results for NDSTSs with two different pitch lengths (L = 8 nm, and L = 9 nm) and smooth surface samples are shown in Fig 4. The scratch and normal force of both smooth and NDSTSs increases with an increase in the counter surface radius. A previous study [11] has shown similar observations. The COF is calculated using Amontons-Coulomb law under the high load approximation [29], which is the ratio of scratch force to the normal force. The average COF for a smooth surface is calculated in the dynamic region over the scratch length, where COF fluctuates around a constant value. For textured surfaces, the COF is calculated, as described in Santhapuram and Nair. (2017) [11]. i.e., for the smaller counter surface radius, the COF is calculated by taking the average of the maximum COF values, because of the higher fluctuation of COF values. For the larger counter surface radius, the COF is calculated as an average of the COF values in the dynamic region over the scratch length, because of lower

fluctuation in COF values. The average COF calibrated for textured and smooth surfaces are plotted against the analytical relation from equation 9, see *x*-axis of Fig 4a. The COF data for different pitch lengths revealed that when the analytical relation is less than 0.967, the COF for the textured surface is higher than the smooth surface. If the analytical relation is greater than 0.967, the COF for the textured surface is lower than the smooth surface. The value 0.967 is further used to calculate the initial contact point of the counter surface on the textured surface such that textured surfaces would have lower COF compared to the smooth surface. Therefore, we use the value of 0.967 to simplify the analytical equation further.

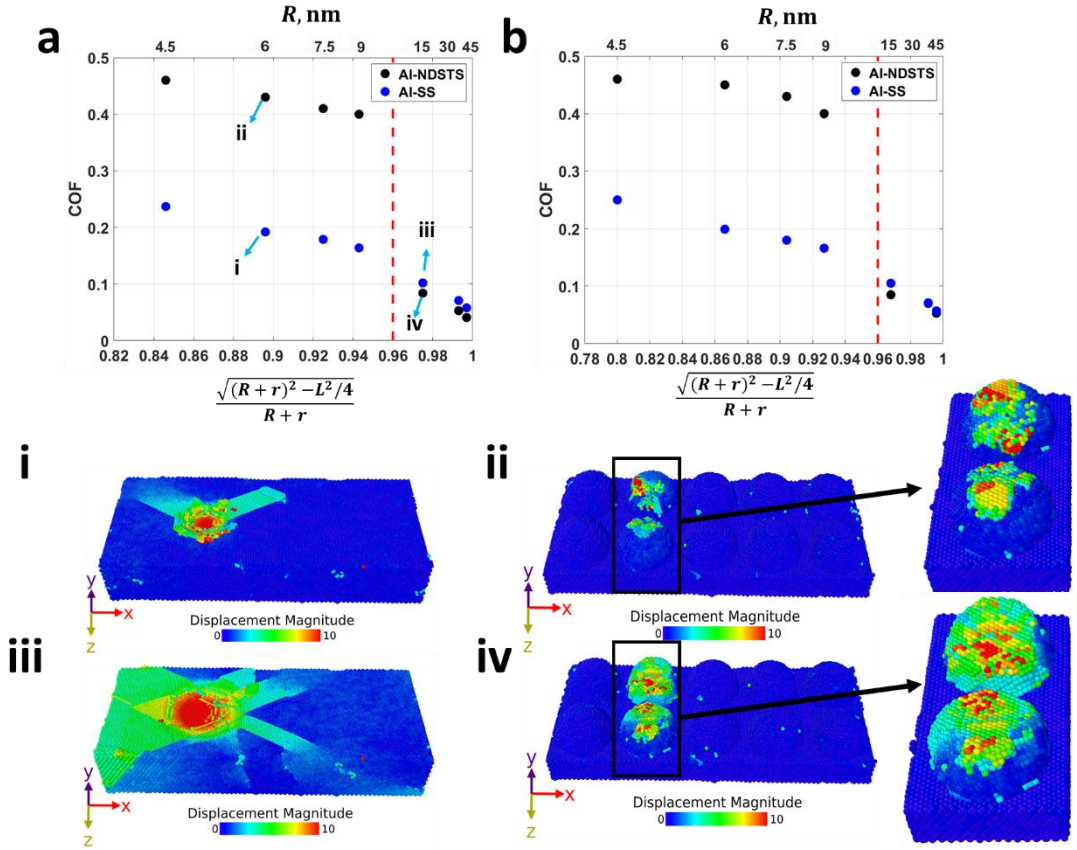

Fig 4. This plot represents COF for textured surface vs. analytical equation (bottom horizontal axis) between the counter surface and textured surface parameters, and COF for smooth surface vs. counter surface radius (top horizontal axis) at the indentation depth of 1 nm. (a) Al-NDSTS with r = 3 nm, L = 8 nm, and the corresponding smooth surface. (b) Al-NDSTS with r = 3 nm, L = 9 nm, and the corresponding smooth surface. The textured surface has a lower COF compared to a smooth surface when the x-axis (relation) is greater than 0.967. (i, ii, iii, and iv) represents the atomic displacement of the textured and smooth surfaces at the end of indentation. (i, ii) atomic

displacements correspond to counter surface radius R = 6 nm. (iii, iv) atomic displacements correspond to counter surface radius R = 15 nm. The color bar indicates the magnitude of atomic displacements, where blue color corresponds to 0 displacement, and the red color corresponds to a maximum of 1 nm.

Substituting 0.967 in equation 9, we find the q% from MD simulations.

$$1 - q\ \% = 0.967 \tag{10}$$

$$q = 3.3\ \% \tag{11}$$

Substituting equation 11 into 1, we obtain

$$p < (3.3\ \%)\, r \tag{12}$$

Equation 12 concludes that the initial contact point of the counter surface should be less than 3.3% of the asperity radius from the top of the asperity, and if this is satisfied, the COF for a textured surface will have a lower COF compared to the smooth surface. We substitute 0.967 in equation 9 to simplify the counter surface asperity relation,

$$\frac{\sqrt{(R+r)^2 - L^2/4}}{R+r} > 0.967 \tag{13}$$

$$\frac{(R+r)^2 - L^2/4}{(R+r)^2} > 0.967^2 \tag{14}$$

$$1 - \frac{L^2}{4(R+r)^2} > 0.9351 \tag{15}$$

$$\frac{L^2}{4(R+r)^2} < 0.0649 \tag{16}$$

$$\left(\frac{L}{2(R+r)}\right) < 0.255 \tag{17}$$

$$L < 0.51\,(R+r) \tag{18}$$

$$R \gtrsim 2L - r \tag{19}$$

$$\frac{R}{2L - r} > 1 \tag{20}$$

This shows that the relation $R/(2L - r)$ should be greater than 1 to have a lower COF for the textured surface compared to the smooth surface. From Fig 4 (a, b), we see that the difference in COF values between textured and smooth surfaces on the left side of the red dotted line, which is much higher than the right side of the red dotted line. This difference is explained in terms of the final displacement of the atoms (see Fig 4 (i, ii, iii, iv)) at the end of the indentation. Fig 4 (i, iii) and (ii, iv) represent displacements of atoms that correspond to smooth and textured surfaces, respectively, at the end of the indentation. Textured surfaces have less displaced atoms (see Fig 4 (ii, iv)) compared to the smooth surfaces (see Fig 4 (i, iii)) at the same indentation depth, and it is independent of the counter surface radii. This shows that the textured surface has a lower contact area compared to the smooth surface. As the counter surface radius increases, the difference between the contact area of the smooth and textured surface decreases because of low indentation depth of 1 nm used in this study. The lower disparity in contact area results in a lower difference in COF values.

Moreover, for a lower counter surface radius (example R = 6 nm), the counter surface is trapped between the textures, and this can be observed before and (see Fig 5 (a)) after indentation (see Fig 4 (ii) and Fig 5 (b)). From Fig 5 (b), we observe that part of the textured surface will obstruct the counter surface displacement in the scratch direction. Therefore, the counter surface needs to completely deform the material that is obstructing it from scratch process, which increases the scratch force. This increases the COF of the textured surface during scratch for a smaller counter surface radius. For higher counter surface radius, for example, 15 nm, the counter surface

lies on top of the asperity before (see Fig 5 (c)) and after indentation (see Fig 5 (d)) the obstruction by the texture in the scratch direction is low, which leads to a lower COF.

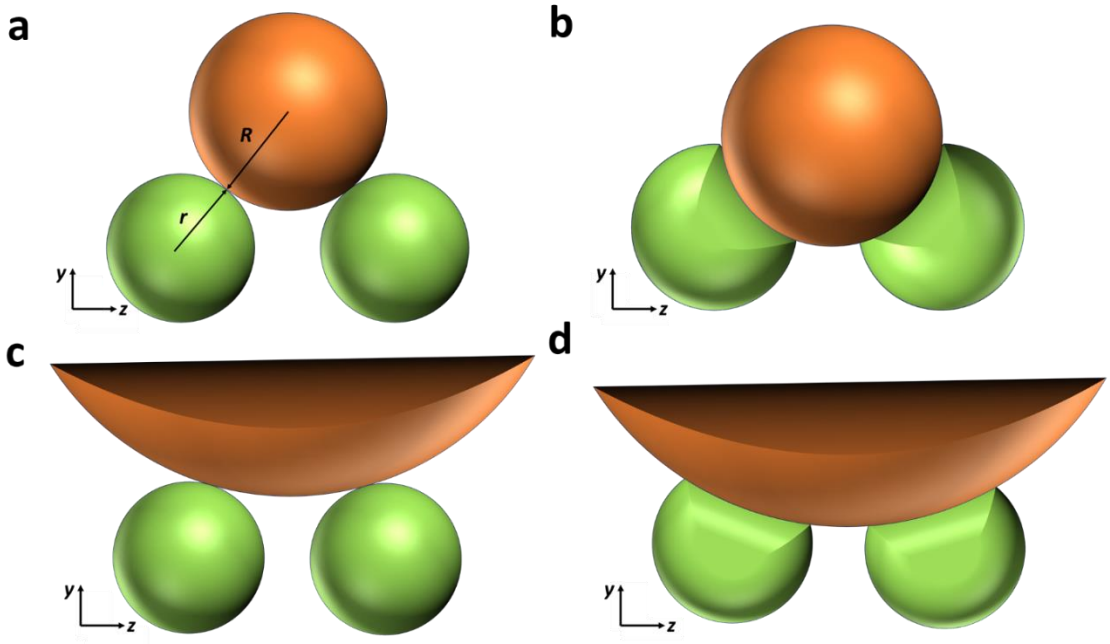

Fig 5. Schematic representation of textured and counter surface (a, c) before indentation and (b, d) after indentation. (b, d) represents probable asperity obstruction during the scratch process along *x* or *z*-direction. Example (a, b) r = 3 nm, R = 4.5 nm, (c, d) r = 3 nm, R = 15 nm (part of the counter surface is shown for better visualization). As the counter surface radius increases, the asperity material obstruction during the scratch decreases and vice versa.

The relation predicted in the previous section is tested for different materials with varying r and L values. This relation is tested using the displacement-controlled method by changing the parameters of the NDSTS (see Fig 6 (a)) and by changing the material of the NDSTS and smooth surfaces (see Fig 6 (b)). The new material used to verify the relation is silver (Ag). The change in the parameters of the textured surfaces is r = 4 nm and L = 10 nm. These parameters remain the same for Ag-NDTS. From Fig 6 (a, b), we see that the change in parameters of the textured surface and material are both satisfying the relation. Furthermore, the relation is tested for CSSTS and a-Si-SS at different indentation depths. For CSSTS and a-Si -SS, the indentation depths studied are

1 nm (see Fig 6 (c)) and 1.5 nm (see Fig 6 (d)). From Fig 6 (c, d), it is clear that the $R/(2L - r)$ relation satisfies CSSTS and also for different indentation depths. Comparing the COF values of CSSTS (see Fig 6 (c)) and NDSTS (see Fig 4 (a, b), and Fig 6 (a)) at 1 nm indentation depths suggests that CSSTS has lower COF compared to NDSTS. A similar trend was reported by previous experimental studies, where the CSSTS have a lower COF compared to NDSTS [19, 28].

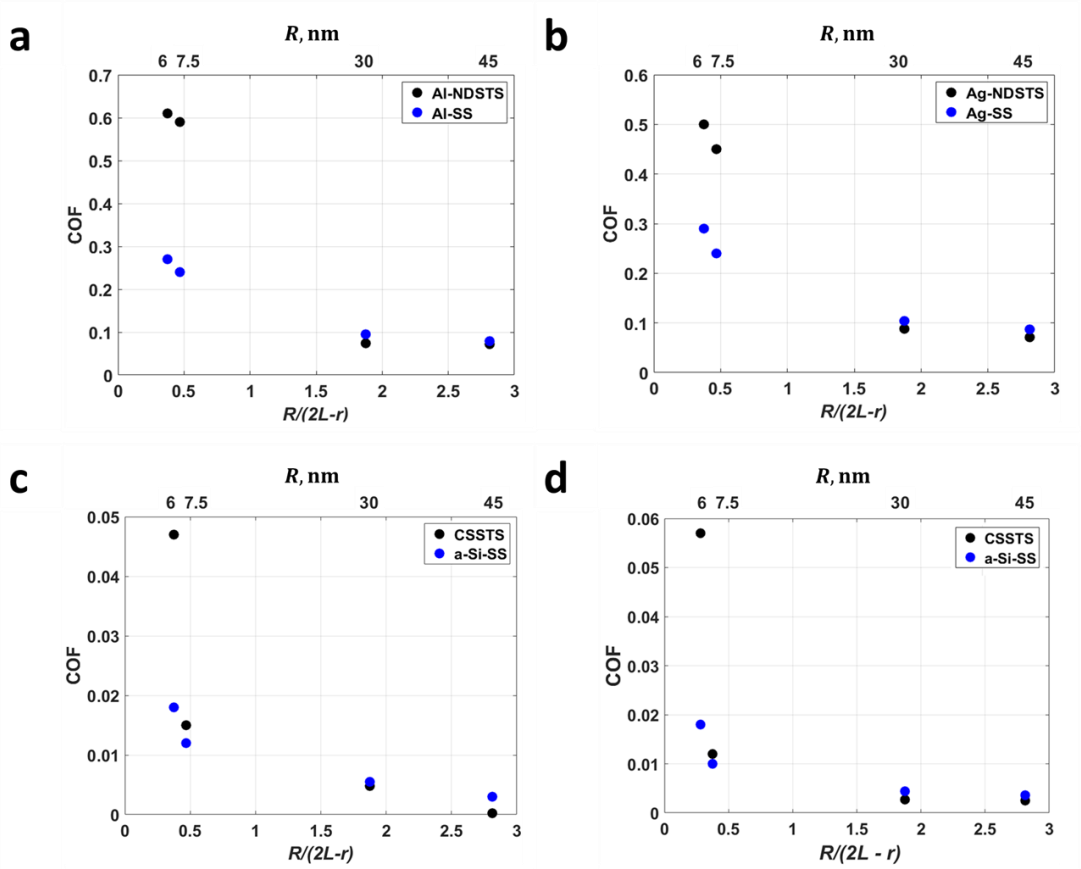

Fig 6. This plot represents the COF for textured surface vs. geometrical relation (bottom horizontal axis) between counter surface and textured surfaces, and COF for the smooth surface vs. counter surface radius (top horizontal axis). (a, b) NDSTS with asperity radius r = 4 nm and pitch length, L = 10 nm at indentation depth of 1 nm. (a) Al. (b) Ag. (c, d) CSSTS, with core radius r = 2 nm, shell thickness t = 2 nm, and a pitch length, L = 10 nm. (c) at an indentation depth of 1 nm. (b) at an indentation depth of 1.5 nm. Textured surface has lower COF compared to the smooth surface when $R/(2L - r)$ is greater than 1.

The trends observed from computational and analytical predictions between textured surfaces and counter surfaces are put to the test using nano scratch experiments. Since the relation obtained in this study predicts the geometrical parameters, here we are trying to test equation 20 for different CSSTSs sizes at the nanometer scale. Due to limitations in experiments, we cannot develop the same CSSTS radius and thickness similar to computational models. However, the calculated ratio of R, r, and L for CSSTS and counter surfaces used in experiments, and the trends for COF are compared.

5.3.2 Experimental results

5.3.2.1 Surface topography

Fig 7 and Fig 8 are the SPM images of the smooth surface and the CSSTS captured before and after the scratch tests using the 1 μm- and 5 μm-tip, respectively. There are noticeable tip convolutions as seen in the differences in the shape and size of the CSSTSs in Fig 7 and Fig 8 and those in the SEM images reported in Fleming et al. [28]. These figures also show the non-uniformity of several CSSTSs in the array, with varying heights and diameters. The 5 μm-tip scratches along several more CSSTSs than the 1 μm-tip because of the increased contact area. Minor plastic deformation was recorded for both tip sizes on the smooth surfaces, with the deformation caused by the 1 μm-tip (~6 nm) being more substantial because of its sharpness compared to the 5 μm-tip (~3 nm).

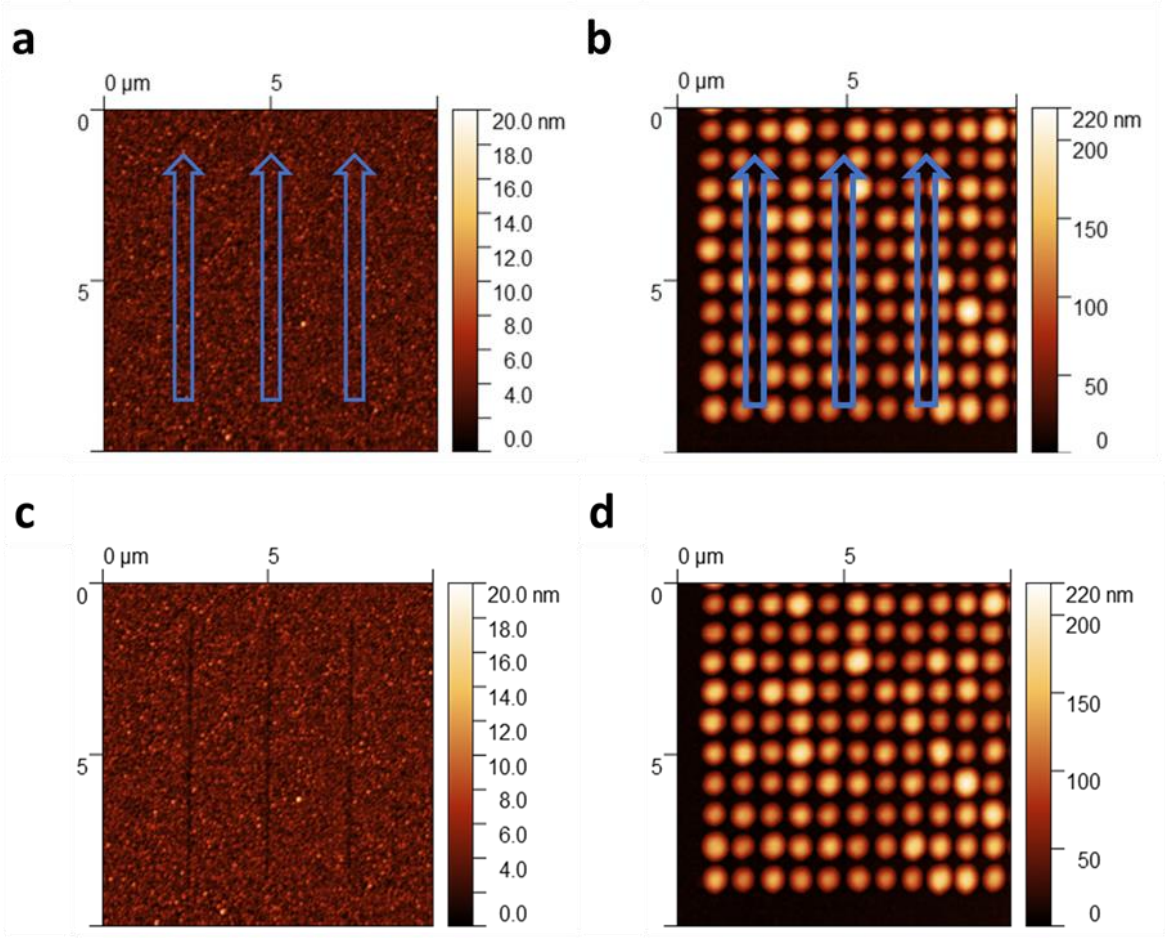

Fig 7. SPM images of the surface topography measured by the 1 μm-tip. (a) Smooth and (b) textured surface before the scratch test with the scratch path shown, respectively. (c) Smooth and (d) textured surface after the scratch test. (Courtesy of Colin Phelan, Dr. Min Zou's lab at the University of Arkansas).

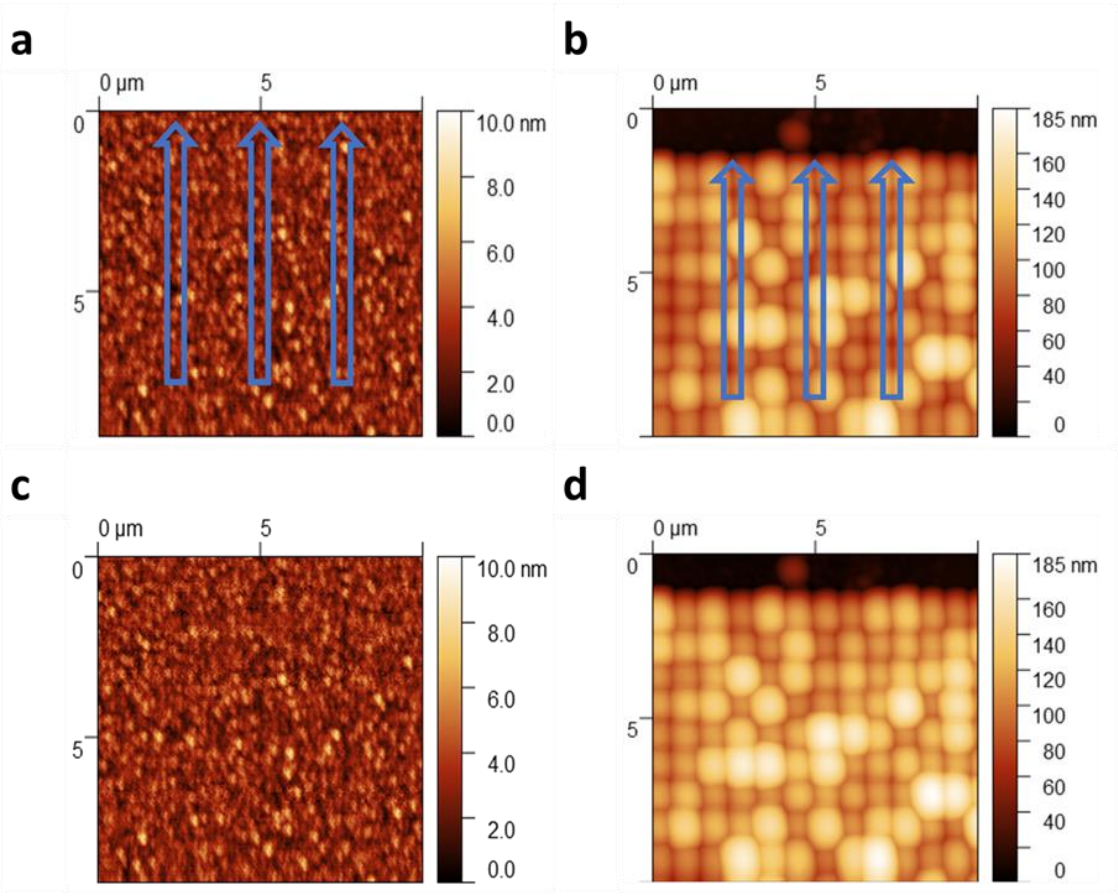

Fig 8. SPM images of the surface topography measured by the 5 μm-tip. (A) Smooth and (B) textured surface before the scratch test with the scratch path shown, respectively. (C) Smooth and (D) textured surface after the scratch test. (Courtesy of Colin Phelan, Dr. Min Zou's lab at the University of Arkansas).

5.3.2.2 Friction measurements

Similar to simulations, the average COFs of both the 1 μm-tip and 5 μm-tip scratches on the smooth and textured surfaces under 100 μN normal loads are shown in Fig 9. For the 1 μm tip, the smooth surface displayed a 56% lower COF than the textured surface. During the scratch on textured surfaces, the tip moves between two rows of CSSTSs. When in contact with CSSTSs, the tip rises and lowers with the topography of the CSSTSs, and the contact pressure also causes the CSSTSs to deform, both increase the COF. When the tip is not in contact with any CSSTSs, it is scratching on the flat areas between the CSSTSs, resulting in similar COF to the smooth surface.

For the 5 μm-tip, the textured surface displayed a 31% lower COF than the smooth surface. During the textured scratches, the tip moves on top of several CSSTSs reducing its contact area compared to the smooth surface and thus reduce the COF.

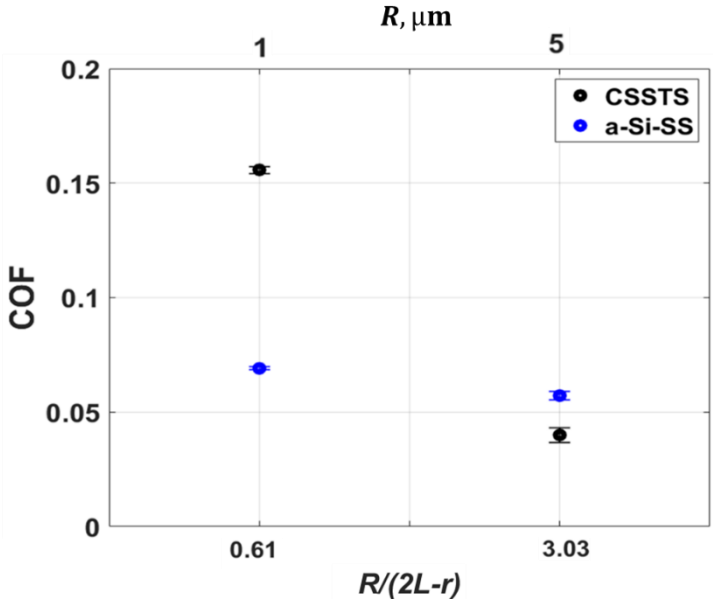

Fig 9. COF vs. relational geometrical parameter (bottom horizontal axis) between the CSSTS and smooth surfaces for 1 μm- and 5 μm-tips (top horizontal axis) with 100 μN loads. (Courtesy of Colin Phelan, Dr. Min Zou's lab at the University of Arkansas).

The COFs measured by the 5 μm-tip on both the smooth and textured surfaces are smaller than those measured by the 1 μm-tip with a 17% and 75% reduction, respectively. The 1 μm-tip is sharper, creating more deformation than the 5 μm-tip due to high contact pressure, resulting in a higher COF on the smooth surface. Scratching over a non-uniform CSSTS affects the 1 μm-tip more than the 5 μm-tip because the 1 μm-tip must travel the profile of any CSSTS, uniform or non-uniform, resulting in the tip to travel sometimes 10s of nanometers higher than expected. The tortuous path of the 1 μm-tip during scratches on the textured surface leads to a higher COF than the 5 μm-tip.

The simulation-based relation $R/(2L\text{-}r)$ predicts that the tested textured surface should have a lower COF than the smooth surface for the 5 μm-tip, but not the 1 μm-tip. For the 1 μm-tip, the relation results in 0.61, which is less than 1, suggesting the COF for a smooth surface would be lower than the textured surface. For the 5 μm-tip, the relation results in 3.03, which is higher than 1, suggesting the COF for a smooth surface would be higher than the textured surface. Therefore, the results of the nano scratch tests seen in Fig 9 agree with the simulation-based relation, $R/(2L\text{-}r)$, for the normal load and tip radii tested.

5.5 Conclusions

In this study, we investigate the geometrical relation between spherical textured and counter surface using computational modeling and analytical method. Computational modeling results show that normal force and scratch force are higher for smooth surface compared to textured surface and increases with an increase in the counter surface radius. In addition, simulation results also predict that when the geometrical relation $R/(2L - r)$ is greater than 1, the COF for a textured surface is lower than a smooth surface, else COF for the textured surface is higher than a smooth surface. The relation obtained is verified for different textured surface variables such as core radii, pitch lengths, and two different materials. Further, the experimental COF results agree with computational predictions at the nanoscale. The geometrical relation obtained in this study could be validated for other spherical textured surfaces composed of FCC or core-shell materials and used to guide the experiments in designing nanoscale texture or counter surfaces for engineering applications.

Acknowledgments

The research was partially supported by the US National Science Foundation (NSF) under Grant No. CMS-1463306 and the Center for Advanced Surface Engineering under Grant No.

OIA-1457888 and the Arkansas EPSCoR Program, ASSET III. We thank the Arkansas Biosciences Institute and the University of Arkansas for major equipment funding support. We also would like to acknowledge the support in part by the National Science Foundation under the grants ARI#0963249, MRI#0959124, and EPS#0918970, and a grant from Arkansas Science and Technology Authority, managed by Arkansas High-Performance Computing Center.

Conflicts of interest: The authors declare no conflict of interest.

References

1. A.T. AlMotasem, J. Bergström, A. Gåård, P. Krakhmalev and L. Holleboom: Atomistic insights on the wear/friction behavior of nanocrystalline ferrite during nanoscratching as revealed by molecular dynamics *Tribology letters.* **65**(3), 101 (2017).

2. J.A. Greenwood and J.P. Williamson: Contact of nominally flat surfaces *Proceedings of the royal society of London. Series A. Mathematical and physical sciences.* **295**(1442), 300 (1966).

3. B.N. Persson: Contact mechanics for randomly rough surfaces *Surface science reports.* **61**(4), 201 (2006).

4. M.H. Müser: Rigorous field-theoretical approach to the contact mechanics of rough elastic solids *Physical review letters.* **100**(5), 055504 (2008).

5. R. Tong, G. Liu and T. Liu: Multiscale analysis on two dimensional nanoscale sliding contacts of textured surfaces *Journal of Tribology.* **133**(4), 041401 (2011).

6. R.-T. Tong and G. Liu: Nanoscale reciprocating sliding contacts of textured surfaces: influence of structure parameters and indentation depth *Chinese Journal of Mechanical Engineering.* **31**(1), 62 (2018).

7. T. Liu, G. Liu, P. Wriggers and S. Zhu: Study on contact characteristic of nanoscale asperities by using molecular dynamics simulations *Journal of tribology.* **131**(2), (2009).

8. R. Tong, G. Liu and T. Liu: Multiscale analysis on two dimensional nanoscale sliding contacts of textured surfaces *Journal of tribology.* **133**(4), (2011).

9. R. Tong, G. Liu and L. Liu: Multiscale analysis on two-dimensional nanoscale adhesive contacts *Chinese Journal of Mechanical Engineering.* **25**(3), 446 (2012).

10. U. Pettersson and S. Jacobson: Influence of surface texture on boundary lubricated sliding contacts *Tribology international.* **36**(11), 857 (2003).

11. R.R. Santhapuram and A.K. Nair: Frictional properties of multi-asperity surfaces at the nanoscale *Computational Materials Science.* **136**, 253 (2017).

12. H. Wang, R.P. Nair, M. Zou, P.R. Larson, A.L. Pollack, K. Hobbs, M.B. Johnson and O. Awitor: Friction study of a Ni nanodot-patterned surface *Tribology Letters.* **28**(2), 183 (2007).

13. W. Cheong and L. Zhang: Monocrystalline silicon subjected to multi-asperity sliding: nano-wear mechanisms, subsurface damage and effect of asperity interaction *International Journal of Materials and Product Technology.* **18**(4-6), 398 (2003).

14. A. Kovalchenko, O. Ajayi, A. Erdemir, G. Fenske and I. Etsion: The effect of laser surface texturing on transitions in lubrication regimes during unidirectional sliding contact *Tribology International.* **38**(3), 219 (2005).

15. M. Zou, L. Cai, H. Wang, D. Yang and T. Wyrobek: Adhesion and friction studies of a selectively micro/nano-textured surface produced by UV assisted crystallization of amorphous silicon *Tribology Letters.* **20**(1), 43 (2005).

16. M. Zou, L. Cai and H. Wang: Adhesion and friction studies of a nano-textured surface produced by spin coating of colloidal silica nanoparticle solution *Tribology Letters.* **21**(1), 25 (2006).

17. H. Zhang and K. Komvopoulos: Scale-dependent nanomechanical behavior and anisotropic friction of nanotextured silicon surfaces *Journal of Materials Research.* **24**(10), 3038 (2009).

18. T. Staedler and K.I. Schiffmann: Influence of tipradius and substrate on the nanotribological characterization of thin DLC coatings *MRS Online Proceedings Library Archive.* **649**, (2000).

19. R.A. Fleming: Deformation Behavior of Al/a-Si Core-shell Nanostructures, (2017).

20. R.A. Fleming, J.A. Goss and M. Zou: Material dimensionality effects on the nanoindentation behavior of Al/a-Si core-shell nanostructures *Applied Surface Science.* **412**, 96 (2017).

21. R.A. Fleming and M. Zou: The effects of confined core volume on the mechanical behavior of Al/a-Si core-shell nanostructures *Acta Materialia.* **128**, 149 (2017).

22. R.R. Santhapuram, D.E. Spearot and A.K. Nair: Mechanical behavior of core–shell nanostructures *Journal of Materials Science.* 1 (2020).

23. S. Plimpton: Fast parallel algorithms for short-range molecular dynamics *Journal of computational physics.* **117**(1), 1 (1995).

24. J. Winey, A. Kubota and Y. Gupta: Thermodynamic approach to determine accurate potentials for molecular dynamics simulations: thermoelastic response of aluminum *Modelling and Simulation in Materials Science and Engineering.* **18**(2), 029801 (2010).

25. P. Williams, Y. Mishin and J. Hamilton: An embedded-atom potential for the Cu–Ag system *Modelling and Simulation in Materials Science and Engineering.* **14**(5), 817 (2006).

26. B. Jelinek, S. Groh, M.F. Horstemeyer, J. Houze, S.-G. Kim, G.J. Wagner, A. Moitra and M.I. Baskes: Modified embedded atom method potential for Al, Si, Mg, Cu, and Fe alloys *Physical Review B.* **85**(24), 245102 (2012).

27. A. Stukowski: Visualization and analysis of atomistic simulation data with OVITO–the Open Visualization Tool *Modelling and Simulation in Materials Science and Engineering.* **18**(1), 015012 (2009).

28. R.A. Fleming and M. Zou: Nanostructure-textured surfaces with low friction and high deformation resistance *Tribology Transactions.* **61**(1), 80 (2018).

29. J.P. Ewen, C. Gattinoni, F.M. Thakkar, N. Morgan, H.A. Spikes and D. Dini: Nonequilibrium molecular dynamics investigation of the reduction in friction and wear by carbon nanoparticles between iron surfaces *Tribology Letters.* **63**(3), 38 (2016).

Chapter 6

6. Conclusions

The objectives defined in section 1.2 have been addressed using molecular dynamics simulations. This study predicts the mechanical, frictional, and deformation characteristics of multi-asperity surfaces at the nanoscale, without shell (Chapters 2 and 5) and with shell (Chapter 5). We also studied the indentation and deformation-resistant behavior of single-asperity core-shell structures (Chapters 3, 4) at the nanoscale.

Our initial study finds the effective geometry of the multi-asperity surfaces that would reduce friction (Chapter 2). This study also indicates that not all textured surfaces have lower COF as COF also depends on the counter surface radius. Further, these textured surfaces deform permanently, as evident from our previous research. Therefore, later in this study, we performed the indentation study by varying the core radius and shell thickness of the core-shell nanostructures. Additionally, we determined the optimal shell thickness for a given core radius of the core-shell nanostructure (Chapter 3). This study also suggests that as the indenter contact area on the shell of CSN increases, the dislocation density increases within the core of the CSN. We also study the effect of core and substrate materials on deformation-resistant characteristics of core-shell nanostructures (Chapter 4). Since the initial study suggests not all textured surfaces will have lower COF compared to a smooth surface, we performed a parameterized study of the geometrical variables on the textured and counter surface to find a relationship between the geometrical variables. The relationship obtained in this work would help design the textured surfaces that will have lower COF compared to a smooth surface (Chapter 5). The unique contributions and understanding drawn from this study are summarized below.

1. During the displacement-controlled indentation and scratch test, the indentation force, scratch force, and average normal force increases as the indenter radius increases, but an increase in the scratch force is much lower than the normal force.
2. The coefficient of friction decreases with an increase in the indenter radius.
3. During the scratch process, dislocations move towards the surface and form step for both smooth and textured surfaces.
4. The friction coefficient is lower for spherical asperity surfaces without shell if the indenter radius is less than or equal to 4 nm. Further, the friction coefficient is lower for cylindrical asperity, if the indenter radius is greater than or equal to 5 nm.
5. We observe no difference in stiffness for CSNs with varying shell thickness except a shift in the elastic and plastic deformation regions towards higher indentation depths.
6. The ratio of the core radius to shell thickness should be between 0.5 and 2 ($0.5 < r/t < 2$) to have a deformation-resistant behavior for the CSNs.
7. The CSN with an a-Si substrate has shown phase transformation in the core after retraction; therefore, these CSNs are not considered as deformation-resistant.
8. The symmetric tilt grain boundary and the single-crystal core of CSNs with Al-substrate perform better than the asymmetric tilt grain boundary in terms of dislocation recovery and crystalline structure retainment, which makes these CSNs deformation-resistant.
9. Spherical textured surface will have a lower coefficient of friction compared to a smooth surface when $R > (2L - r)$.
10. The relation $R > (2L - r)$ is validated for different materials (Al, Ag, and Al/a-Si (CSN)) and also agree with experiments for CSNs for the tested tip sizes.

6.1 Future work

6.1.1 Core-shell nanostructures

In this study, we found a ratio of core radius and shell thickness that would make the CSNs a deformation-resistant nanostructure. But is this also true for a different material combination? Further experiments and computational modeling should also be carried out for different material combinations while maintaining core material as crystalline and shell material as amorphous to characterize if this property is material-dependent or structure independent.

Further, this study has shown that the single-crystal core performs better in terms of deformation-resistence compared to polycrystal core, but the grain radii studied here is less than or equal to 10 nm. Is this property going to change for a higher grain radius? Further studies need to be performed. Till now, experiments are performed for polycrystal core but not for single crystal core.

6.1.2 Multi-asperity surfaces

For multi-asperity surfaces, we determined the relation between dimensional parameters of spherical multi-asperity and counter surfaces. This relation effectively reduces friction for asperity surfaces compared to a smooth surface. This relation is also tested for core-shell multi asperity surfaces through simulations and experiments. Will this relation be true for other spherical multi-asperity core-shell nanostructures with different material combinations? This can be tested either through a computational approach or through experiments or a combination of both.

Appendix A

Supplementary material for paper 2: Mechanical behavior of core-shell nanostructures

Raghuram Reddy Santhapuram, Douglas E. Spearot, Arun K Nair

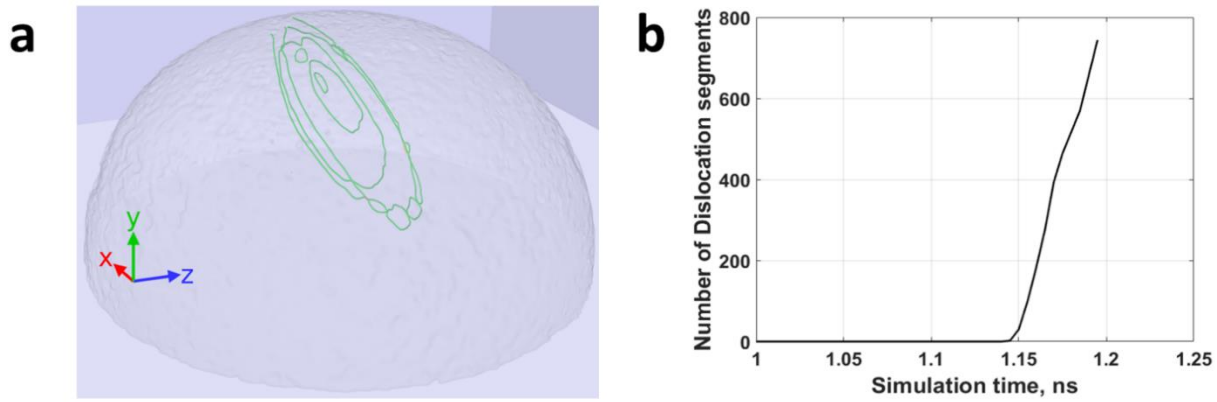

S1. (a) Shear loop formed in the Al core during nanoindentation of core shell nanostructure (CSN) with core radius of 30 nm and shell thickness of 20 nm. (b) Number of dislocation segment versus simulation time for CSN for core radius of 30 nm and shell thickness of 20 nm.

We observe dislocation starvation mechanism for the CSN (R = 10 nm, see S2.c and S3 below) but with the increase the core radius the dislocation starvation mechanism becomes less prominent as the dislocations need to travel farther distance in order to find the interface. The CSNs used in this study, we observe that the initial dislocation nucleates after indenter displacement is greater than its shell thickness. However, for a higher core radius (R = 30 nm) sample after initial dislocation nucleation event, even a small indenter displacement, we observe the strain burst which leads to sudden increase in dislocation segments (see S1.b). This indicates that as the R increases the CSN almost behaves like the flat model (see S2.d) except initial dislocation nucleation happens at very latter stages (see S2.a, and b). Therefore, for higher CSN it is safe to limit the deformation less than the shell thickness as we did not observe 100% recovery for higher core radius used in this study (R = 30 nm, See Fig 5 (b) in the manuscript).

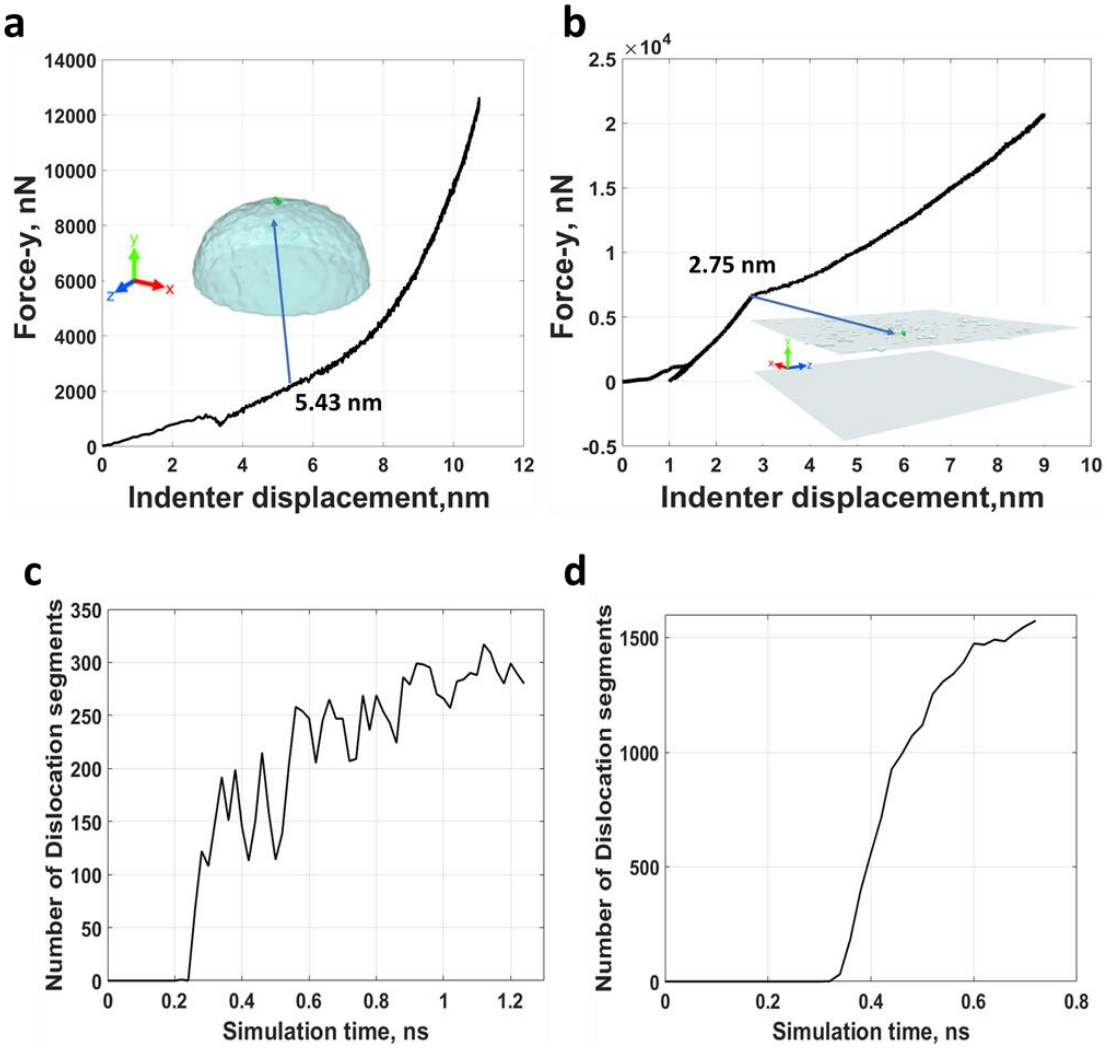

S2. (a, b) Force versus indenter displacement plots of core shell nanostructure (CSN) with core radius of 10 nm and shell thickness of 5 nm: (a) spherical CSN and (b) flat CSN. (c, d) Number of dislocation segment versus simulation time for CSN for core radius of 10 nm and shell thickness of 5 nm: (c) spherical CSN and (d) flat CSN.

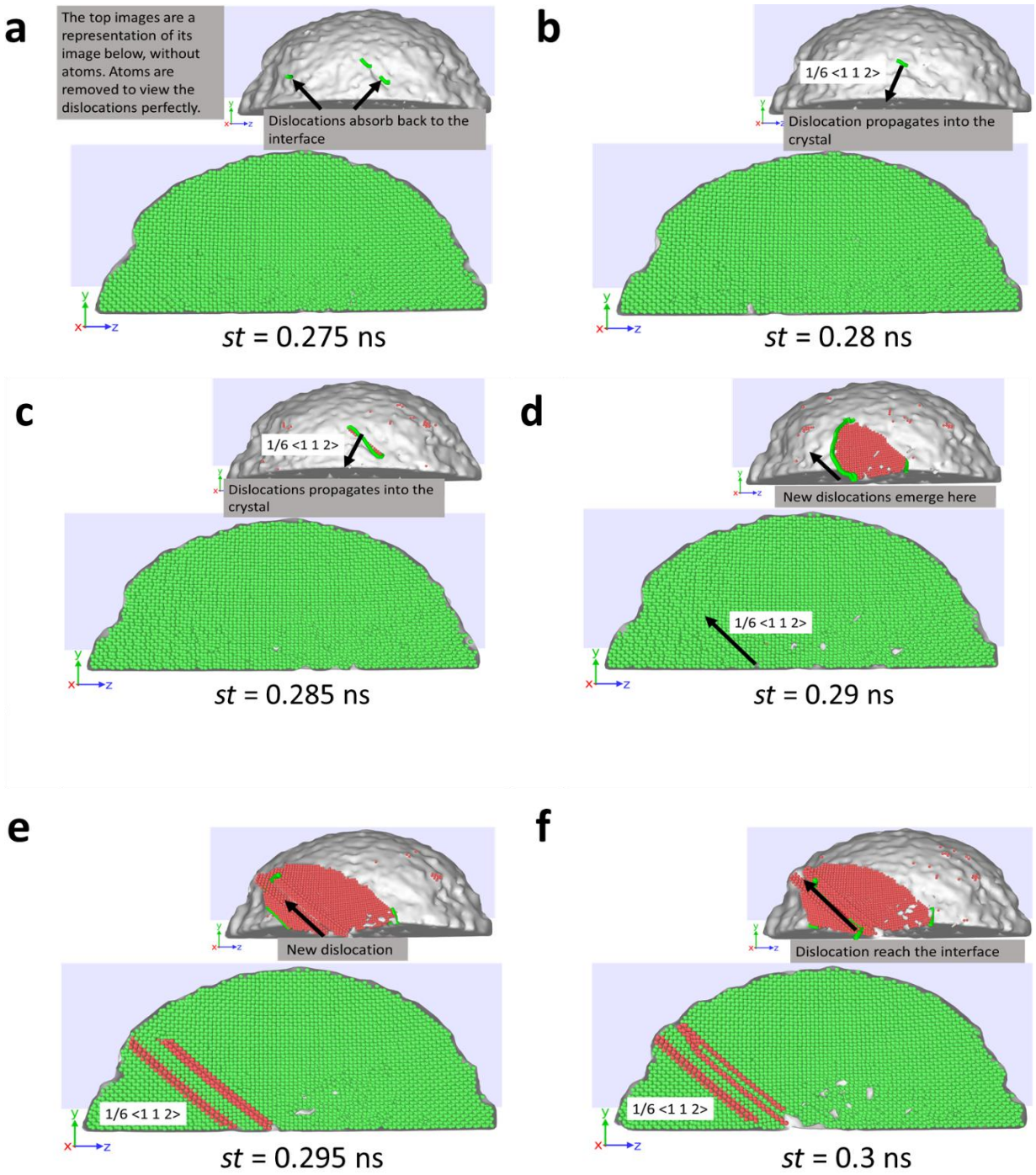
a
The top images are a representation of its image below, without atoms. Atoms are removed to view the dislocations perfectly.
Dislocations absorb back to the interface
st = 0.275 ns
b
1/6 <1 1 2>
Dislocation propagates into the crystal
st = 0.28 ns
c
1/6 <1 1 2>
Dislocations propagates into the crystal
st = 0.285 ns
d
New dislocations emerge here
1/6 <1 1 2>
st = 0.29 ns
e
New dislocation
1/6 <1 1 2>
st = 0.295 ns
f
Dislocation reach the interface
1/6 <1 1 2>
st = 0.3 ns

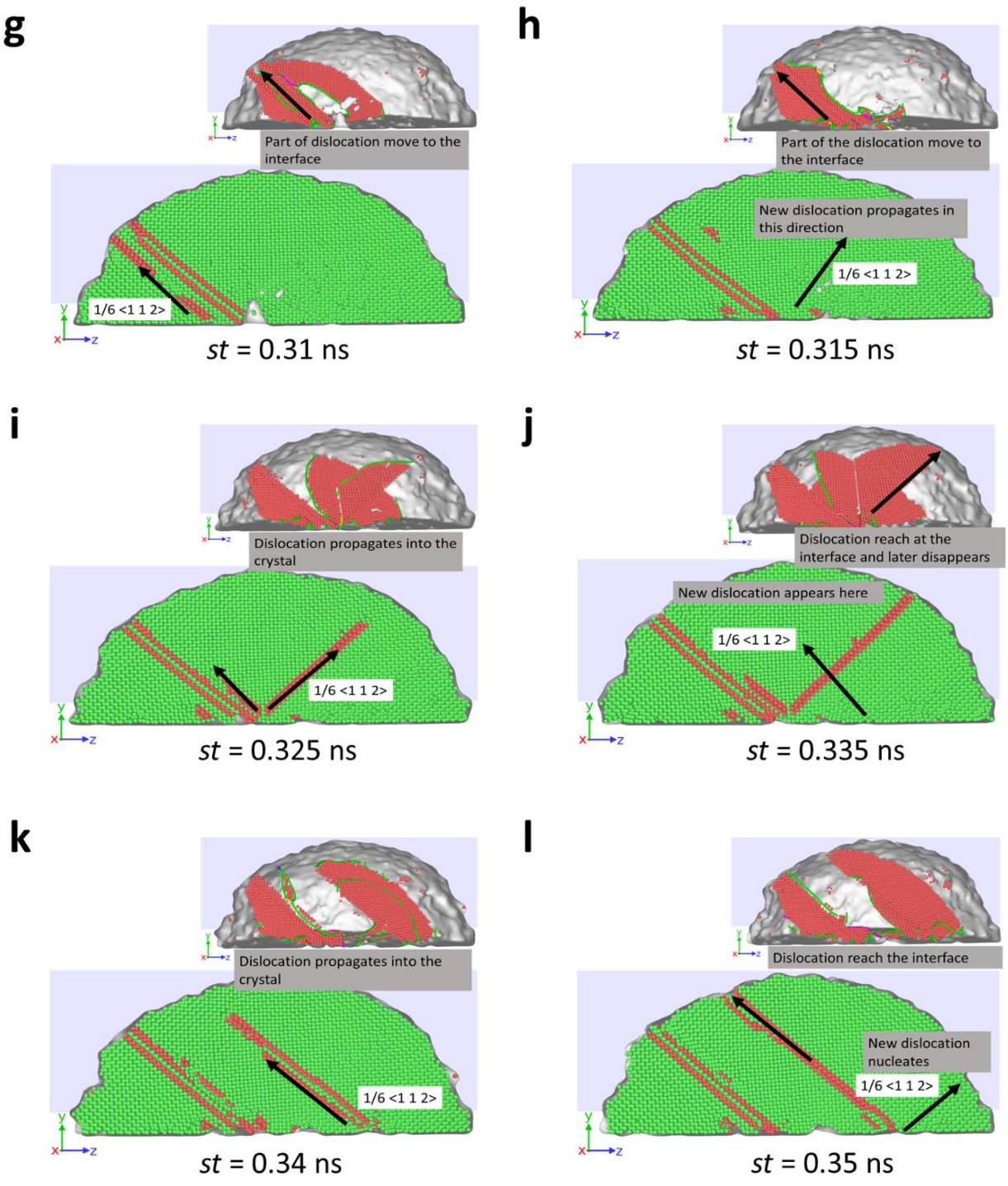
g
Part of dislocation move to the interface
1/6 <1 1 2>
st = 0.31 ns
h
Part of the dislocation move to the interface
New dislocation propagates in this direction
1/6 <1 1 2>
st = 0.315 ns
i
Dislocation propagates into the crystal
1/6 <1 1 2>
st = 0.325 ns
j
Dislocation reach at the interface and later disappears
New dislocation appears here
1/6 <1 1 2>
st = 0.335 ns
k
Dislocation propagates into the crystal
1/6 <1 1 2>
st = 0.34 ns
l
Dislocation reach the interface
New dislocation nucleates
1/6 <1 1 2>
st = 0.35 ns

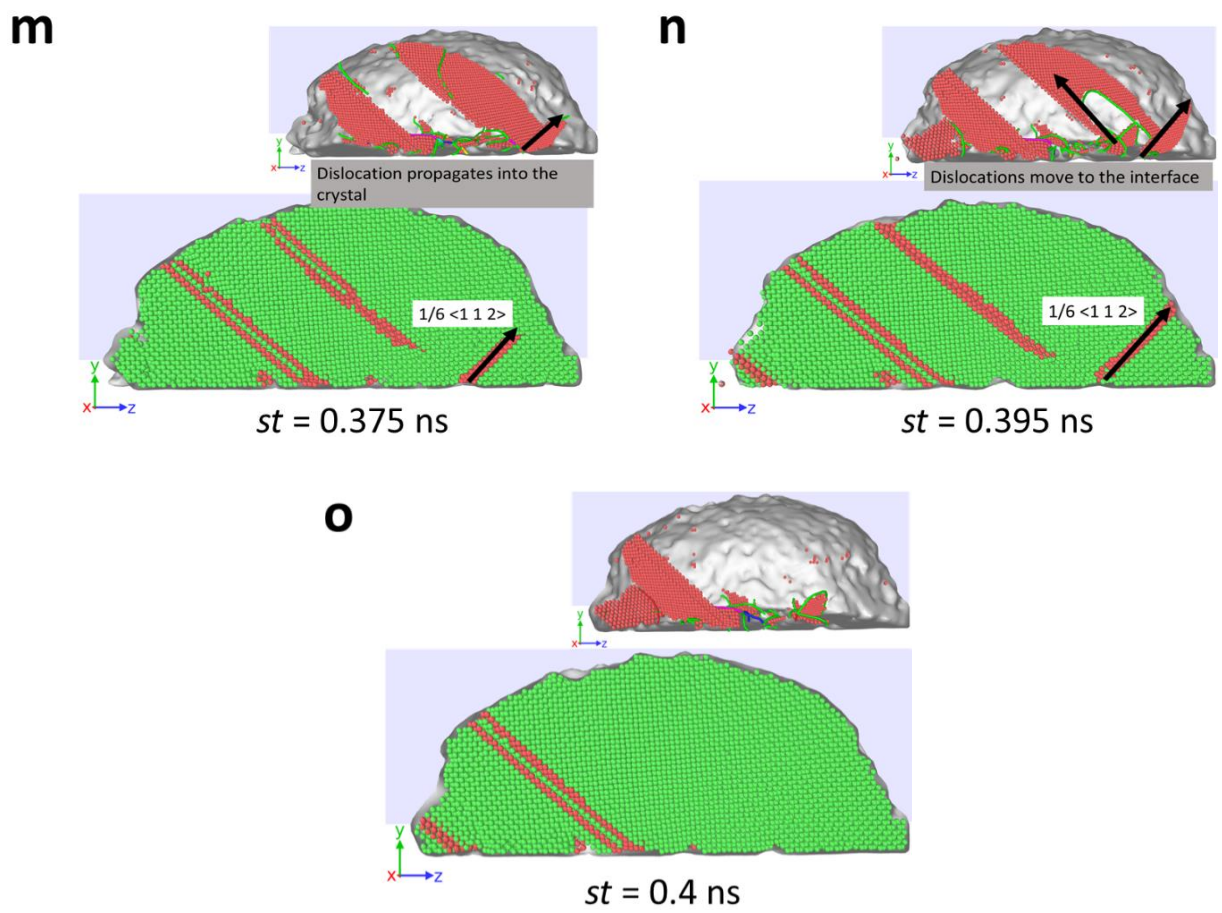

S3. (a-o) Represents the dislocation starvation mechanism over indentation simulation time (*st*) for CSN (*R*=10 nm, *t*=10 nm). The top images are a representation of the image below without atoms. Atoms at perfect lattice position are removed to visualize the dislocations. The corresponding dislocation segments versus simulation time plot is shown in the manuscript, see Fig 3(d).